A COMBINED TOP-DOWN/BOTTOM-UP ROUTE TO FABRICATING GRAPHENE DEVICES

A Thesis
Presented to
The Academic Faculty

by

Jeremy D. Hicks

In Partial Fulfillment
of the Requirements for the Degree
Doctor of Philosophy in the
School of Electrical and Computer Engineering

Georgia Institute of Technology
August 2013

A COMBINED TOP-DOWN/BOTTOM-UP ROUTE TO FABRICATING GRAPHENE DEVICES

Approved by:

Edward H. Conrad, Advisor
School of Physics
Georgia Institute of Technology

John D. Cressler, Co-Advisor
School of Electrical & Computer
Engineering
Georgia Institute of Technology

Azad Naeemi
School of Electrical & Computer
Engineering
Georgia Institute of Technology

Walt A. de Heer
School of Physics
Georgia Institute of Technology

Ali Adibi
School of Electrical & Computer
Engineering
Georgia Institute of Technology

Thomas K. Gaylord
School of Electrical & Computer
Engineering
Georgia Institute of Technology

Date Approved: June 28, 2013

ACKNOWLEDGEMENTS

I would first like to thank my advisor, Prof. Edward Conrad, for his mentorship, advice (both inside and outside of the lab) and, along with his wife, Dr. Leyla Conrad, for encouraging my professional development. Many professors discourage activities such as internships, but Ed was nothing but supportive. In all, I cannot imagine having had a better graduate school experience.

I also thank my committee for their guidance on creating an impactful thesis, and the numerous other scientists who have assisted or mentored me at various points, including Drs. Claire Berger and Patrick Soukiassian, as well as Drs. Amina Taleb-Ibrahimi, Antonio Tejeda, and rest of the Cassiopée beamline at Synchrotron SOLEIL. I am indebted to the students and staff, present and past, of the greater graphene group at Georgia Tech, including Dr. Ming Ruan, Dr. Kristin Shepperd, Dr. Michael Sprinkle, Dr. Farhana Zaman, Zelei Guo, John Hankinson, Yike Hu, Meredith Nevius, James Palmer, Andrei Savu, Holly Tinkey, Britt Torrance, and Feng Wang. Outside of the graphene group, I am grateful to my co-advisor, Prof. John Cressler, for always being there to help, as well as his students, including Dr. Rajan Arora, Partha Chakraborty, and Eleazar Kenyon for their assistance in radiation experiments and electrical measurements. In the cleanroom, I could not have gotten far without the periodic aid of Dr. Mikkel Thomas, Devin Brown, Janet Cobb-Sullivan, and Charlie Suh, as well as the rest of the IEN staff.

Finally, I wish to acknowledge Prof. Ant Ural and Dr. Ashkan Behnam, who introduced me to carbon electronics and were the proximate reason for my pursuing graphene research. Ultimately, however, I am indebted to my parents, whose constant advocacy for my education has shaped my future in ways I will never know.

TABLE OF CONTENTS

LIST OF TABLES

LIST OF FIGURES

LIST OF SYMBOLS OR ABBREVIATIONS

λ Photon wavelength

Φ Material work function

a Graphene lattice constant ≈ 2.46 Å (unless otherwise specified)

E_D Dirac point

E_F Fermi energy

$\hbar$ Reduced Planck constant $\approx 6.582 \times 10^{-16}$ eV·s

$\mathbf{k}$ Crystal momentum vector with scalar vector components k_i

k_B Boltzmann constant $\approx 8.617 \times 10^{-5}$ eV·K^{-1}

t Electronic "hopping energy" between neighboring atoms ≈ 3 eV

v_F Fermi velocity

AFM   Atomic force microscopy

ARPES   Angle-resolved photoemission spectroscopy

BZ   Brillouin zone

C-face   The $(000\bar{1})$ face of hexagonal SiC

CCS   Confinement-controlled sublimation

CVD   Chemical vapor deposition

EBL   Electron beam lithography

EDC   Energy distribution curve

EFM   Electrostatic force microscopy

FET   Field-effect transistor

FLG   Few-layer graphite; grown from SiC (0001)

GFET   Graphene field-effect transistor

HOPG   Highly-ordered pyrolytic graphite

IPA   Isopropyl alcohol

LEED   Low-energy electron diffraction

MEG	Multilayer epitaxial graphene; grown from SiC $(000\bar{1})$
RIE	Reactive-ion etching
SEM	Scanning electron microscopy
Si-face	The (0001) face of hexagonal SiC
SiC	Silicon carbide
STM	Scanning tunneling microscopy
STS	Scanning tunneling spectroscopy
SXRD	Surface x-ray diffraction
TEM	Transmission electron microscopy
UHV	Ultra-high vacuum
VHS	van Hove singularity
XPS	X-ray photoelectron spectroscopy

SUMMARY

The purpose of this work is to explore a method that combines both top-down and bottom-up elements to fabricate electronic devices made from graphene, a single sheet of carbon atoms related to carbon nanotubes and graphite. This material has garnered interest in the semiconductor industry for many reasons, including its potential for ballistic conduction, natural ambipolar (both n- and p-type) carrier transport, and impermeability to nearly all elements. However, its lack of a band gap, and a lack of viable options for creating one in the material, suggests a limited future as a silicon replacement material. A solution to this problem is presented that uses a recently-reported technique of creating pre-patterned graphene features from the thermal decomposition of specially-structured silicon carbide (SiC) surfaces. We employ a combination of direct band structure measurements and electrical results to suggest that a semiconducting bent graphene nanostructure exists in this structured SiC system, creating a possible route toward a broad class of future graphene electronics.

In Chapter I, we give a simplified view of the electronic properties of graphene as well as common growth techniques, with special emphasis on the SiC growth method. Chapters II and III further explore the electronic properties of the material. In Chapter II, it is shown that multilayer graphene on a particular face of SiC behaves as a series of nearly ideal, decoupled sheets,[1] using it further to test theoretical predictions about the electronic properties of bilayer graphene.[2] Chapter III probes the effects of radiation damage in the material while simultaneously shedding new light on how electrical conduction occurs in multilayer graphene films on SiC.[3]

Chapter IV first presents the idea of creating graphene from structured SiC, building upon previous work to create highly-ordered, dense arrays of graphene lines through precise surface diffusion control. Using this system, we obtain the first band structure measurements of graphene lines of width < 30 nm.[4] Chapter V further extends the structured graphene idea to take advantage of a newly-discovered curvature-induced semiconducting graphene region,[5] fabricating devices to demonstrate electrically that devices built around these regions have superior off-state characteristics.

CHAPTER I

BACKGROUND

Graphene is a single sheet of carbon atoms arranged in an sp^2-bonded honeycomb lattice. Three of the four valence electrons in each C atom participate in strong σ bonds with neighboring C atoms, endowing the graphene with great mechanical strength as well as chemical inertness. By contrast, the fourth electron, whose p_z orbital lies perpendicular to the plane of the sheet, is non-hybridized and contributes to electrical conduction. This π electron,[1] as it is called, is extremely mobile and, as explained in the next section, also gives graphene devices unique properties such as ambipolar (characteristic of both n- and p-type) currents composed of carriers with saturation velocities that have been shown to exceed those seen in advanced silicon devices by a factor of 5.[6]

In this Chapter, a simplified view of the electronic properties of graphene that originate from its crystal structure will first be presented. The common graphene growth techniques will then be reviewed, ultimately making the case for the superiority of graphene grown from SiC. Finally, the particular growth method used by the Epitaxial Graphene Lab, which uses an enclosure to slow down the Si sublimation from SiC, will be explained.

1.1 Electronic properties

From a crystallographic point of view, the honeycomb lattice of graphene implies a two-atom, hexagonal unit cell with two triangular sub-lattices [see Figure 1.1(a)]. Although the two sub-lattices are equivalent in the case of a single graphene sheet,

---

[1]Because the π electron is the only one that contributes to the electronic properties, we will only refer to that electron here.

they are not necessarily so when another sheet is placed on top of it, as exemplified by the case of graphite. This inequivalence leads the bands of the latter two-sheet system to become non-degenerate, as first shown by Wallace in 1947.[7] In deriving the graphite band structure in that paper, the bands of graphene were also calculated. By employing a tight-binding, or linear combination of atomic orbitals method that took into account only nearest-neighbor interactions, Wallace found that the dispersion relation of graphene can be written[2] (after some algebra) as

$$E(\mathbf{k}) = \pm t \sqrt{1 + 4\cos^2\left(\frac{k_x a}{2}\right) + 4\cos\left(\frac{\sqrt{3}k_y a}{2}\right)\cos\left(\frac{k_x a}{2}\right)}, \qquad (1.1)$$

where:

- $\mathbf{k}$ and k_i are the wavevector and vector components, respectively

- $a \approx 2.46$ Å is the magnitude of the primitive vectors of graphene

- $t \approx 3$ eV, often called the "hopping energy," is the energy barrier between neighboring atoms.[8]

The hexagonal Brillouin zone (BZ) of graphene is typically labeled with three points of high symmetry. The vertices of the zone are referred to as K or K' to distinguish between sublattices, with the so-called M points lying at the midpoint of each side. The center of the BZ is referred to as the Γ point. Plots of Equation 1.1, given in Figure 1.2, show that only at the K and K' points given by $(k_x, k_y) = \left(\pm\frac{2\pi}{3a}, \frac{2\pi}{\sqrt{3}a}\right) + m\mathbf{a}^* + n\mathbf{b}^*$, where $\mathbf{a}^* = \left(\frac{2\pi}{a}, \frac{2\pi}{\sqrt{3}a}\right)$ and $\mathbf{b}^* = \left(-\frac{2\pi}{a}, \frac{2\pi}{\sqrt{3}a}\right)$ are two choices for the reciprocal lattice vectors of graphene and where m and n are integers, does $E(\mathbf{k}) = 0$, indicating that the conduction ($E > 0$) and valence ($E < 0$) bands come in contact at those points but do not cross. The effect of this confluence is to create

---

[2]The convention of vector quantities being given in **bold** will be adopted here.
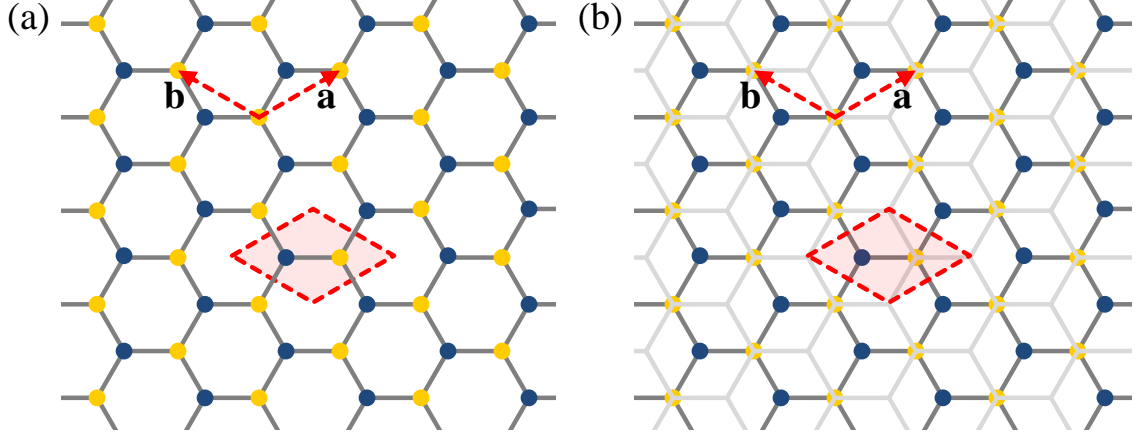
Figure 1.1: Graphene and graphite unit cells. (a) Depiction of the graphene unit cell and primitive vectors $\mathbf{a} = a\left(\frac{\sqrt{3}}{2}, \frac{1}{2}\right)$ and $\mathbf{b} = a\left(-\frac{\sqrt{3}}{2}, \frac{1}{2}\right)$ within a larger graphene sheet. Atoms belonging to different sublattices are colored differently. (b) Illustration of the inequivalence between the sublattices in the case of graphite. Only the lightly-shaded bonds of the second sheet are shown for clarity. Note how all of the atoms of one sublattice coincide with atoms from the other sheet, while those of the other sublattice do not.

a vanishing density of states at zero energy[3] and has lead graphene to be called both a semimetal and a gapless semiconductor. Despite its lack of band gap, however, its limited density of states near zero energy allows it to exhibit a pronounced electric field effect.[9]

The symmetry of Equation 1.1 about zero energy implies similar behavior between electrons and holes in the material; in practice, this similarity is most valid near zero energy. This symmetry is absent from essentially all currently-used semiconductor materials such as Si, SiGe, and the alphabet soup of III-V materials, where one carrier has a higher mobility than the other.[4] This symmetry is, in practice, difficult to observe experimentally in graphene because of methodological problems. For

---

[3] "Zero" energy will be taken here to mean where the Fermi level would lie in an undoped system. This point was historically called the charge neutrality point (CNP) in carbon nanotubes, but is often called the Dirac point in the graphene literature.

[4]In the case of III-V materials such as GaAs ($m_e^* \approx 0.067 m_e, m_h^* \approx 0.45 m_e$), the mobility asymmetry can be quite large.
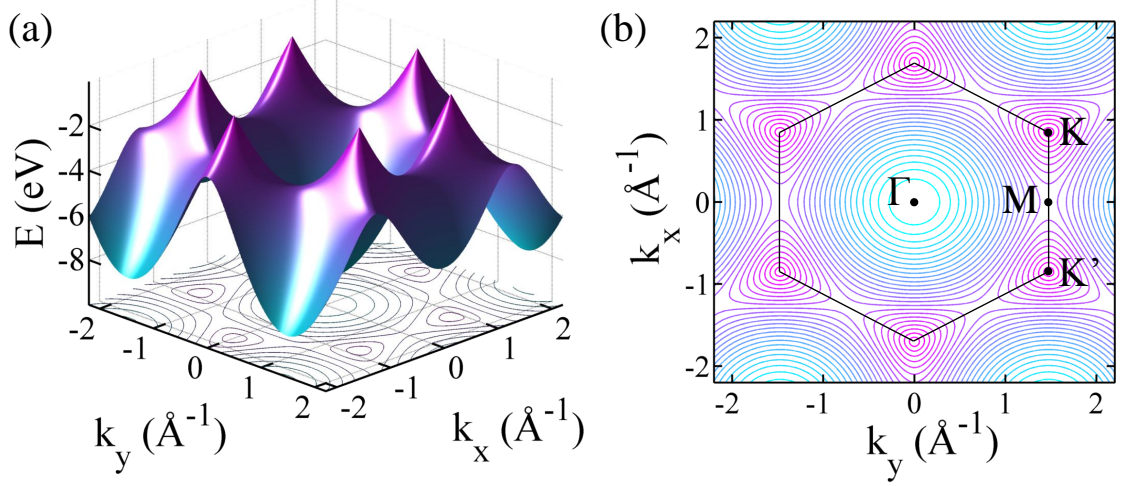
Figure 1.2: Graphene band structure and Brillouin zone. (a) A plot of Equation 1.1 for $E < 0$ that clearly shows six prominent cone-like structures near zero energy that comprise the primary region of interest for devices. (b) Illustration of the graphene BZ overlaid on a contour plot of Equation 1.1, displaying its points of high symmetry at K/K', M, and Γ.

example, nearly all studies containing current-gate voltage sweeps report an asymmetric conductivity in the electron- and hole-dominated regimes, but it is usually explained by extrinsic effects, such as p-n and p-p junctions forming at the source/drain contacts.[10]

Evaluating Equation 1.1 a small distance $\|\Delta \mathbf{k}\| \ll \frac{2\pi}{a}$ from the K points, the dispersion relation takes on the form

$$E(\mathbf{k}) = \pm \hbar v_F \|\Delta \mathbf{k}\|, \tag{1.2}$$

where $v_F = \frac{\sqrt{3}at}{2\hbar} \approx 10^6$ m/s is the so-called Fermi velocity, the speed at which electrons at the Fermi level travel on a microscopic scale, and $\hbar = \frac{h}{2\pi}$ is the reduced Planck constant. This equation describes a cone-shaped feature in the band structure that is typically referred to as the Dirac cone, after the Dirac Equation, which is a relativistic formulation of the Shrödinger Equation that predicts a linear energy-momentum relationship for massless particles and qualitatively describes the graphene bands near the K points. Because this is the only band region to lie near zero energy,

it is of primary importance for device operation.

1.2   Other properties relevant to electronics

Graphene is useful to the semiconductor industry not only for its electronic properties, but its optical and chemical properties as well; namely, it is chemically inert and highly transparent. As a result of its tiny, dense honeycomb pattern, as well as its weak chemical reactivity, graphene sheets are diffusion barriers to most chemical species, including atomic helium.[11] As a result, graphene has been studied for a variety of related applications, including corrosion coatings [12] and pore-based DNA sequencers [13]. Graphene may also be ultimate diffusion barrier for copper interconnects, which are currently made of thin layers of W, TaN, etc., a few nm thick.[14]

The material is highly opaque for its thickness of 3.35 Å, absorbing about 2.3% of incoming light over a very broad range of wavelengths.[15] However, because a single sheet is relatively conductive, it has been investigated for so-called transparent conducting applications, such as touchscreens [16] and solar cell electrodes [17]. In the latter case, transparent electrodes are useful because the sandwich structure of the typical solar cell causes opaque electrodes to block some light from reaching the middle of the sandwich where photoconversion takes place.[18]

Uniquely, the optical transparency of graphene can be tuned by changing where the Fermi level E_F lies. This tunability can be seen most simply by examining electron occupancy in the material as a function of E_F. In the relative absence of reflections,[15] the transparency of graphene at a wavelength λ is reduced when one of its electrons absorbs an incoming photon of energy $\frac{hc}{\lambda} = \hbar\omega$, where c is the speed of light and ω is the angular frequency of the photons. Following Figure 1.3(a), because photons have a small momentum, the only allowed transitions are ones from an energy $-\frac{\hbar\omega}{2}$ to ones with the same momentum at $\frac{\hbar\omega}{2}$. The transition probability $P(\hbar\omega)$ is, therefore, proportional to the product of the relative occupancy of all states
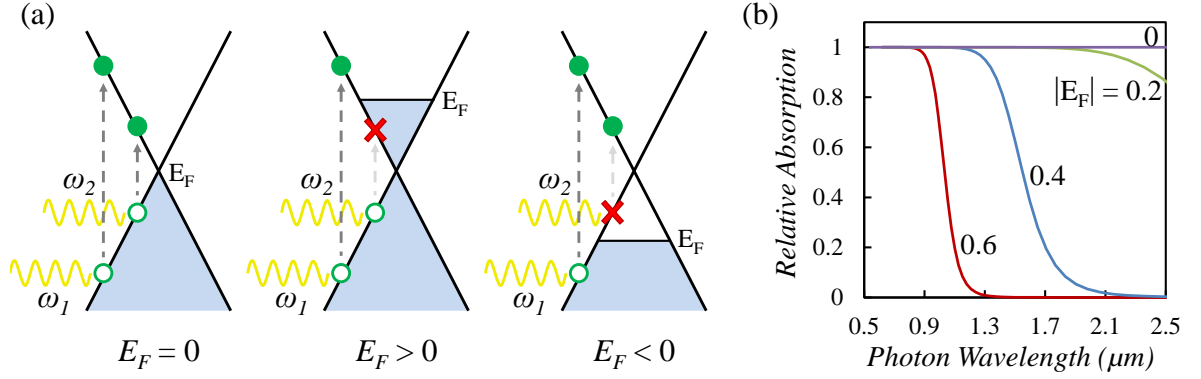
Figure 1.3: Tunable graphene absorption spectrum through doping. (a) Band structure schematic of the photoexcitation process, showing allowable electron transitions for high ($\hbar\omega_1$) and low ($\hbar\omega_2$) energy photons exciting electrons from energy $-\frac{\hbar\omega_{1/2}}{2}$ to $\frac{\hbar\omega_{1/2}}{2}$, respectively. Transitions are suppressed when $\frac{\hbar\omega}{2} < |E_F|$. (b) A relative plot of Equation 1.3 for $T = 300$ K in the optical to infrared range for various E_F from 0 to 0.6 eV.

at $E = -\frac{\hbar\omega}{2}$ and the relative *vacancy* of all states at $E = \frac{\hbar\omega}{2}$ as

$$P\left(\hbar\omega\right) \propto F\left(-\frac{\hbar\omega}{2}\right)\left[1 - F\left(\frac{\hbar\omega}{2}\right)\right] \tag{1.3}$$

where $F\left(E\right) = \frac{1}{1+\exp\left(\frac{E-E_F}{k_B T}\right)}$ is the Fermi-Dirac function, k_B is the Boltzmann constant, and T is the temperature relative to absolute zero. We can use this simple relationship to extract the salient features of the optical transmission spectrum of graphene because all material-dependent parameters, as well as photon energy, cancel out in more complete approximations that take into account the interaction strength between the light and the graphene electron states.[15, 19][5]

A quick inspection of Equation 1.3, plotted in Figure 1.3(b) for various values of E_F, confirms that the transition probability, and therefore photon absorption rate, varies widely, depending upon doping. For $\frac{\hbar\omega}{2} \gg |E_F|$, the effect of doping on the absorption is negligible.[6] However, when $\frac{\hbar\omega}{2}$ is comparable to or less than $|E_F|$, either

---

[5]This statement is only valid for linear bands, and so we are careful to restrict our analysis to the optical regime. In the deep ultraviolet range, photoexcitation occurs where the graphene band structure becomes highly nonlinear. On the other end, in the deep infrared range, low energy excitations such as plasmons begin to drastically increase photoabsorption.[20]

[6]For reference, a photon with wavelength 1 μm has energy $\hbar\omega \approx 1.2$ eV.

the lack of occupied valence band states ($E_F < 0$) or lack of unoccupied conduction band states ($E_F > 0$) begin to inhibit absorption, increasing the transparency of graphene in that range. This interesting phenomenon allows for the possibility of making graphene even more transparent while simultaneously making it more conducting, a similar behavior to that seen in transparent conducting oxides (TCOs), which are the current standard material for transparent conducting applications.[21]

1.3 Growth techniques

Over the last decade, several techniques for the creation or isolation of graphene have proliferated, including using scotch tape to peel off the top layers of highly-ordered pyrolytic graphite (HOPG),[9, 22] sublimating Si from SiC to create so-called epitaxial graphene,[23] chemically reducing graphene oxide created by the well-known Hummers method,[24, 25] and, more recently, performing chemical vapor deposition (CVD) of hydrocarbons on foils made from a variety of metals, including Ni,[26] Cu,[27] and Ru [28]. Of these methods, only the CVD and SiC growth methods stand out at first glance as commercially viable for electronic devices; the scotch tape method has throughput issues, while reduced graphene oxide exhibits poor conductivity.[29] Figure 1.4 gives a visual comparison of the graphene produced by each of the aforementioned methods.

The Si sublimation from SiC method is unique in that the graphene is, as grown, ready for processing on a wafer scale. Unlike CVD-grown graphene, the SiC-grown graphene is believed to be a continuous sheet across the wafer. As a result, epitaxial graphene has been the subject of many important graphene device papers, including demonstrations of the first GHz-frequency transistors,[32] as well as a number of operating frequency records.[33, 34] However, the size of a single graphene sheet is limited by the wafer size, making graphene on SiC less appropriate for applications requiring extremely large areas, such as touchscreens. Given that CVD-grown graphene
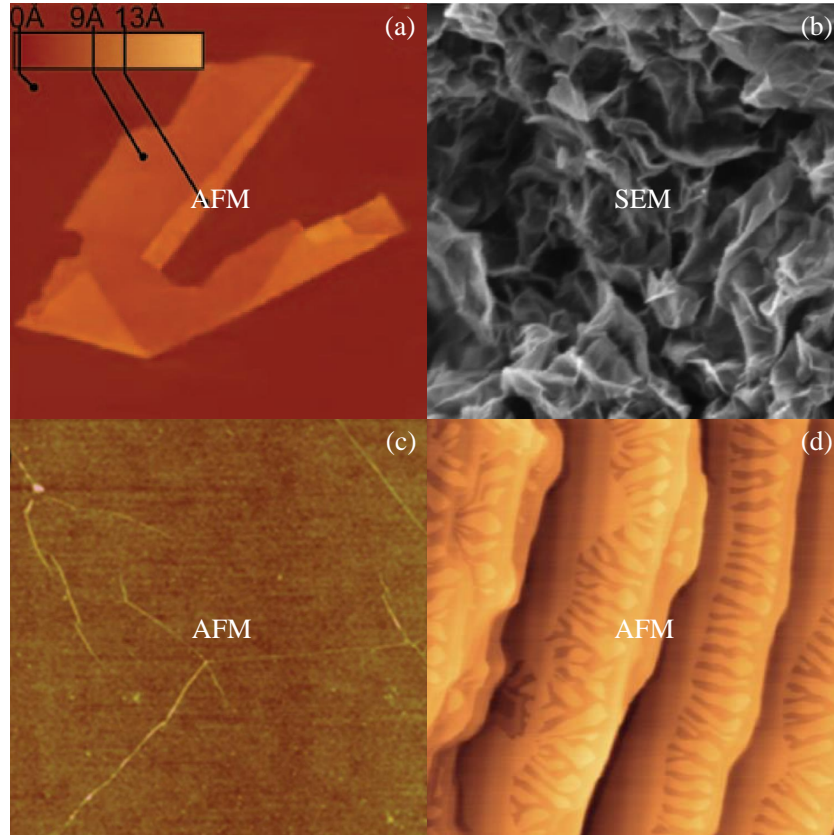
Figure 1.4: Comparison of graphene films grown by various methods: (a) mechanical exfoliation, (b) reduction of graphene oxide, (c) chemical vapor deposition, (d) decomposition of SiC. The relative scale of each image is within an order of magnitude. Taken from References [22], [29], [30], and [31], respectively.

can easily reach large (meter-scale) areas,[16] the CVD and SiC growth methods are complementary: CVD for large areas, and SiC for high quality.

1.3.1 Mechanical exfoliation

Mechanical exfoliation, or the "scotch tape method", was the technique used in many of the seminal papers on graphene.[9, 22, 35, 36] It quickly gained popularity because of its minimal overhead costs yet ability to produce graphene capable of displaying a variety of physical phenomena such as the quantum Hall effect (QHE) [35] and Aharonov-Bohm (AB) oscillations [37]. The method itself is a re-framing of an established technique to remove the topmost layers of HOPG, exposing a clean surface for use in vacuum-based surface analyses of that material. Essentially, a piece of scotch tape is placed, sticky side down, on a piece of HOPG, lifted, and then deposited, face down again, onto another substrate. The deposits may then be sonicated and rinsed to further reduce the number of layers in the deposited flakes.[7] With luck, suitable monolayer flakes will be found after an exhaustive search using some form of microscopy.

A few key downsides keep mechanical exfoliation from moving beyond the lab. First, the nominal size of a graphene flake isolated by this method is on the order of microns,[9] with large distances between flakes, precluding its use for all but the tiniest electronic devices. Second, what few flakes that are deposited may be one or more layers, requiring a tedious search process to find a suitable monolayer piece with which to work. Finally, the graphene tends to be of lower quality than that produced by other methods; exoliated graphene has been shown to deteriorate under even soft x-rays,[38] making a number of x-ray-based measurements difficult to perform. For all of these reasons, the share of work using exfoliated graphene has dropped precipitously over the last few years as the field has matured and demanded progressively more

---

[7]See the supplemental information for Reference [9].

sophisticated studies.

1.3.2 Reduction of graphene oxide

Reducing graphene oxide has proved popular for some applications, particularly those involving composites or thick aggregated films.[24, 39, 40] In a common process, bulk powder graphite is oxidized through the Hummers method, which involves mixing the graphite with sodium nitrate ($NaNO_3$) in a bath of sulfuric acid (H_2SO_4), slowly stirring in potassium permanganate ($KMnO_4$).[25] The resulting mixture, referred to in the literature as graphite oxide or graphitic oxide, disperses readily into single sheets in water, owing to its hydrophilic nature,[24] to form graphene oxide. The oxygen can then be removed from the sheets by adding a strong reducing agent such as hydrazine hydrate (N_2H_4).[24] However, using this method, it is impossible to isolate a single sheet because the dispersed graphene sheets re-agglomerate once reduced.[29] One reported way to avoid this problem is to oxidize instead an already-isolated sheet, such as monlayer graphene on SiC, and "draw" the desired reduced graphene oxide pattern using a heated nanoscale tip.[41]

The greatest drawback to graphene produced by this method is the large number of defects,[29] and, consequently, its poor conductivity. Reduced graphene oxide created from oxidized graphene on SiC, for example, has a sheet resistance on the order of 100 times larger than that of the non-oxidized material.[23, 41] Strong oxidation reactions are well known to attack the graphene lattice, allowing for effects such as the "unzipping" of carbon nanotubes into narrow graphene strips.[42] To compete with other methods of production, a method to repair the lattice, e.g., through annealing, should be devised.

1.3.3 Chemical vapor deposition

The general process of CVD involves flowing a gas across a substrate in a high temperature environment, causing the gas, through dissociation or reaction, to leave a

particular chemical species on that substrate.[43] The gases of choice for graphene growth tend to be either ethylene (C_2H_4) or methane (CH_4). The mechanism of CVD growth of graphene involves either direct C adsorption, as in a "conventional" CVD process,[27] or the dissolution of C in another material at high temperatures and subsequent precipitation during cooling.[26, 28] The solubility of carbon in most metals is quite high at graphene growth temperatures, requiring that the amount of carbon either dissolved or precipitated out be tightly controlled to ensure only monolayer graphene forms.[44] However, the solubility of carbon in Cu is so low that no dissolution actually occurs, causing only a single layer of C to adsorb onto the Cu surface, constituting a highly self-limiting process.[45] Cu foils are therefore useful when monolayer graphene is desired, but if a thicker film is needed, then Ni, Ru, or other metal foils would be preferable.

There are two main benefits of the CVD method: compatibility with existing semiconductor processing, and scalability. Regarding the former, growth can be done in many commercial CVD systems using inexpensive, high-purity hydrocarbon gas. For the latter, because metal foils can be made arbitrarily large, the CVD process can be scaled up to very large areas; indeed, a roll-to-roll CVD process has been used to create meter-scale areas of graphene inexpensively.[16] For these reasons, CVD graphene currently seems to enjoy the largest share of interest among the graphene growth methods.

The quality of CVD-grown graphene is limited by a couple of factors. First, the graphene cannot be used as-grown; it must be transferred to an insulating substrate, which can introduce tears in and contamination on the graphene. For example, $FeCl_3$, commonly used to etch away the metal foils after CVD growth, is a known graphite intercalant,[46] and so graphene films treated with this — or any other known intercalant — could be especially difficult to clean. More importantly, the graphene

domain size is fixed to the average distance between growth nucleation sites, ultimately limiting the conductivity across a sheet.[47]

1.3.4 Decomposition of SiC

The observation that extremely thin, carbon-rich films could be formed by the sublimation of Si from SiC dates at least to 1965 with the work of Badami [48]. Perhaps the most compelling early work, which elucidated the disparate growth on the two polar faces of SiC, was done in 1975 by van Bommel, et al.[49] In that study, low-energy electron diffraction (LEED) and Auger electron spectroscopy (AES) were used to study SiC[8] (0001) and (000$\bar{1}$) (also known as the Si- and C-faces, respectively) that had been subjected to heating from 100 °C up to 1,500 °C in ultra-high vacuum (UHV). On the (0001) face, a blanket $6\sqrt{3} \times 6\sqrt{3}R30°$ reconstruction formed on the SiC surface by 800 °C, eventually forming single-orientation graphite by 1,500 °C. By contrast, domains of 2×2, 3×3, and 4×4 reconstructions formed instead for SiC (000$\bar{1}$) before eventually forming what appeared to them by LEED to be rotationally-disordered graphite, as a ring-shaped pattern, rather than discrete points, was observed after heating to 1,500 °C.[9] Further, the films grown on SiC (000$\bar{1}$) were much thicker, all other conditions being equal.

From the outset, it has been clear that graphene grows differently on the two polar faces. As explained further in Chapter II, these differences have a profound effect on the electronic properties of films grown on the two faces. For example, bilayer graphene grown on the Si-face forms a band gap, while on the C-face it tends to remain as two mostly independent sheets of graphene, retaining individual Dirac cones for each layer.[1] This "decoupled"[10] nature of C-face films allows them to

---

[8]Here, all references to SiC will be to the *hexagonal* (H) polytype.

[9]Van Bommel probably grew "graphene" in a contemporary sense, but until 2004, such terms as "few-layer graphite" or "monolayer graphite" were used to describe thin stacks of graphene sheets.

[10]Here we mean decoupled strictly in an *electronic* sense. There is no evidence to suggest that layers are *mechanically* more weakly coupled than on the Si-face.
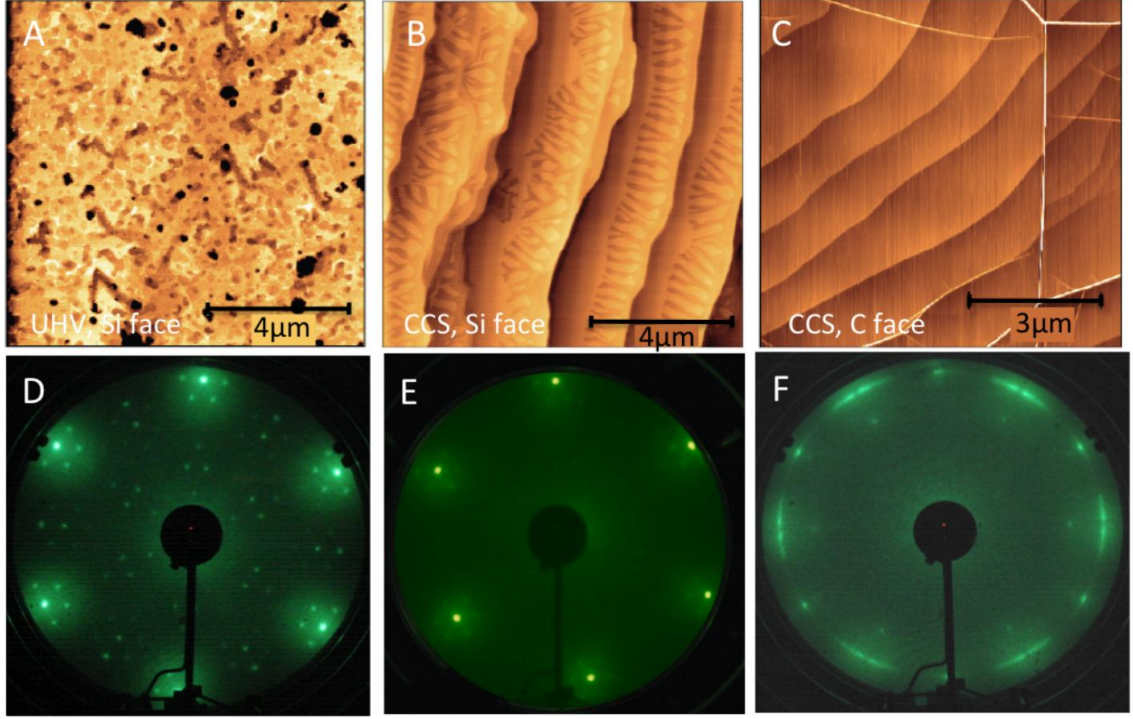
Figure 1.5: Comparison of graphene films grown on SiC characterized by atomic force microscopy (AFM) and LEED. UHV-grown Si-face films (A, D) contain small domains of either a $6\sqrt{3} \times 6\sqrt{3}R30°$ reconstruction (sixfold-symmetric spots around each graphene spot) or graphene. CCS-grown Si-face films (B, E) have much larger domains. The film is relatively uniform, although thicker finger-like areas extend from the SiC step edges. By contrast, CCS-grown C-face films (C, F) are uniform and continuous over large areas — even over step edges. This observation, in addition to band structure measurements, have led many to refer to the sheets in C-face films as "decoupled" from both the substrate and each other. Taken from Reference [31].

possess mobilities at least an order of magnitude larger than those seen in a monolayer film on the Si-face.[50]

Since the early days, refinements have been made to the basic silicon sublimation method to produce high-quality films with room-temperature mobilities of 250,000 $cm^2V^{-1}s^{-1}$ on SiC $(000\bar{1})$.[50][11] Although many groups continue to use UHV-grown graphene, the mobilities from Reference [50] were measured on graphene grown by a method that uses an ambient Si pressure to better control the Si sublimation rate. This method, dubbed confinement-controlled sublimation (CCS), encloses the SiC

---

[11]For reference, $\mu_e \approx 1,400$ $cm^2V^{-1}s^{-1}$ and $\mu_h \approx 450$ $cm^2V^{-1}s^{-1}$ at room temperature for Si.
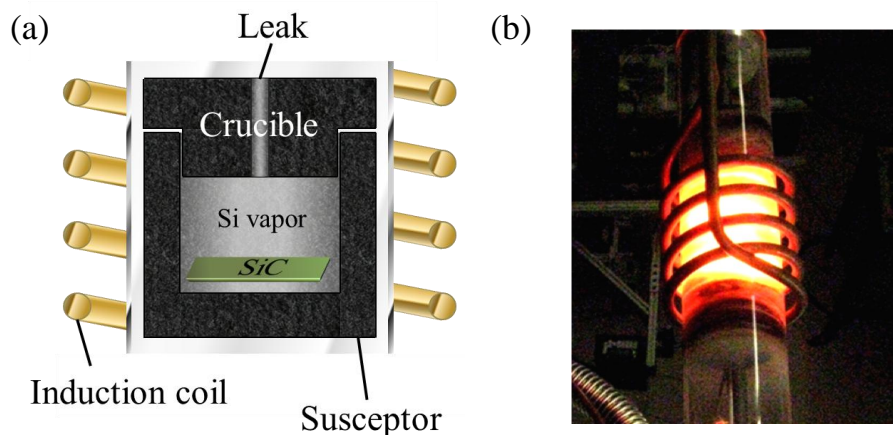
Figure 1.6: An archetypal CCS furnace. (a) Schematic of the furnace used in the CCS method. (b) Furnace in operation. Films are grown by the CCS method at much higher temperatures — >1,500 °C — compared to 1,200 °C for UHV. Reproductions of figures 1(B) and (C) from Reference [31].

chip in a mostly-hollow crucible that contains only a small hole from which sublimated Si can escape.[31] In doing this, a significant atmosphere of Si vapor develops within the enclosure, lowering the rate at which new Si sublimates from the surface of the SiC to the rate at which the Si leaves the hole (in equilibrium).[12] Consequently, compared to UHV growth in a completely open chamber, the graphene growth rate using the CCS method is much slower and, because it is slower, growth temperatures can be increased without sacrificing the ability to create very thin films. As shown in Figure 1.5, these higher growth temperatures increase film quality by smoothing out pits in the SiC caused by microscopic variations in the Si sublimation rate as well as by annealing out film grain boundaries that plague UHV-grown graphene.[31, 51] The archetypal CCS furnace is given in Figure 1.6(a).

---

[12]The idea of introducing or maintaining gaseous species within the growth chamber is not unique to the CCS method. Atmospheres of noble gases [51] as well as silane [52] have also been used for a similar effect.

CHAPTER II

WEAK COUPLING IN GRAPHENE FILMS ON SIC $(000\bar{1})$

As mentioned in Chapter I, it has been clear for decades that graphene grows differently on the two polar faces of SiC.[49] After 2004, because of its relative ease of growth, most SiC groups concentrated on the (0001) face, finding that films on that face with more than one layer behaved like few-layer graphite.[53, 38] This discovery was facilitated by the use of a surface technique called angle-resolved photoemission spectroscopy (ARPES) that can, essentially, directly image the occupied electron states in a material, thereby imaging much of its band structure below the Fermi level. Until 2009, when the first ARPES images were taken of high-quality graphene on SiC $(000\bar{1})$, it had not been clear what impact the sheet rotational disorder in those films, observed decades before by LEED, had on the electronic properties of the material. As it turns out, the disorder serves to make the stack behave like a series of nearly ideal graphene sheets that following a quasi-ordered stacking sequence,[1, 54] arguably constituting a distinct allotrope of carbon. With this observation, the terms *few-layer graphite* (FLG) and *multilayer epitaxial graphene* (MEG) have been coined to denote films grown on SiC (0001) and $(000\bar{1})$, respectively.

We present in this Chapter some of the original ARPES data on MEG, elucidating how, even as a multilayer film, it behaves as a series of nearly ideal, decoupled sheets.[1, 2] We use this system to test theoretical predictions made about the drastic effect of small relative twist angle on the electronic structure of two-layer graphene, finding in ARPES that there are minimal consequences.[2]
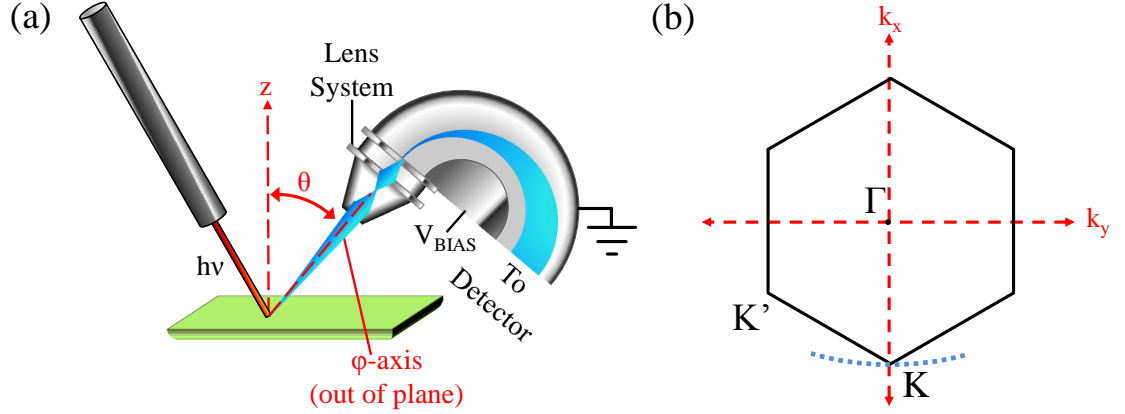
Figure 2.1: ARPES detection setup on the Cassiopée beamline. (a) Schematic of the ARPES detector. The angle ϕ used to resolve in-sample-plane momentum is coming out of the plane of the figure and the axis is oriented at an angle θ relative to the z-axis. A narrow slit (not shown) exists past the lens system at the entrance to the hemispherical analyzer that admits a large angular spread of electrons in ϕ but only a small window in θ. (b) Depiction of a typical region of k-space (blue dashed arc) in which electrons are actively collected as a result of the configuration of the figure on the left. See Equation 2.3.

2.1   Angle-resolved photoemission spectroscopy (ARPES)

When investigating the electronic properties of a material, it is useful to have a tool that can directly image the band structure. ARPES is a photon-in/electron-out characterization technique that uses an electron energy analyzer that is additionally sensitive to the angle at which the photo-excited electron was liberated from the material to construct its energy vs momentum diagram. The kinetic energy KE of an ejected electron is given by

$$KE = \hbar\omega - \Phi - BE = \frac{(\hbar k_{tot})^2}{2m_e},\tag{2.1}$$

where $\hbar\omega$ was the impinging photon energy, Φ is the material work function, and BE is shorthand for "binding energy", the distance below E_F from which the electron was ejected. Writing KE in terms of total wavenumber k_{tot} and using mass-energy units for the electron mass m_e, we obtain

$$k_{tot} = \frac{\sqrt{2m_e}}{\hbar}\sqrt{KE} \approx 0.512\sqrt{KE} \ (\text{Å}^{-1}). \tag{2.2}$$

Following Figure 2.1, if we are looking at a strictly 2D material, the band structure has no dependence on k_z,[1] and so we care only about the in-plane components k_x and k_y of the vector $\mathbf{k_{tot}}$, which are

$$k_x \approx 0.512\sqrt{KE}\sin\theta\cos\phi \ (\text{Å}^{-1}) \tag{2.3a}$$

and

$$k_y \approx 0.512\sqrt{KE}\sin\phi \ (\text{Å}^{-1}). \tag{2.3b}$$

Note that θ and ϕ are real space angles. For the work discussed here, all ARPES measurements were taken on the Cassiopée beamline at Synchrotron SOLEIL in Gif-sur-Yvette, France. The detector is a $\phi = \pm15°$ acceptance angle Scienta R4000 detector with resolution $\Delta E < 1$ meV and $\Delta k \approx 0.01$ Å^{-1} at $\hbar\omega = 36$ eV, the photon energy at which all data were taken. At this energy, the mean electron escape depth is on the order of one graphene layer,[55] and so 3-4 layers is the practical observation limit. All measurements, unless noted otherwise, were taken at 100 K. The total measured instrument resolution is $\Delta E < 12$ meV, and the ARPES beam size is about 40 μm.

Although similar, ARPES does *not* produce a diffraction pattern like LEED. In the case of the generic honeycomb lattice in Figure 2.2(a), this leads to a key difference in the orientation of the BZ as seen in ARPES relative to the diffraction pattern as seen in LEED, as shown in Figure 2.2(b). ARPES gives a true reciprocal space image of the sample, while the diffraction pattern from LEED merely displays a projection of all degenerate points of the initial beam momentum. The latter, as it turns out, produces an apparent honeycomb-like pattern that looks rotated 30° with respect to

---

[1]This statement is not true for multilayer films on SiC (0001), where the bands do have some k_z dependence because of the highly-ordered stacking of the sheets.[53]
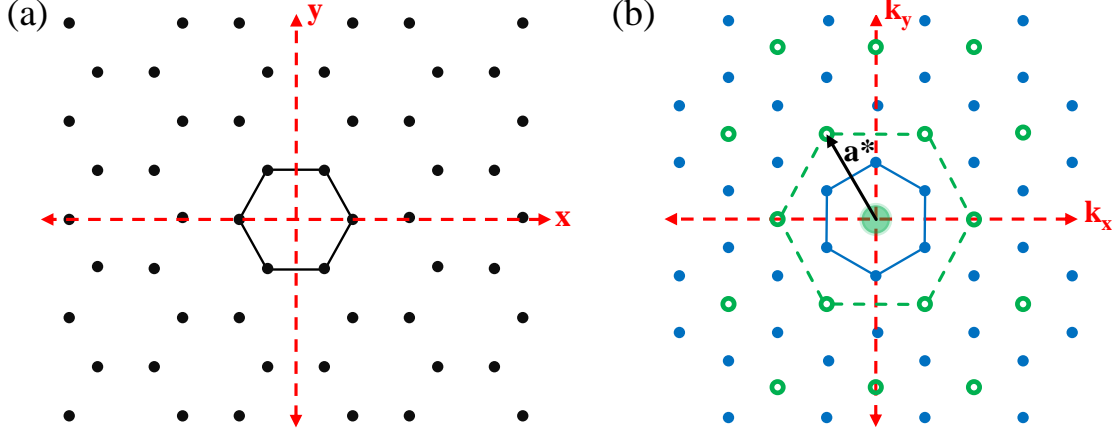
Figure 2.2: Comparison between LEED and ARPES data for a honeycomb lattice. (a) Real space lattice. (b) Reciprocal lattice (blue ●, solid hexagon) corresponding to the K points as seen by ARPES for the case of graphene. The pattern formed by connecting similar points of every honeycomb in the reciprocal lattice (green ○, dashed hexagon) using a translation vector a^* is what is seen by LEED or any other diffraction-based technique. The overall effect is that the first-order LEED diffraction honeycomb and the BZ in ARPES are rotated by 30° relative to each other in the graphene system.

the true reciprocal lattice. This distinction becomes important when attempting to correlate features seen in any diffraction technique with ARPES data.

Finally, it is important to note that for our ARPES experiments, SiC heavily n-doped with N atoms to a level of $n \approx 2 \times 10^{18} \mathrm{cm}^{-2}$ was used. This type of SiC is conducting in a reasonable temperature range and ameliorates the effect of substrate charging that results from liberating so many electrons from the sample surface during ARPES.

2.2 Properties that make graphene on $SiC\left(000\bar{1}\right)$ nearly ideal

Figure 2.3 demonstrates the stark difference in band structure between films grown on opposite polar faces of SiC.[2] The graphite-type stacking sequence[3] of the sheets

---

[2]As shown in Figure 2.1(b), any ARPES data, unless otherwise stated, are taken along an arc that is roughly perpendicular to the $\Gamma - K$ direction.

[3]This stacking sequence, whereby successive graphene sheets are successively stacked by centering each carbon hexagon on an atom from the previous sheet, is also commonly referred to as either AB
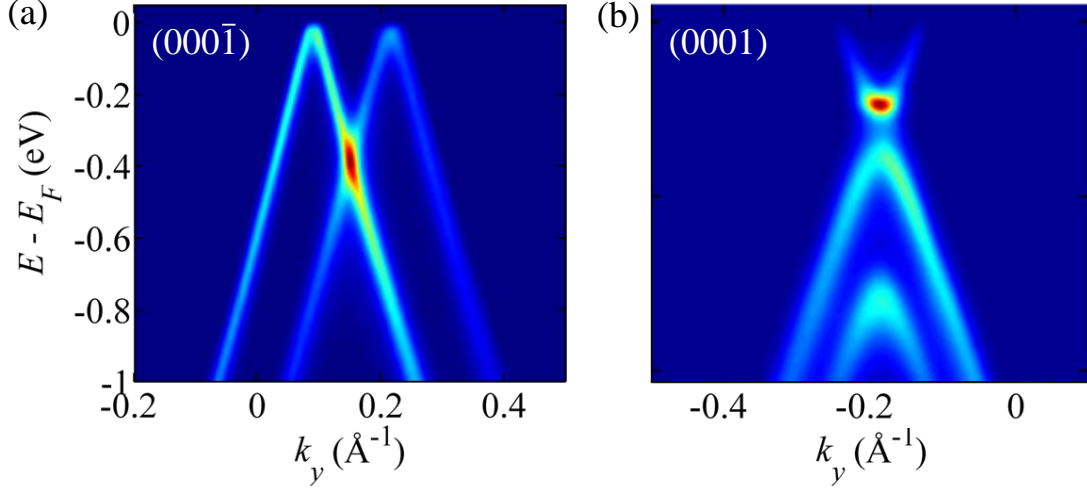
Figure 2.3: Qualitative comparison between the band structures of MEG (a) and FLG (b). Note the prominent subband in the FLG band structure caused by the sublattice symmetry breaking. FLG image courtesy P. Soukiassian.

in the case of FLG leads to a complete breaking of the symmetry between the two triangular sublattices (see Figure 1.1), splitting their degenerate bands into two subbands, creating a 0.1 eV band gap, as well as reducing the Fermi velocity[4] to 8×10^5 m/s. No such symmetry breaking is apparent here for the graphene grown on MEG, as two cones with K points rotated by some amount appear not to interact with one another — at least to within the energy resolution of the tool. Both ARPES and surface x-ray diffraction (SXRD) data suggest that the amount of graphitic stacking in MEG is limited to about 20% of the sheets.[54]

Aside from a qualitative picture, MEG exhibits several quantifiable properties that are very similar to those of an ideal, theoretical graphene sheet. First, although films with less than 4 layers are significantly n-doped,[53, 56] beyond those, as in Figure 2.3(a), MEG sheets are nearly undoped. Typically, the Dirac point E_D is within a few tens of meV from the Fermi level. For $E_D - E_F \approx 20$ meV difference, this equates[5] to a carrier density $p \approx 3 \times 10^{10}$ cm^{-2}. This number is about a factor

---

or Bernal stacking.

[4]The Fermi velocity can be computed from the ARPES bands as $v_F = \frac{1}{\hbar} \frac{\partial E}{\partial k}$.

[5]The doping level can be calculated from $\Delta E = E_D - E_F$ by finding four times (spin, sublattice
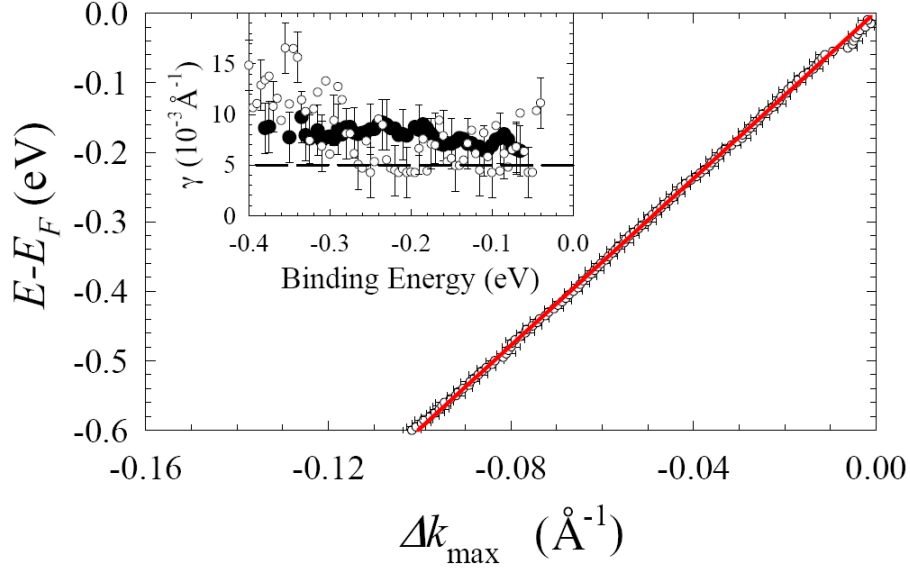
Figure 2.4: Nearly ideal cone-shaped band structure and long mean scattering times in MEG as measured by ARPES. The almost perfectly linear bands of graphene (black) can be seen to match well over a 0.6 eV window with a linear fit (red). (inset) Band half-width at half-max (HWHM) values γ in k, which are related to carrier scattering time, over a 0.4 eV energy window going up to the Dirac point at 6 K ($\bullet$) and 300 K ($\circ$). The instrument resolution (dashed line) is the limiting factor over most of the energy range. Taken from Reference [1].

of 10 lower than the $< 1.2 \times 10^{11}$ cm^{-2} reported for the same material using optical differential transmission spectroscopy.[57] It should be emphasized, however, that these *upper* limits on the doping in MEG far from the MEG-SiC (000$\bar{1}$) interface are determined by the capabilities of the aforementioned tools, and that magnetic field studies tracking Landau Level positions have reported values of $p \approx 5 \times 10^9$ cm^{-2} using far infrared (FIR) absorption [50] and $n \approx 8.8 \times 10^8$ cm^{-2} using scanning tunneling spectroscopy (STS) [58].

A second property of MEG films are the extraordinarily linear bands belonging to each layer. As first derived by Wallace,[7] an ideal graphene sheet should have a conical band structure with a Fermi velocity of 10^6 m/s within a large energy window

---

degeneracy) the area of a circle with radius $k_y = \frac{\Delta E}{\hbar v_F}$ and dividing it by the area in k-space of 1 cm^2, $\left(\frac{2\pi}{1}\right)$cm^{-2}.

and taper to a point-like apex at zero energy. Figure 2.4 plots the band peak positions of a representative MEG layer with a best fit line of about 9.5×10^5 m/s running through it, showing just how linear the band is. Some rounding off occurs in the bands near zero energy due to a slight p-doping.

Complementary to the straightness of each cone is its thickness in reciprocal space. Many factors contribute to this apparent thickness; the Fermi-Dirac function (thermal broadening), spatial fluctuations in the position of the Dirac point, as well as the instrumentation and beamline energy resolutions all broaden the bands in energy, while electron scattering times and the angular resolution of the instrument broaden the bands in momentum. The broadening in momentum space is approximately Lorentzian with a half-width at half-max γ that can reveal much about many-particle interactions in the material.[59] As a baseline, the apparent momentum broadening expected for a 31.5 eV electron[6] from the instrumentation is about $\gamma_{inst} \approx 5 \times 10^{-3}$ Å^{-1}.

The inset of Figure 2.4, which plots γ as a function of energy ascending to the Dirac point, reveals that, regardless of temperature, the band broadening is dominated by the instrument resolution within a large energy window. Outside of this window, the bands broaden with energy, consistent with a reduction in scattering time τ as a result of an increased probability of electron-electron scattering at higher binding energy.[59] The instrument resolution places a lower limit on the carrier scattering time τ within a generous window around the Dirac point of $\tau > 1/(2 \times 0.005 \times v_F) \approx 10$ fs.[7] Results from other experimental methods, however, have found that the scattering time does not come close to this lower bound, with infrared absorption [50] and transport [60]

---

[6]This is a typical kinetic energy value for an electron originating from the Dirac cone, as E_F is about 32 eV ($\Phi \approx 4$ eV) for $\hbar\omega = 36$ eV.

[7]The relationship between τ and γ relies on the intuition that a very narrow feature in momentum space becomes a very broad one in real space (and therefore in time, related by a factor of v_F), and vice versa.

both reporting values in the hundreds of femtoseconds.[8] Note that a τ of even 100 fs corresponds to a scattering length of $v_F \times 100$ fs $= 100$ nm.

2.3 Twisted graphene sheets possess ideal bands even at low rotation angles

A typical MEG film contains a variety of sheet rotations relative to the underlying SiC, as shown in Figure 2.5(a). These rotations form a tight distribution aligned with the SiC $\langle 10\bar{1}0 \rangle$ direction and, unlike FLG, form an additional bimodal distribution centered on the SiC $\langle 21\bar{3}0 \rangle$ direction, which is rotated 30° away. The precise distribution of the sheets in the $\langle 21\bar{3}0 \rangle$ direction is highly sample dependent; distribution peaks 7° from that direction are shown in Figure 2.5(c), but peaks as close as 2.2° off that direction have been reported previously.[61] This sheet rotation distribution, first observed in LEED, has been well correlated with SXRD and ARPES data, as shown in figures 2.5(c) and (d).

The relative rotation between adjacent graphene layers is widely predicted to impact on the electronic properties of the stack. Some theorists predict that v_F is heavily and monotonically reduced as the relative sheet twist θ approaches 0° (mod 60).[62, 63] Others draw a distinction between rotations that preserve the symmetry between the triangular sublattices and those that do not when determining how the twist angle affects the electronic properties.[64] The earliest work employing *ab initio* calculations predicted that there is essentially no effect for all but AB stacking,[65] although very small rotations were not explicitly considered, presumably because of the enormous computational time required for very large supercells. Depictions of possible scenarios, based on the above predictions, for a small rotation angle θ are given in Figure 2.6.

---

[8]In the case of Reference [60], transport measurements can only obtain the scattering times of the electrons within about $k_B T$ of E_F.
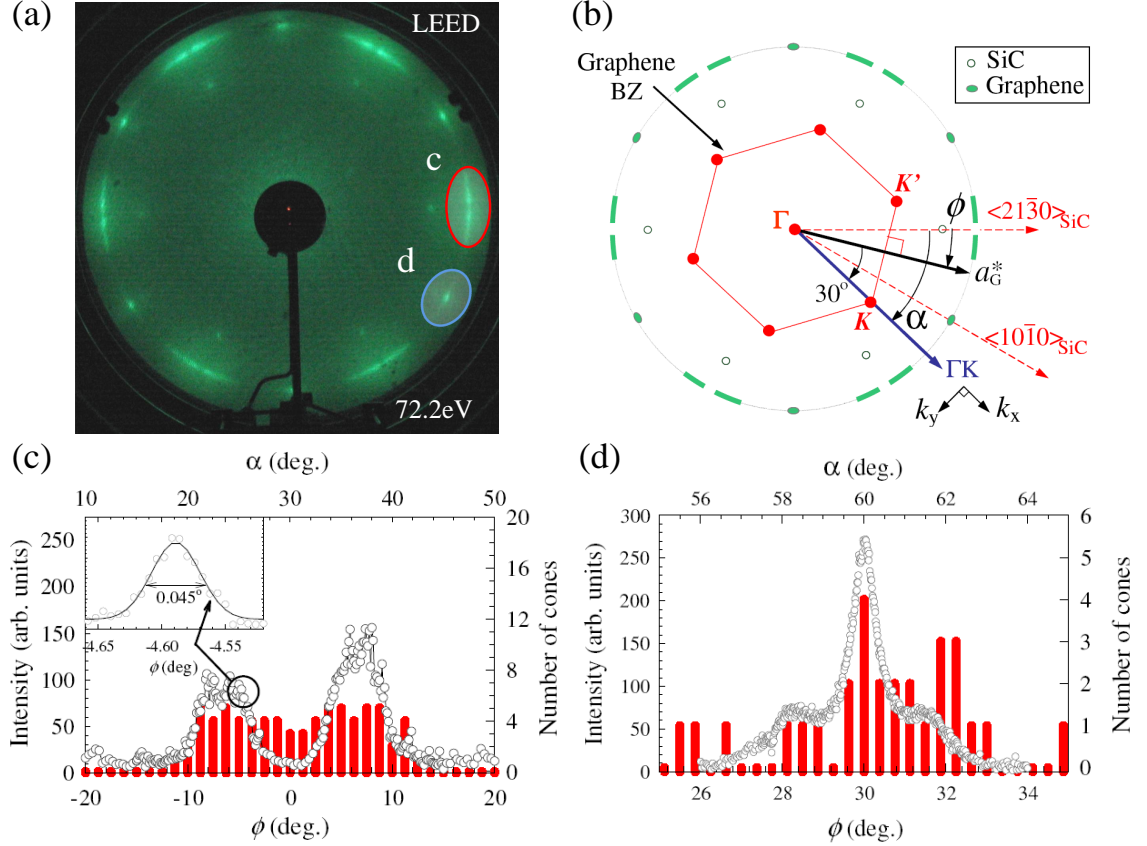
Figure 2.5: Overview of the unique distribution of sheet rotations in MEG. (a) LEED image of MEG two six-fold symmetric sets of diffuse arcs as well as the principal SiC spots at smaller radius. (b) Schematic of the LEED pattern in (a) with a superimposed BZ that is rotated by ϕ relative to the SiC $\langle 21\bar{3}0 \rangle$ direction. In (c) and (d), ARPES cone rotation histograms (bars) and SXRD data ($\circ$) are put together to corroborate the angular profiles seen in LEED at points "c" and "d", respectively, from (a). $\Gamma - K$ and the BZ translation vector a_G^* are 30° apart, and so ϕ and $\alpha = \phi + 30°$ are used to denote the respective rotations of a_G^* and $\Gamma - K$ relative to SiC $\langle 21\bar{3}0 \rangle$. SXRD data come from the Advanced Photon Source at Argonne National Laboratory on the 6IDB-μCAT beamline using $\hbar\omega = 16.2$ keV. Taken from Reference [54].
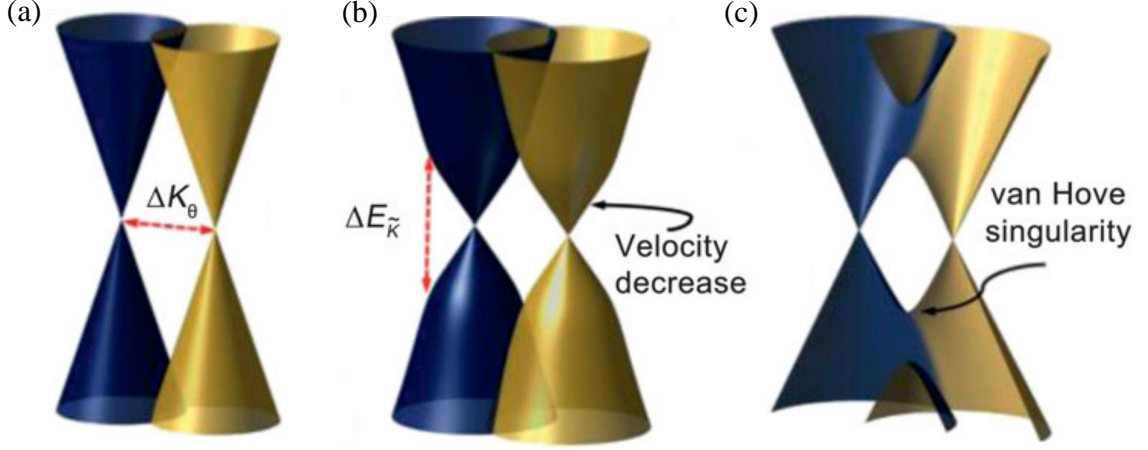
Figure 2.6: Hypothetical scenarios for band structure warping caused by interlayer interactions in twisted graphene. (a) No interaction. (b) Sharp reduction in Fermi velocity of each cone, but only within an energy window $\Delta E_{\tilde{K}}$ related to the relative rotation angle θ. (c) Van Hove singularities in the form of saddle points develop at the crossing region between the two cones. Taken from Reference [4]

The first experimental works on the subject, by Andrei, et al., interpreted the appearance of peaks in the zero-magnetic-field STS spectra of exfoliated [66] and CVD [67] graphene sheets that displayed large Moiré patterns as evidence of van Hove singularities[9] developing at the intersection of two rotated Dirac cones. Additionally, they observed an apparent reduction in v_F through Landau Level Spectroscopy (LLS) in regions where extra zero-field STS peaks were found. These results corroborated earlier tight-binding calculations made by Lopes dos Santos, et al.,[62] favoring scenario C in Figure 2.6(c).

Several recent experimental works on both CVD graphene [68, 69, 70] and MEG [71] have further supported the existence of large VHSs in twisted bilayer graphene, although, where noted, none found a decrease in v_F. These studies used a variety of techniques to identify VHSs, from the angular dependence of the Raman G peak intensity,[68, 69] to ARPES [70] and STS [71]. However, in the only study on MEG referenced above, Brihuega, et al., found VHSs only in certain areas of the supercell

---

[9]A van Hove singularity (VHS) is any region in the band structure where $\frac{\partial E}{\partial k} = 0$, causing a discontinuity in the density of states, $g(E) \propto \left(\frac{\partial E}{\partial k}\right)^{-1}$.
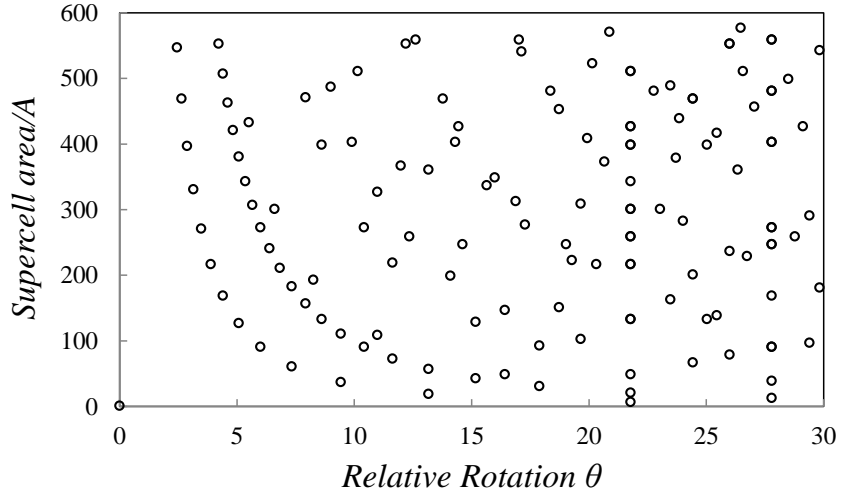
Figure 2.7: A plot of supercell area (normalized to units of the graphene unit cell area $A = \frac{\sqrt{3}}{2}a^2$) vs relative sheet rotation θ as determined by Equation 2.5 for p, q, n, $m < 100$.

BZ with high corrugation, suggesting that interlayer interactions are enhanced when the layers have rougher topography. In the case of graphene on graphite and, to a lesser extent, CVD-grown graphene, the root mean square (RMS) roughness of the surface may be on the order of 1-2 Å[72] — a significant fraction of the graphene interlayer spacing. By contrast, the RMS roughness of MEG is 0.2 Å.[73]

We present data here on MEG in which we find neither VHSs nor a reduction in Fermi velocity at small twist angles. To reconcile our data with those of the wider literature, we propose, similar to other groups [70, 71], that the smoothness of MEG results in weaker interlayer interactions, reducing their effect on the band structure. By this reasoning, MEG can be seen as an excellent testbed for theories on graphene.

2.3.1 Commensurate rotations in bilayer graphene

In special (but numerous) cases, two graphene sheets rotated by an angle θ are commensurate, forming a supercell that varies in size from as few as four atoms ($\theta = 0$) to an arbitrarily large number. By its commensurability, the supercell periodicity **c** is a linear combination of the unit cell vectors from each sheet, and so
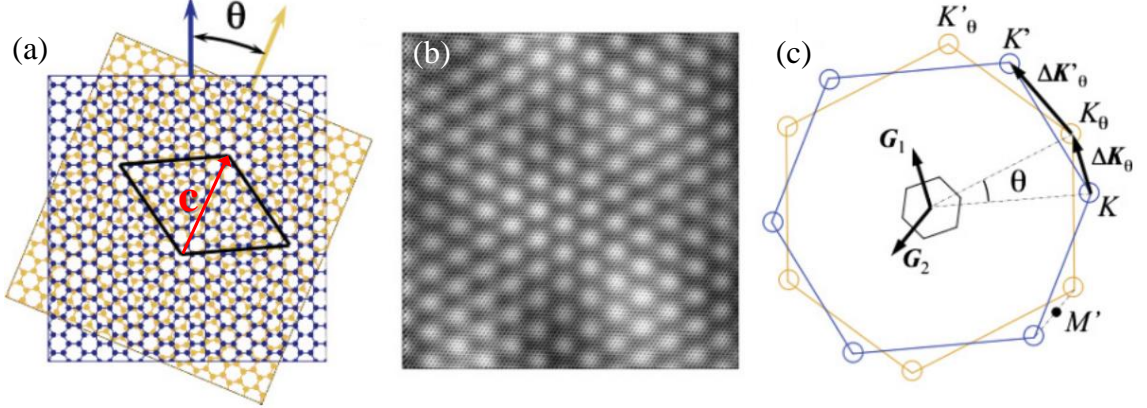
Figure 2.8: Schematics in real and reciprocal space of a Moiré pattern formed by twisted graphene sheets along with an example image from STM. (a) Schematic of two sheets rotated by $\theta = 17.9°$, showing an obvious superperiodic structure with an overlay of the supercell vector **c**. (b) A 200 Å× 200 Å STM image of a $(m, n) = (4, 5)$ supercell ($\theta = 7.34°$). Image courtesy P. N. First and J. A. Stroscio (unpublished). (c) BZs of two sheets rotated by an angle θ, showing the supercell BZ defined by the supercell reciprocal vectors $\mathbf{G_1}$ and $\mathbf{G_2}$. Taken from Reference [2]

$$\mathbf{c} = n\mathbf{a_1} + m\mathbf{b_1} = p\mathbf{a_2} + q\mathbf{b_2}, \tag{2.4}$$

where n, m, p and q are integers, and $\mathbf{a_1}/\mathbf{b_1}$ and $\mathbf{a_2}/\mathbf{b_2}$ are the unit cell vectors of the two sheets. The relative rotation θ can be calculated for a known commensurate pair from the dot product of the rightmost equivalency of Equation 2.4 using the same basis vectors on each side[10] to be

$$\cos\left(\theta\right) = \frac{\frac{3}{4}\left(m + n\right)\left(p + q\right) + \frac{1}{4}\left(m - n\right)\left(p - q\right)}{\sqrt{m^2 + n^2 + mn}\sqrt{p^2 + q^2 + pq}}. \tag{2.5}$$

Figure 2.7 plots a number of supercells and their respective sheet rotations. There is no obvious correlation between the axes, suggesting that using microscopic methods such as scanning tunneling microscopy (STM) to work backwards from supercell size to relative sheet rotation can be a difficult task without true atomic resolution. As

---

[10]There is not a one-to-one correspondence between θ and $||\mathbf{c}||$. For example, $(n, m) = (3, 5)$ and $(0, 7)$ both give $||\mathbf{c}|| = 7a$, and so it is possible to have the same sized supercell made up of different commensurate rotations.
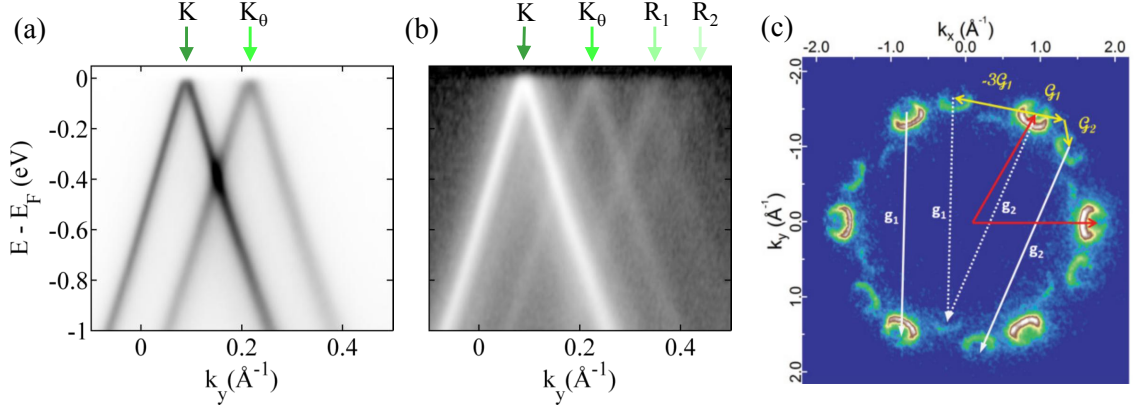
Figure 2.9: An example of the process of identifying sheet relative rotations in ARPES. (a) Two cones at K and K_θ, rotated by about 4.2°. (b) Log-intensity image at a slightly smaller θ showing the weak replica bands R_1 and R_2, a further $\mathbf{G}$ and $2\mathbf{G}$ away from K_θ, resulting from the formation of a superperiod by the relative rotation of the two sheets identified in (a). (a) and (b) taken from Reference [2]. (c) Photoemission data taken from Reference [74] of a representative rotated bilayer system showing primitive vectors $\mathbf{g}_1$ and $\mathbf{g}_2$ from the two sheets and how they create replica cones. The Dirac cones look like half-moons due to interference effects that cause photoemission supression in certain parts of the Dirac cone.[75]

depicted in Figure 2.8, a (m, n) supercell has reciprocal lattice vectors

$$\mathbf{G_1} = \frac{1}{m^2 + n^2 + nm} \left[(m + n) \, \mathbf{a_1^*} + n\mathbf{b_1^*} \right] \tag{2.6a}$$

and

$$\mathbf{G_2} = \frac{1}{m^2 + n^2 + nm} \left[-n\mathbf{a_1^*} + m\mathbf{b_1^*} \right]. \tag{2.6b}$$

The supercell BZ is therefore rotated by an angle ϕ given by $\cos(\phi) = \frac{m + \frac{n}{2}}{\sqrt{m^2 + n^2 + nm}}$ that is different from θ. Following Figure 2.8, the supercell connects the K points of the two rotated BZs by a new vector $\mathbf{G}$ which, according to Mele [64], is equivalent to either $\Delta\mathbf{K}_\theta$ or $\Delta\mathbf{K}_\theta'$, depending on whether the supercell preserves the symmetry of the two triangular sublattices in each sheet or not, respectively. Importantly, $\mathbf{G}$ need only be a linear combination of $\mathbf{G_1}$ and $\mathbf{G_2}$.[64]

2.3.2 ARPES data on MEG with identifiable relative twists

Using ARPES, it is possible to identify twisted bilayer sheets by confirming two criteria, as shown in Figure 2.9. First, as given in Figure 2.9(a), two Dirac cones must be visible and have relative intensities of about $1/e \approx 0.36$, consistent with photoelectrons originating from the next layer down from the surface. Second, there must be evidence of an interaction between the two layers, demonstrated by the existence of "replica" bands like in Figure 2.9(b). These bands arise from the new periodicity introduced by the other sheet in the bilayer system and are offset from the K points in each sheet by the primitive vectors of the other, as shown in Figure 2.9(c). The relative sheet rotation θ is found by computing the central angle subtended by the chord $\mathbf{G}$, the distance between replicas, as

$$\|\mathbf{G}\| = 2\|K\| \sin{(\theta/2)}, \tag{2.7}$$

where $\|K\| \approx 1.704$ Å^{-1} is the distance from the Γ point to the K point. It is important to note that both criteria must be met to identify a pair of rotated sheets. Without the first criterion, it would be impossible to determine θ given that $\mathbf{G}$ is a linear combination of the replica spacings $\mathbf{G_1}$ and $\mathbf{G_2}$. Without the second criterion, however, it is impossible to prove that two Dirac cones do not originate from differently-rotated domains on the same sheet — a plausible result of the ubiquitous "pleats" seen in MEG films.

Across several samples and multiple weeks of beamtime, a handful of images satisfying the criteria above for identifying rotated layers were found. Figure 2.10 plots the Fermi velocities $\tilde{v}_F$ of these cones relative to $v_F = 10^6$ m/s and compares them with theoretical data that predicted precipitous drops in $\tilde{v}_F$ at small θ, finding no correlation between $\tilde{v}_F$ and θ. The lack of reduction in $\tilde{v}_F$ is observed not only for cones that were positively identified as belonging to a particular rotation θ, but for *all* non-AB-stacked cones across all data analyzed on hundreds of images taken over
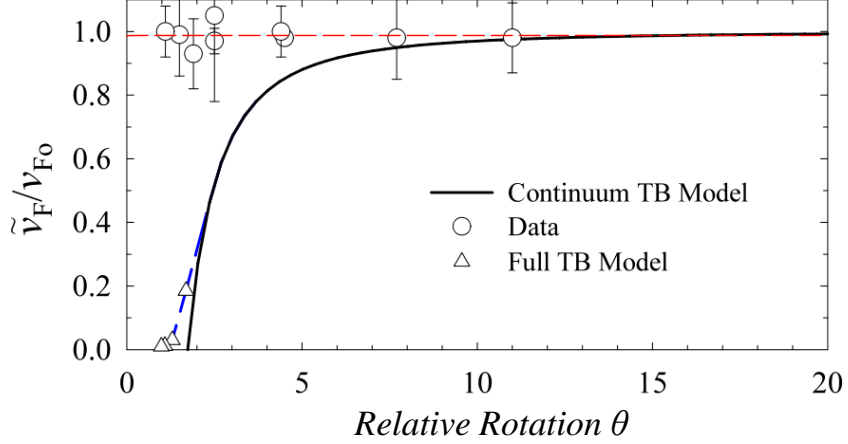
Figure 2.10: Comparison of theoretical and experimental multilayer graphene Fermi velocities as a function of relative sheet rotation. The experimental Fermi velocities were extracted from the few examples of replica bands found across all samples, showing no dropoff in v_F going down to about 1°. The solid line is from Reference [62] while the theoretical data closer to 0° ($\triangle$) come from Reference [63]. Taken from Reference [2].

multiple years. This assertion guarantees that the main point of Figure 2.10 holds true regardless of methodology for identifying rotations, barring an unperceived bias in the collected data.

Figure 2.11 addresses other predictions made about rotated pairs, namely that the band structure should be modified near the crossing point between the Diac cones from each sheet.[62] A plot of peak band intensity going down the cones from Figure 2.9 finds no deviation from an idealized cone structure, even near the crossing point around -0.4 eV down, to within experimental resolution. The dashed bands provide a rough comparison between the experimental data and the theoretical prediction made by Reference [62], showing poor agreement. The integrated intensity profile to the right is an alternate way of detecting small deviations in the band structure, given that the integrated intensity is proportional to the density of states $g(E) \propto \left(\frac{\partial E}{\partial k}\right)^{-1}$. A curve in the band structure away from the crossing point should manifest as a peak in intensity. However, not all intensity peaks correspond to curvature in the band structure. For example, a heavily-rounded peak is coincidentally centered around
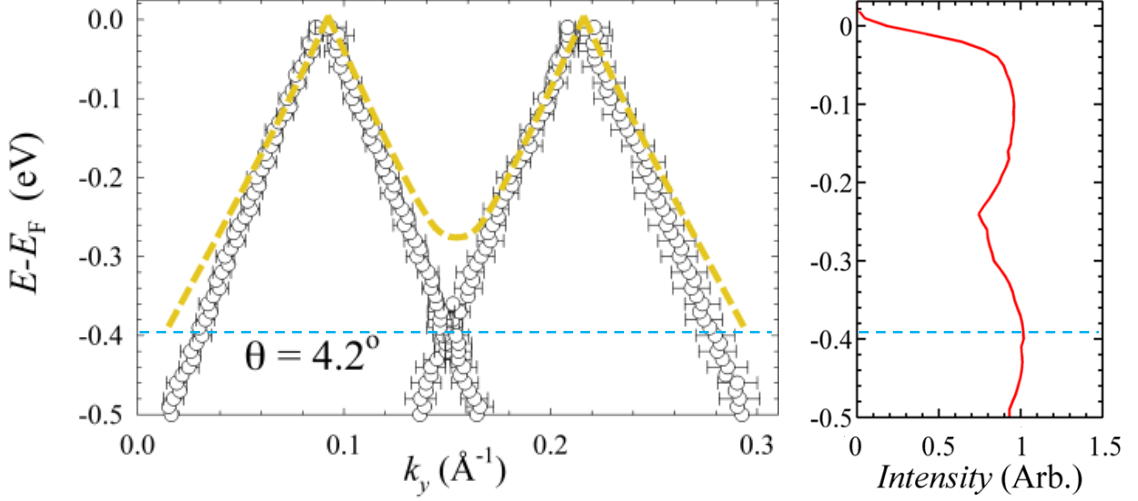
Figure 2.11: Experimental bands from a bilayer with 4.2° relative sheet rotation. (left) A plot of intensity peaks as a function of energy, with the crossing point of the bands being around -0.4 eV. The dashed curve is a rough overlay of the band shape as predicted by Reference [62]. (right) An integrated intensity profile of the figure on the left. The median intensity at each energy was subtracted in an attempt to eliminate background effects. Taken from Reference [2].

-0.4 eV in Figure 2.11, but this feature exists in many other scans, including those that depict only a single cone, suggesting its origin is unrelated to θ. Therefore, we conclude that no effect of θ on the band structure is observed.

In short, although we observe no modulations in the band structure as a result of the rotations found here, we cannot preclude the existence of small perturbations in the band structure below the practical energy limit of ARPES to detect them. We conservatively place this limit around 50 meV. This energy window is larger than the energy range corresponding to some predictions — especially for larger θ — and so further study is necessary to test that range of θ.

CHAPTER III

RADIATION EFFECTS IN GRAPHENE

Unlike terrestrial environments that are protected by the atmosphere of Earth, space is rife with highly energetic particles, ranging from protons to atomic nuclei, that are ejected from various cosmic sources.[76] The distribution in energies of these "cosmic rays" follows an approximate power law with energy, with a particle flux of about 1,000 $m^{-2}s^{-1}$ at 1 GeV, falling to about 1 $m^{-2}s^{-1}$ at 1 TeV.[77] When these particles interact with the atoms of the atmosphere, a variety of other highly-energetic particles can be created or liberated, such as photons and electrons.[78] Combined, these particles make space a hostile environment for electronics, and so various "radiation hardening" techniques, ranging from special materials selection to robust designs, have been developed to make electronics used in space more resistant to the effects of highly energetic species.

In this Chapter, we present combined electrical, topographic, and spectroscopic data of the effects of x-ray and proton radiation on MEG on SiC $(000\bar{1})$. We find that electronic quantities such as resistivity and carrier mobility are statistically unchanged after heavy x-ray bombardment despite measurable physical and chemical changes in the graphene. The damage mechanism is identified as extrinsic to the graphene itself, suggesting that epitaxial graphene on SiC is a promising platform for radiation-hardenened electronics.

3.1 Radiation effects in field-effect devices and carbon allotropes

In general, there are two radiation damage mechanisms: ionization and atomic displacement.[79, 80] In the former mechanism, electrons are forcefully ejected from atoms in the irradiated material, causing effects from transient electrical currents that interfere with circuit operation to creating highly immobile electron-hole pairs in insulating layers of the circuit ("charge traps") that affect leakage currents and threshold voltages.[81] In the latter mechanism, the increased number of lattice defects decreases carrier mobilities, but this damage vector has been considered relatively unimportant in the context of field-effect devices when compared with ionization effects.[79]

A large body of work on the effects of radiation in graphite exists due to its use as a moderator [82] — attenuating the energy of so-called "fast" neutrons — in early nuclear fission reactors.[83] However, studies on the electronic effects of radiation in carbon-based materials are relatively recent, spanning back only to the late carbon nanotube era c. 2005.[84, 85, 86] These studies found that carbon nanotubes require very high doses of lattice-damaging radiation[1] before deleterious electronic effects are observed in the nanotubes,[85, 87] while ionizing radiation primarily affects structures in the circuit aside from the nanotubes.[86, 88] Further recently-reported effects include enhanced carbon nanotube chemical reactivity in response to γ irradiation [89] and magnetism in graphite under proton irradiation [90]. In all, these studies provide guidance for work on radiation effects in graphene.

3.2 Ionizing radiation damage in graphene on SiC

Studies on ionizing radiation in graphene, proceeding in parallel with the present work, have found that, aside from extrinsic effects such as oxide charge trap formation, defects were created in the graphene by reactive oxygen species formed from

---

[1]This quantity is referred to in the literature as the *displacement damage dose* (DDD).

the ambient air during irradiation.[91, 92] One other study suggested that graphene weakly bound to a substrate, such as exfoliated graphene, is unstable even under soft x-ray irradiation, but that graphene on SiC is stable.[93] These studies, combined with its low atomic number (and, therefore, its small radiation capture cross section) and its natural integration with a wide band gap semiconductor makes graphene on SiC an attractive option as a radiation hardened electronics platform.

In this study, MEG samples approximately 7 layers thick (determined by ellipsometry [94]) and grown using the CCS method [see Figure 4.1(a)], were exposed to x-ray radiation from a tungsten source ($\hbar\omega \approx 10$ keV) in air. Half of each sample was patterned by photolithography into several eight-armed Hall bar structures for electrical and atomic force microscopy (AFM; non-contact mode) measurements, while the other half was left unpatterned for characterization by x-ray photoelectron spectroscopy (XPS; $\hbar\omega \approx 1.486$ keV) and Raman spectroscopy ($\lambda \approx 532$ nm). Before any measurements, the samples were cleaned of photoresist residue by annealing at 250 °C under 10 cc/s of forming gas (3% H_2, 97% Ar) for 2 hours.[95] This treatment eliminated all spurious (i.e., related to neither graphene nor SiC) peaks in the starting XPS spectra of the samples.

The irradiation was carried out at Vanderbilt University Institute for Space and Defense Electronics (ISDE) in an Aracor 4100 x-ray irradiator at a nominal dose rate of 31.5 krad(SiO_2)/min to reach the 12 Mrad(SiO_2) total ionizing dose (TID).[2] It is worth nothing that the dose chosen is significantly larger than what would be expected in a typical orbital environment, constituting a worst case exposure for most space-faring systems; for example, a minimally-shielded circuit in low earth orbit at an altitude of 500 km can, on the high end, expect a TID on the order of 100

---

[2]One rad, or radiation absorbed dose, is defined as the dose required to reach 100 ergs, or 10 μJ, of absorbed energy per gram of irradiated material.[80] Doses in new materials are typically specified as an equivalent dose of a reference material, such as Si or SiO_2, for easier comparisons to data from the literature.
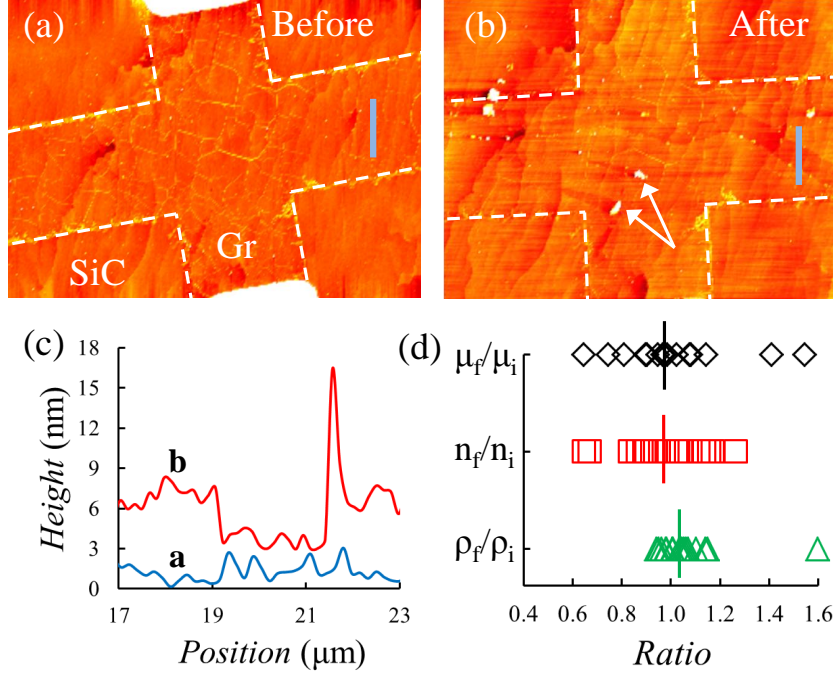
Figure 3.1: AFM and electrical measurements of MEG before and after x-ray irradiation. Non-contact AFM images of a Hall bar (the dashed line is a guide for the bounds of the structure) both before (a) and after (b) x-ray irradiation. The arrows in (b) point out areas where the graphene has locally delaminated from the surface. (c) Height profile of the blue bars in (a) and (b) extending across an area that has delaminated in the latter figure. (d) Ratios of carrier mobility μ, density n, and resistivity ρ before (subscripts i) and after (subscripts f) irradiation across many Hall bars, with the vertical lines in each row representing the median value. Taken from Reference [3].

krad(SiO_2)/year.[80]

Figures 3.1(a) and (b) show AFM maps of part of the same Hall bar before and after irradiation, respectively. In the latter image, arrows, which point out areas of high topography, form consistently at the tips of long, narrow sections of low topography, suggesting that the graphene has locally rolled up like a scroll. Figure 3.1(c), which shows topographic line profiles from similar locations in figures 3.1(a) and (b), confirms that the low topography regions did not exist before irradiation and, furthermore, that the regions are several layers deep. The exact number of layers peeled away is difficult to determine by AFM alone because x-ray induced chemical changes in the top graphene layer (see Figure 3.2) may affect the apparent height of the feature

34

in AFM.[96]

Despite the obvious physical damage done to the graphene during irradiation, Figure 3.1(d) shows that the electronic properties remain essentially unchanged. Of 16 Hall bar structures measured over 4 samples, the median free carrier mobility/concentration was found to be 3% lower and the median resistivity 4% higher, which are statistically insignificant given the spread in the data. These data represent a variety of sample qualities, with resistivities ρ ranging from 100-800 $\Omega\backslash\square$, mobilities μ between 400-4,000, and carrier concentrations n from 1-3 $\times 10^{13}$ cm^{-2} prior to irradiation. However, it should be noted that the properties of the Hall bars within a sample were relatively uniform, and that the observed lack of change in the electronic properties was independently observed independently in each sample.

Figure 3.1 presents seemingly conflicting data: AFM suggests that the graphene sustains heavy damage, but the electronic properties of the film remain unchanged. This conflict can be reconciled by supposing that the peeling of the MEG film does not extend to the bottom-most layers. It is well established that the constituent sheets of epitaxial graphene closest to the SiC are highly doped,[53, 97, 56] and so it was argued that the numbers extracted from Hall data on those films should then be dominated by those closest layers.[97] The lack of change in the electronic properties combined with AFM data suggesting either a constriction or a severing of electronic transport in the top-most graphene layers suggests that these layers are electrically shorted by those layers closest to the SiC — a direct confirmation of Reference [97].

Figure 3.2 gives spectroscopic evidence of new defects in as well as oxygen functional groups on the graphene after irradiation. Figure 3.2(a) gives a background-subtracted[3] Raman spectrum before (top) and after (bottom) irradiation. The two spectra share two peaks in common: the so-called G and 2D peaks at 1570 cm^{-1} and 2700 cm^{-1}, respectively, that are typical of graphene.[36] After irradiation, two new

---

[3]See Appendix C for background subtraction details.
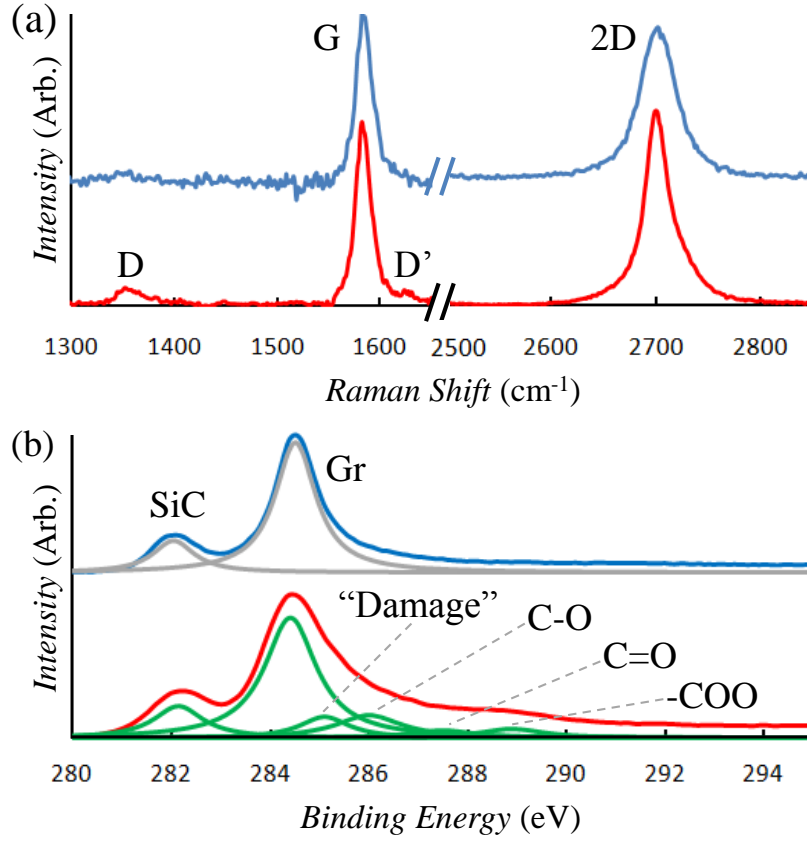
Figure 3.2: Raman and XPS measurements of MEG before and after x-ray irradiation. (a) Background-subtracted Raman spectra of bulk MEG before (top) and after (bottom) irradiation. For display purposes, the G and 2D peaks in each plot have been normalized with respect to one another. (b) C1s XPS spectra, with peak fits, of the same general area in (a) before (top) and after (bottom) irradiation. The curves are normalized and shifted to have the same integrated graphene intensity centered on 284.5 eV. Taken from Reference [3].

peaks, referred to as D and D' in the graphene literature,[36] appear around 1350 cm^{-1} and 1620 cm^{-1}, and have been unambiguously attributed to the appearance of defects, in the form of edges, in the graphene lattice.[98, 99] Aside from the natural variations in a single sample, there were no shifts or broadening of either the G or 2D peaks after irradiation.

We observe evidence of the damage mechanism in Figure 3.2(b), which presents C1s XPS spectra of bulk MEG before and after irradiation, finding that a significant number of oxygen-containing carbon species are detected. Beforehand, the C1s spectrum could be adequatey described by two peaks for C bound as SiC (282.1 eV) and as graphene (284.5 eV). Afterward, the graphene peak (284.5 eV) has widened by about 20% (1.1 eV-1.3 eV) and is asymmetric, requiring the addition of another peak at 285.3 eV to reflect surface damage.[100] In addition, a broad shoulder extends to 290 eV, which we ascribe to the contribution of at least three non-graphitic peaks at 286 eV, 287.5 eV, and 288.9 eV, attributed to particular carbon-oxygen bond configurations, namely, C–O, C=O, and –COO, respectively. These peaks have been seen after subjecting CNTs to strong oxidation reactions.[101, 102, 103] Based on the stability of epitaxial graphene to soft x-rays in vacuum,[93] we conclude that these oxygen function groups were created during irradiation rather than afterward by reactive oxygen species that formed when subjecting ambient O$_2$ to the x-rays.

Raman was further used to confirm the supposition that some, but not all, of the layers in x-ray-exfoliated regions were removed after irradiation. A scan across the peeled region in Figure 3.1(b), shown in Figure 3.3(b), reveals that the 2D peak in the peeled region falls to around half that of its intensity in the surrounding unpeeled regions. This figure of half should be treated as an upper bound because the laser used has a nominal beam size of 1 μm, and given that the peeled region is less than 2 μm in width, some contribution from unpeeled areas will be seen even when the laser is squarely over the peeled region.
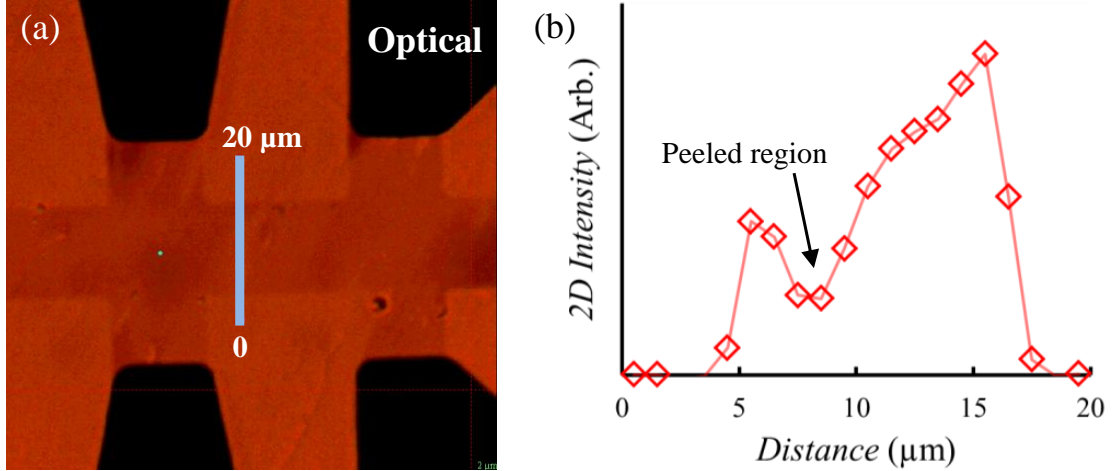
Figure 3.3: Raman line scan across an x-ray-damaged graphene region. (a) Optical micrograph of the Hall bar from Figure 3.1(b) with an overlayed line showing the location of the line scan. (b) Integrated Raman 2D peak intensity along the line shown in (a) in 1 μm increments.

3.2.1 Evidence for reactive oxygen as the damage mechanism

Strong support for surface etching by reactive oxygen species being the primary damage mechanism in the previous study was found by investigating 63 MeV proton radiation damage in MEG. The benefit of looking at this type of damage is twofold: first, protons will damage the lattice of all material far into the bulk of the SiC, providing a reference for how damage not localized to the MEG surface affects the electrical data. Second, the high energy used makes impact ionization of the oxygen in air extremely unlikely,[104] allowing us to observe whether the numerous oxygen-containing carbon species detected in XPS after x-ray irradiation will reappear in the absence of reactive oxygen. Together, these advantages will allow us to prove that x-ray irradiation in the previous study caused surface-localized etching of MEG by reactive ambient oxygen.

For the present proton study, aside from the irradiation, the methodology and measurement methods used are identical to the previous study. Irradiation was carried out in air at the Crocker Nuclear Laboratory at the University of California at

38
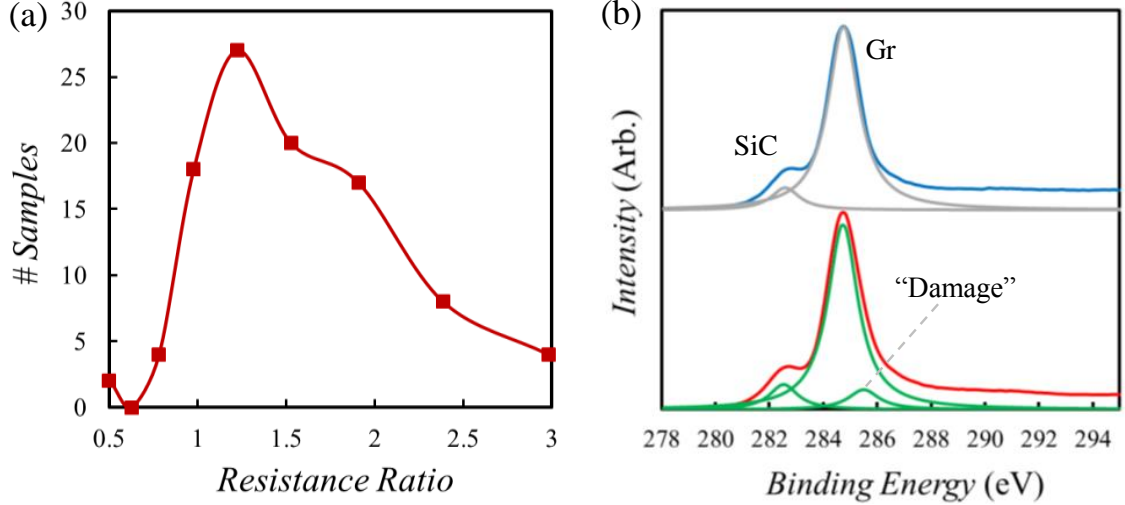
Figure 3.4: Electrical and XPS measurements of MEG before and after proton irradiation. (a) Histogram of 60 Hall bars giving the ratios ρ_f/ρ_i between their measured resistivities before (ρ_i) and after (ρ_f) irradiation. The median increase in resistivity is about 30%. (b) C1s XPS spectra, with peak fits, of bulk MEG before (top) and after (bottom) irradiation. The curves are normalized and shifted to have the same integrated graphene intensity centered on 284.5 eV.

Davis using a cyclotron source at a nominal dose rate of 1 kRad(Si)/s to reach total displacement doses of 500 krad(Si), 1.3Mrad(Si), and 3Mrad(Si)[4] on three different samples. Over the measurements presented here, however, no trends with dose were seen, and so the data are presented here in aggregate.

Figure 3.4(a), which presents a histogram of the resistivity ratios of Hall bars in MEG before and after irradiation, shows that MEG samples have a 30% higher median resivity afterward with a heavy skew toward even higher resistivities, suggesting that all layers of the samples were damaged during irradiation. These data importantly show that damage to the bottom layers — an obvious result of proton irradiation — does increase resistivity. By contraposition, if there had been no change in resistivity after irradiation, as in the x-ray experiment, then the bottom layers

---

[4]Si is a standard material for measuring displacement dose. Determining equivalent doses between protons in Si and x-rays in SiO_2, the latter of which was used for the ionizing radiation study in MEG, was outside of the scope of this work, and it suffices to state that the doses used for protons and for x-rays should have been enough to see effects in both cases.

could not have been damaged, suggesting in the x-ray study that only the topmost layers were affected by irradiation.

The C1s XPS spectrum remains mostly unchanged after irradiation, as shown in Figure 3.4(b), aside from a new "damage" peak around 285.5 eV to account for lattice damage to the MEG.[100] The many C–O bond variants seen in the x-ray study are essentially absent here, once again confirming that the x-rays had ionized ambient oxygen species that then proceeded to chemically attack the MEG surface.

CHAPTER IV

GRAPHENE RIBBONS ON HIGHER-ORDER SIC FACETS

The inherent lack of a band gap in graphene presents an obstacle to its use in areas such as digital electronics and photovoltaics. Chemical methods have so far been the experimental method of choice to endow graphene with a band gap. Popular examples, besides the aforementioned graphite oxide [29], include rehybridizing some of the π electrons by attaching to the graphene hydrogen (graphane) [105] and, more recently, fluorine (fluorographene) [106]. However, these materials are highly unstable at even 400 °C, rendering them incompatible with techniques such as rapid thermal processing that are commonly used in the semiconductor industry.

Alternatively, many experimental studies have found that graphene assumes behavior similar to that of a semiconductor when patterned it into very thin strips ("nanoribbons") by selective plasma [107] or energetic beam [108] etching of graphene sheets, or by "unzipping" carbon nanotubes using various chemical [42] or chemical-mechanical [109] means. Although on/off ratios of nanoribbon field effect transistors (FETs) are usually substantial, reported mobilities are often much poorer than reported for the basic graphene sheet, which has been understood more recently as the result of the edge roughness of the ribbons creating a series of mismatched-level quantum dots that hamstring electron movement along the length of the ribbons over a large energy range.[110] Regardless, the most popular theoretical predictions assert that even well-ordered graphene nanoribbons should have a band gap, although the

exact details are debated. For example, a density functional theory (DFT) calculation by Son, et al., held that a band gap on the order of 1 eV-nm[1] should form,[111] while an analytical approach by Brey, et al., predicted a band gap only if the ribbon length is along a particular class of directions,[112] similar to the case of carbon nanotubes.[113] Most predictions, including those of References [112] and [111] agree, however, that the exact size of the band gap depends on the edge structure.

Producing nanoribbons through the methods above are not suitable for their own reasons. Intuitively, lithographically-patterned graphene sheets will contain rough edges as a result of both the roughness of the resist as well as the stochastic nature of the plasma etching process. These edge effects drastically reduce mobilities when ribbon widths scale to tens of nm.[114] While unzipped nanotubes have boasted mobilities up to 1,500 $cm^2V^{-1}s^{-1}$,[109] the method is not scalable and faces the same problems that ultimately killed commercial carbon nanotube device ambitions, namely the lack of precise control over the placement of the nanotubes and their electronic characteristics. A method is therefore sought that is highly scalable and produces ribbons with minimal edge roughness.

In this Chapter, we extend earlier work by Sprinkle, et al., that used artificial SiC features as a template to create graphene nanoribbons with clean edges and high mobilities.[115] We find that highly-ordered arrays of these "structured graphene" ribbons can be packed densely enough to rival the modern lithographic feature densities with the right growth conditions and surface diffusion control. These arrays are used to obtain the first ARPES band images of graphene nanoribbons, providing the first direct evidence that a band gap may indeed form at extremely small ribbon widths.
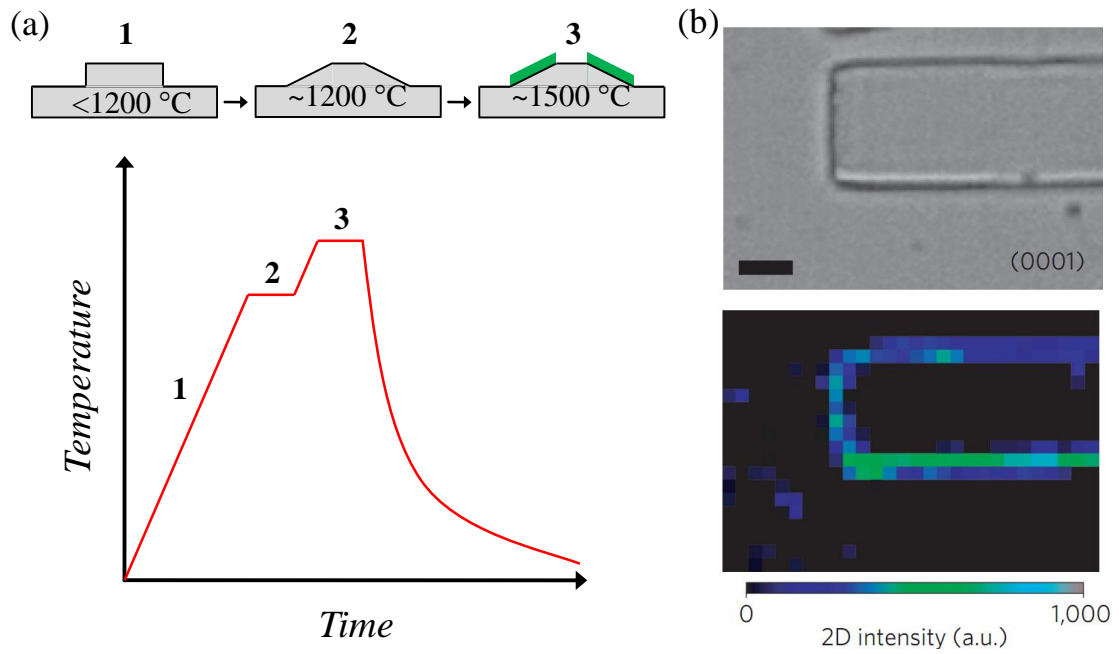
Figure 4.1: Illustration of the sidewall growth process and images of the SiC surface after growth. (a) Depiction of a typical growth process, showing what the SiC surface looks like at each step. (b) Optical image (top) and Raman 2D peak intensity map (bottom) of a raised rectangular plateau of SiC on the Si-face. The scale bar is 2 μm. Figures (b) are taken from Reference [115].

4.1 Structured graphene growth on SiC (0001)

Silicon sublimation proceeds much faster on the C-face than it does on the Si-face,[49] all other conditions being equal. It follows that other, higher-order surfaces of SiC might have disparate sublimation rates as well. In 2010, Sprinkle, et al., reported efforts to grow patterned graphene directly out of SiC.[115] They accomplished this by patterning deep (tens of nm) features into the Si face using a masked reactive-ion etching (RIE) process and then proceeding with graphene growth using the CCS method. Around 1,200 °C, the features began to flow, the walls snapping quickly from something roughly vertical to a particular higher-order crystal facet, measured from transmission electron microscopy (TEM) to have a horizontal angle of about 24°.[115] As the temperature further increased, Si began to sublimate at a quicker pace from this "sidewall" crystal facet than it did from the (0001) face, forming a complete graphene layer by the time the (0001) face contained a graphitic but non-conducting $6\sqrt{3} \times 6\sqrt{3}R30°$ surface reconstruction, typically called the "buffer" layer. The result after growth was a surface that contained graphene only along the edges of the patterned features with all other regions containing at most a pre-graphene buffer layer, as shown in Figure 4.1(b). Patterned graphene created using this method has been referred to as "structured epitaxial graphene".

The results of this combination top-down, bottom-up approach to graphene nanoribbons are the highest reported mobilities to date,[2] reaching up to 2,700 cm^{2}V^{-1}s^{-1}.[115] FETs made from ribbons produced in this manner appear to be completely free of quantum dots, as evidenced by the gapless behavior in the low-temperature transport measurements of ribbons no more than a few tens of nanometers wide.[116] We will demonstrate that this fabrication method can, furthermore, produce feature pitches

---

[1]For example, a 10 nm-wide nanoribbon should have a band gap of 0.1 eV.

[2]More recent data have suggested that the transport in tiny structured graphene nanoribbons is completely ballistic, for which mobility is a meaningless quantity.

competitive with advanced production methods used today.

4.2   *Fabricating large arrays of structured graphene ribbons*

Below the silicon sublimation temperature, the atoms of SiC are very mobile,[117] causing any pre-existing features in the SiC to flow rapidly. It might seem difficult, therefore, to use the structured fabrication method to create highly-ordered features. To first order, the diffusion rate R_d of an atom is an Arrhenius function of how much energy is required to break the n bonds it has formed with the surrounding crystal[3],[43] following the relation

$$R_d \propto e^{-E_a/k_B T}, \tag{4.1}$$

where E_a is the so-called activation energy, which can be expressed as

$$E_a = \sum_{i=1}^{n} E_i. \tag{4.2}$$

In the case of SiC, E_i may be E_{C-C}, E_{Si-C}, or E_{Si-Si} to distinguish between the different possible bonds and their associated bond energies. Borovikov and Zangwill argued that E_{Si-C} should be the greatest because SiC is stable (i.e., C-C and Si-Si bonds in a greater SiC lattice are more likely to be broken, reducing E_a for those configurations) and that $E_{C-C} > E_{Si-Si}$ because C-C bonds are stable as Si escapes during the sublimation process.[118][4] Using equations 4.1 and 4.2, atoms with the fewest bonds should naturally be the most mobile, making corners, like those created by the etching of SiC, the most susceptible regions of the crystal to diffusion. The result of this initial diffusion is a higher-order surface that quickly reflows out from the vertical trenches, likely forming a stable facet that has been observed in numerous prior studies on SiC chemical etching [119, 120] and on the bunching of SiC steps on

---

[3]n is typically referred to as the "coordination number".

[4]Implicit in this argument is that Si sublimation is more likely to occur when an Si atom diffuses and bonds with another Si atom.

miscut (0001) faces [121] caused by disparate diffusion rates of the differently-stacked layers in the SiC.[118, 122, 123] It is useful, therefore, to think of vertically-etched SiC trenches as a series of pre-bunched steps.

For this study, arrays of trenches running along the $\langle 11\bar{2}0 \rangle$ direction were patterned into nominally-miscut, heavily-doped 4H-SiC (0001) ($n \approx 10^{18} \text{cm}^{-2}$) at the Georgia Tech Microelectronics Research Center (MiRC). First, after the application of SurPass 3000, an adhesion promoter, to the SiC,[5] 6% hydrogen silsesquioxane (HSQ) was spun onto the SiC (0001) surface, and large arrays of lines on the order of 1-200 nm by 1-2 mm were patterned by electron beam lithography (EBL) along the $\langle 11\bar{2}0 \rangle$ direction.[6] After EBL exposure and development, the HSQ-masked SiC (0001) surface was etched in a conventional RIE system (Plasma-Therm RIE) . The remaining HSQ was removed with buffered oxide etch (BOE). In this case, the actual graphitization process serves as the HSQ "descum" process because HSQ is SiO_2-based, and so any HSQ residue remaining after the BOE dip should sublimate away. Later, a 1:1 mix of ZEP520a, a polymer-based positive electron beam resist, and anisole was substituted for HSQ to decrease the exposure time by an order of magnitude without any apparent loss in cleanliness.

The samples were grown using the CCS method [see Figure 4.1(a)] out of the (0001) surface. For shallow trenches on the order of 20 nm or more, no explicit step-flow time was used, ramping instead directly to the graphitization temperature of 1,550 °C for 1-5 minutes. Figure 4.2 shows an example of the resulting highly-ordered arrays. In addition to AFM, electrostatic force microscopy (EFM), which applies a bias between the AFM tip and the sample to add a tip deflection component caused by the free charge of the region beneath the tip, is used in Figure 4.2(b) to confirm

---

[5]This step was found to be necessary, as the patterned features appeared to "run" without the promoter.

[6]It is worth noting that, without a lengthy post-anneal, using HSQ to pattern graphene directly results in significant defect formation as a result of electron-beam-induced hydrogenation and rehybridization of the graphene surface, as shown conclusively by Ryu, et al.[124]
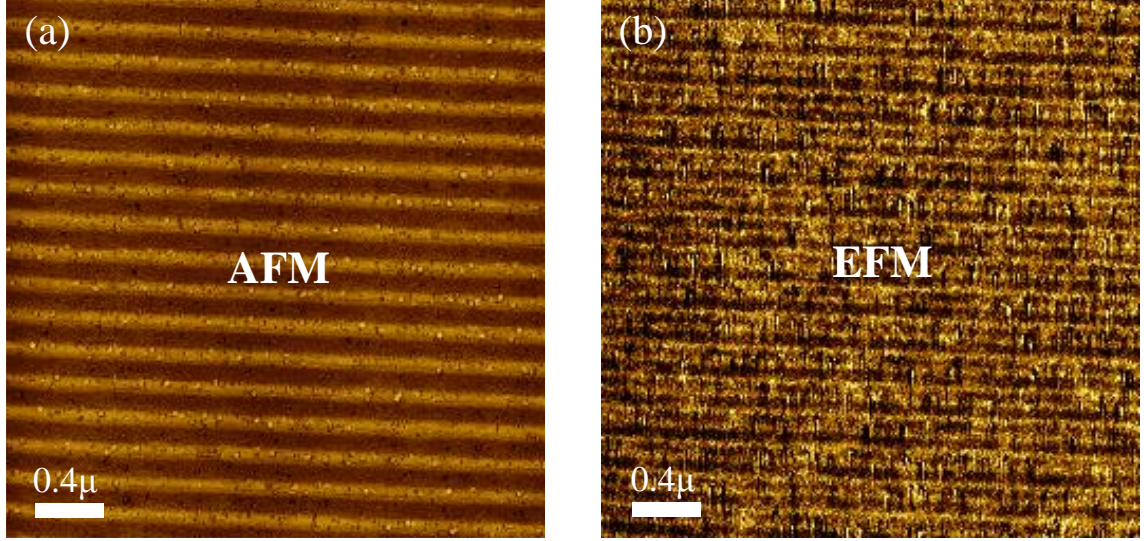
Figure 4.2: AFM and EFM of a large array of sidewall nanoribbons. (a) AFM image of a large sidewall array, with lighter colors indicating higher topography. (b) Corresponding EFM image, with the bright areas being graphene and the darker areas being SiC. The trenches are about 20 nm deep.

that the graphene is mostly confined to the sidewalls. The structured graphene has an excellent contrast with the $6\sqrt{3} \times 6\sqrt{3}R30°$ buffer layer on the (0001) surface in EFM because the latter, as a semiconductor, does not have a significant free carrier concentration.[125] As an aside, it should be noted that the apparent width of the graphene regions in EFM is a convolution of the tip radius (10 nm) with the actual graphene region width, and so any apparent width seen in EFM should be reduced by about that amount to get the true width.

Dense arrays of sidewall ribbons similar to those in Figure 4.2 were also measured by LEED, as shown in Figure 4.3(a). The patterns have many of the salient features of a typical Si-face graphene sample (see Figure 1.5) but with the addition of vertical streaks, most visible in the red dashed region, attributed to a combination of specular and diffraction spots of the sidewall facet. The center of the streaked area does not move with changing electron energy, suggesting it is the result of specular reflection. The surrounding spots were observed to move slightly with energy, suggesting they
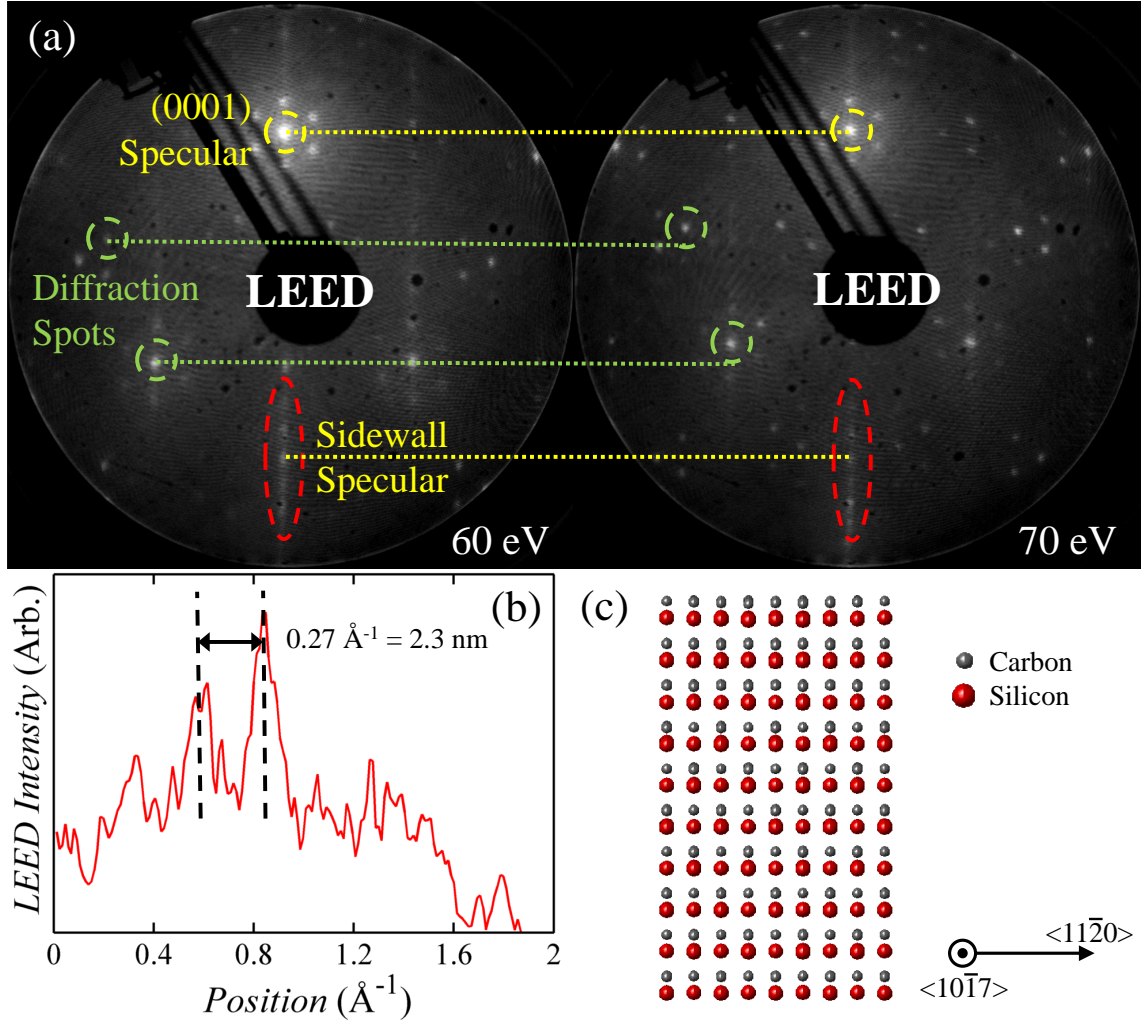
Figure 4.3: Explanation of the LEED pattern from a dense array of sidewall nanoribbons. The ribbons are oriented in approximately the same way as in Figure 4.2, and the sample is tilted so that the (0001) specular spot lies near the top of the image, rather than in the center, where it would normally be blocked by the electron gun. (a) LEED taken at 60 eV and 70 eV, clearly distinguishing between spots with diffractive and specular origins. (b) Integrated intensity profile along the vertical direction in the "Sidewall Specular" region from (a) plotted in terms of $Å^{-1}$. (c) Illustration of the $(10\bar{1}7)$ surface from the perspective of its normal.

are diffraction spots.[7] The difference between specular and diffraction spots can be clearly seen by observing which spots do and do not move going from 60 to 70 eV in Figure 4.3(a).

An intensity profile along the vertical streak, shown in Figure 4.3(b), reveals that there are a series of intensity peaks spaced about 0.27 Å^{-1} apart within the streak, corresponding to a real space periodicity of about 2.3 nm. This extra periodicity comes from the underlying sidewall crystal facet, which at a 29° tilt corresponds to the (10$\bar{1}$7) surface and has a rectangular, rather than hexagonal, symmetry, as seen in both our LEED data as well as a sketch of the facet, given in Figure 4.3(c).[8]

4.3   Factors affecting sidewall order

To elucidate some of the factors that affect sidewall order, we use nominally < 10 nm deep trenches, as shallow features should be especially sensitive to step flow. Based on the simple picture of sidewall growth painted in the previous sections, the SiC step flow rate should purely be a function of temperature, while the graphitization rate should be a function of temperature and ambient silicon pressure. While the latter is true, we find that the growth process is much more complicated, and that step order can be controlled in a number of ways, including increasing the growth temperature, adding a high temperature anneal step, growing on the C-face, and roughening up the surface. The unifying mechanism, if any, behind these strategies is unknown at this point.

Figure 4.4 shows, surprisingly, growing at a higher temperature actually *increased* the order of our sidewall pattern. The Raman spectrum in Figure 4.4(d) confirms

---

[7]Diffraction spots move because as the electron energy becomes larger (smaller), the relative momentum imparted by in-plane diffraction becomes smaller (larger) relative to the total momentum of the electron, making the angle at which the electron exits the material correspondingly smaller (larger). A reflected electron contributing to a specular spot experiences no in-plane momentum transfer, and so its trajectory does not change with energy.

[8]See Appendix B for a detailed calculation of various SiC facet angles relative to the {0001} surfaces.
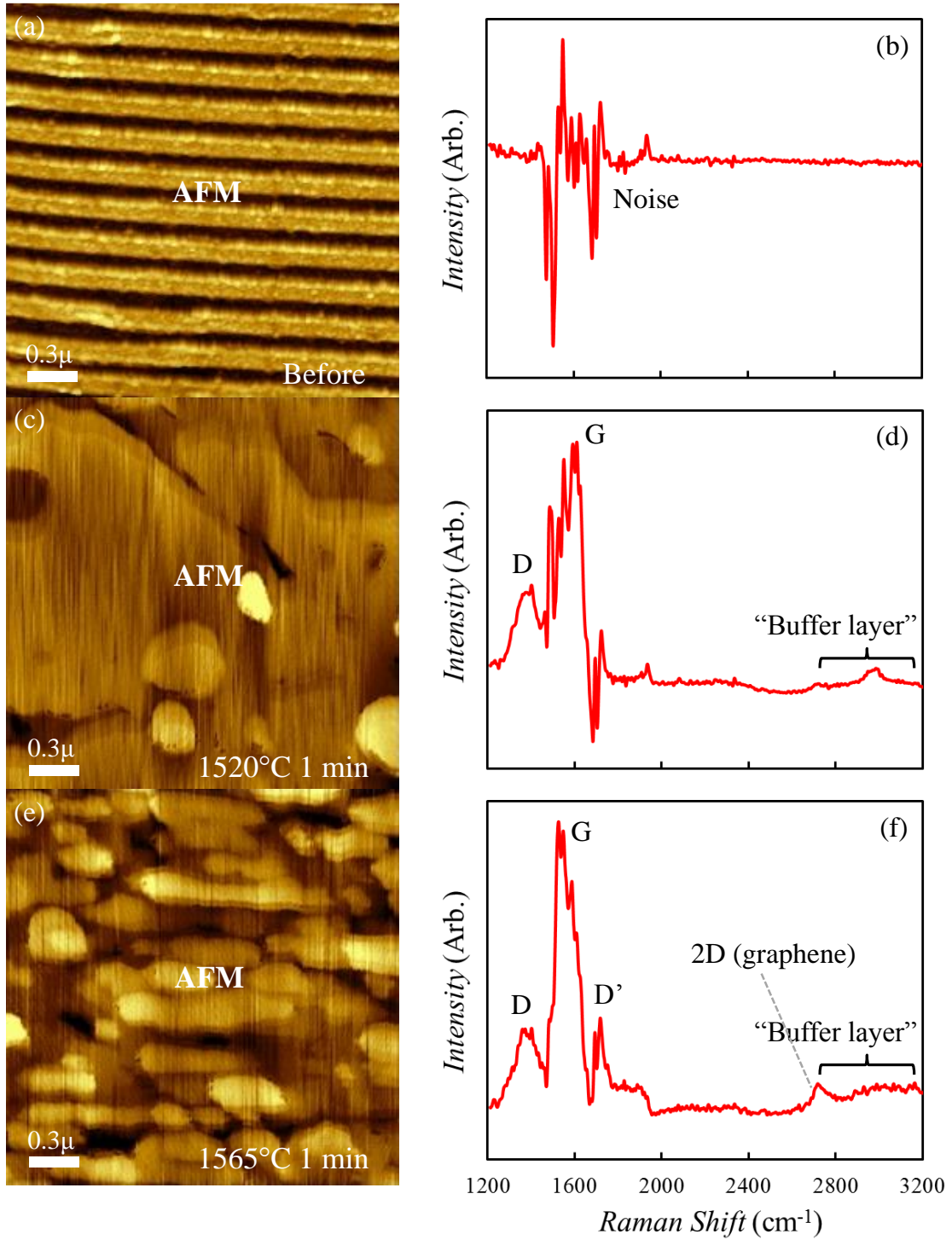
Figure 4.4: Effect of growth temperature on sidewall order. AFM of a dense sidewall pattern before (a) and after heating to 1,520 °C (c) and 1,565 °C (e) for 1 minute. (b), (d), and (f) show the corresponding background-subtracted Raman spectra for (a), (c), and (e), respectively.
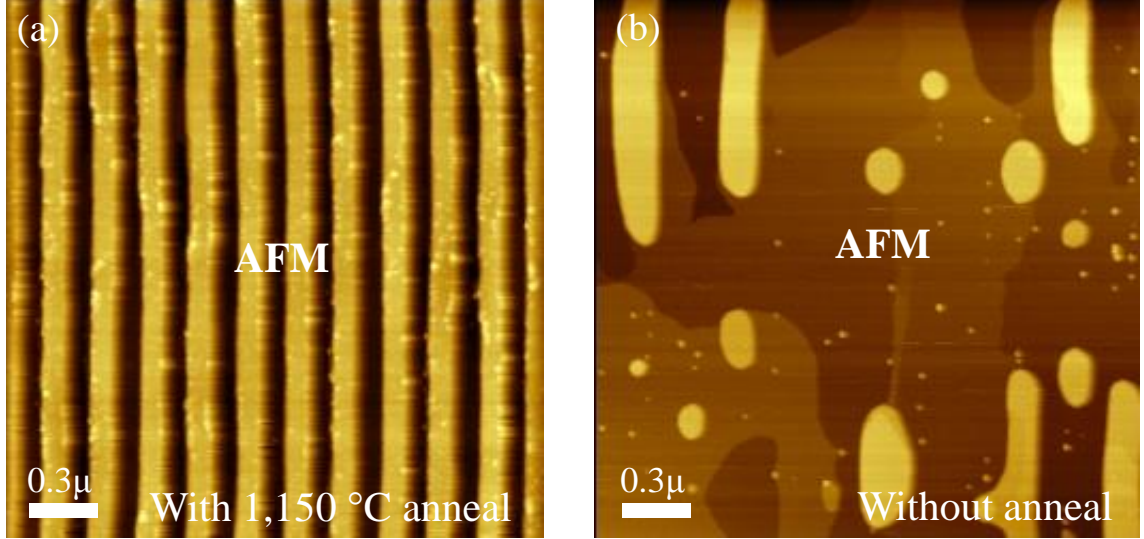
Figure 4.5: Effect of 1,150 °C anneal on sidewall order. AFM of dense sidewall patterns with (a) and without (b) a 30-minute anneal at 1,150 °C before proceeding with growth at 1,520 °C.

that only a buffer layer, indicated by broad peaks around 1,350 cm^{-1}, 1,600 cm^{-1} and 3,000 cm^{-1}, has formed. This last peak is previously unreported on graphene, but the entire Raman spectrum is similar to what has been called "nanocrystalline graphite", which are small domains of graphite.[98] When heated up to 1,565 °C for the same amount of time, the buffer layer forms more quickly over the (0001) surface, and the patterned features retain much more of their original shape. A sharp 2D peak around 2,750 cm^{-1}, presumably arising from the sidewall graphene, is also visible in (f).

In Figure 4.4(f), the 2D peak position is higher than the nominal 2,700 cm^{-1} cited in the literature for ideal graphene.[36] The position of this peak is dependent on doping,[126] whether it is part of a multilayer stack,[127] and strain,[128, 129] among other things. For example, a combination of compressive strain and doping on the Si-face causes the 2D peak position of a monolayer to shift above 2,720 cm^{-1}.[130] In the absence of doping (to be shown later in this Chapter), the ribbons are likely also under significant compressive strain — perhaps even moreso than on the Si-face.

The effect of growth temperature pales in comparison to the effect of a high
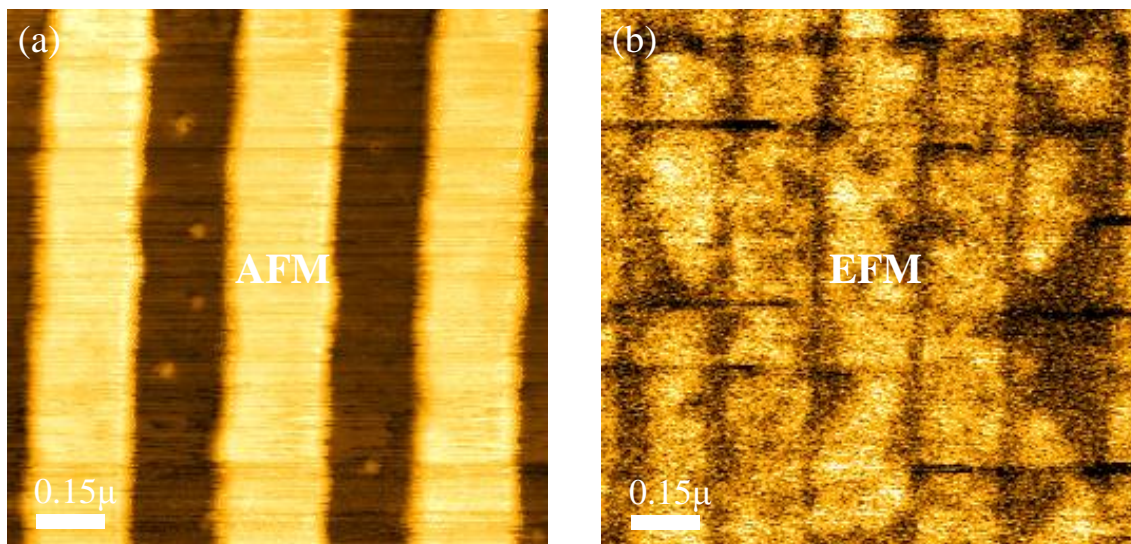
Figure 4.6: Sidewall growth on the C-face at 1,500 °C. (a) AFM and (b) EFM images after growth. The darker areas of (b), confined mostly to the sidewall regions seen in (a), are devoid of graphene, while the rest of the surface appears to have at least a monolayer of graphene.

temperature anneal, as seen in Figure 4.5. In this case, a 30 minute anneal at 1,150 °C was done *in situ* prior to growth at 1,520 °C. The difference in surface order is obvious in Figure 4.5(a), with the trenches retaining essentially all of their shape, whereas they largely melted away without the anneal, shown in Figure 4.5(b). The mechanism behind the efficacy of the extra step is a mystery, at the moment, because a LEED measurement of a similar sample after annealing but before growth found only unreconstructed SiC 1×1 diffraction spots, indistinguishable from a clean (0001) surface. Further analysis by XPS revealed that no C–C bonds exist and, interestingly, that surface lacked the native oxide that is typically observed on the Si face.[131]

Two other effects, perhaps not applicable to the immediate problem of improving sidewall order on trenches patterned into the Si-face, were also seen. The first is shown in Fig 4.6, which contains AFM and EFM scans of a sidewall sample grown at 1,500 °C for 1 minute on the C-face instead of the Si-face. Being on the C-face, graphene formed quickly over the flat, non-sidewall surface, but no sidewall graphene was found on this sample either through EFM or ARPES. In this instance, the quick
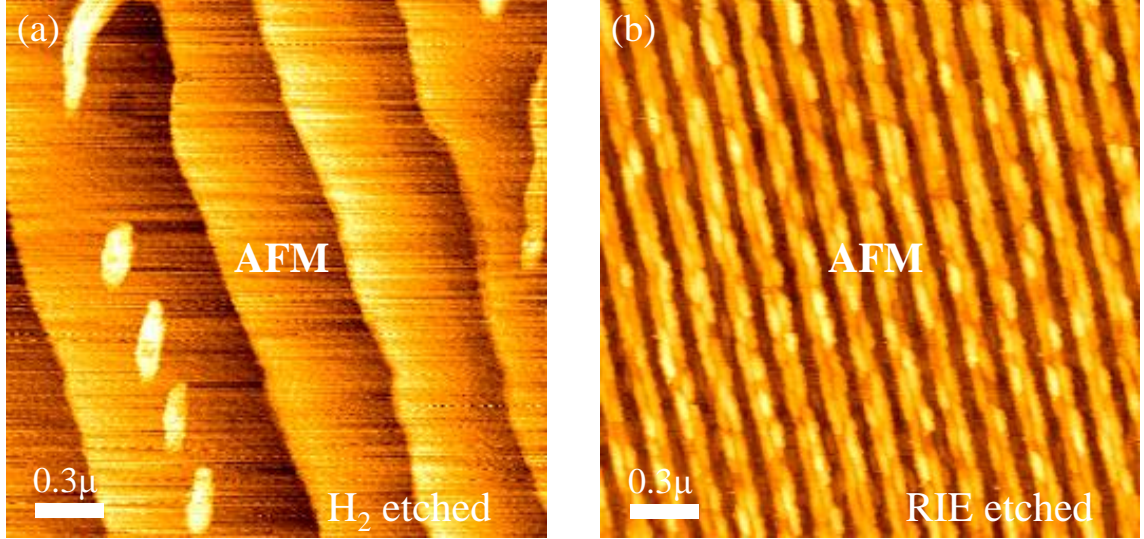
Figure 4.7: Effect of starting substrate roughness on sidewall order. AFM of a dense sidewall pattern starting with H_2- (a) and RIE-etched (b) SiC (0001) surfaces shows that the macroscopic order of the trenches is much higher at the same growth conditions with a rougher starting surface.

growth of graphene may have acted as a SiC diffusion barrier, preserving trenches that had completely run together at a similar temperature of 1,520 °C on the Si-face.

The second effect was that of starting surface roughness on sidewall stability. Figure 4.7 shows the result of graphitizing a sidewall pattern using two extremes for starting surface roughness: H_2-etched[9] and RIE-etched using a SiC etching recipe. While the H_2-etched surface is as flat as possible given the inevitable miscut in the wafer when being diced, the RIE-etched surface contains domains on the order of 100 nm in size with a roughness of 2-3 nm. From these starting surfaces, the sidewall pattern was etched into the SiC as done previously. The RIE-etched surface proves to make step flow much more difficult, as the initial pattern made in the SiC remains completely intact after going through a typical sidewall growth cycle. By contrast, the features made into the H_2-etched surface are almost completely gone with only a few isolated mesas existing far away from atomic step edges. The exact cause

---

[9]H_2 etching involves heating the SiC to around 1,400 °C in a dilute hydrogen gas flow for around an hour. The resulting surface contains highly-ordered, atomically-flat steps.[120]
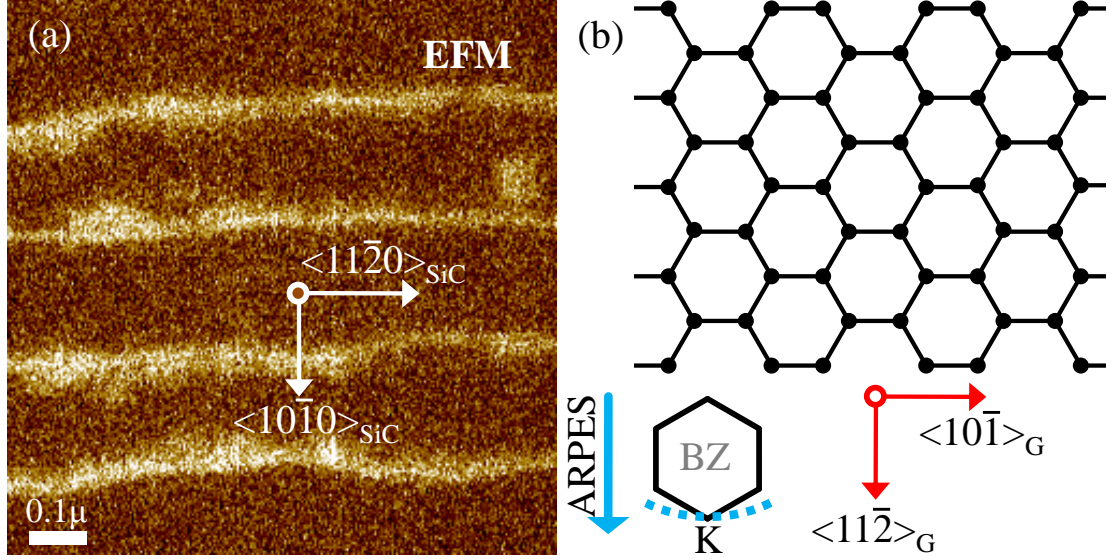
Figure 4.8: Orienting depiction of the ARPES setup used for investigating sidewall nanoribbon arrays. (a) EFM image of the 10 nm sidewall ribbon array. (b) Schematic of the expected lattice of the nanoribbons, paying special attention to the "armchair" edge shape on the top and bottom. The in-plane projection of the $\phi = 0$ direction of the ARPES detector is in the $\langle 10\bar{1}0 \rangle_{SiC}$ direction.

for the roughness-induced feature stability was not investigated further because the RIE-etched sample in Figure 4.7(b) was found in EFM, not shown, to contain not sidewall graphene ribbons but rather a number of small graphene islands. Possible explanations, however, include step pinning from defects introduced by the etching formula or, perhaps more simply, the fact that rougher surfaces require more energy (or time) to smooth out.

4.4 ARPES on arrays of structured graphene ribbons

To test theoretical predictions made about graphene nanoribbons, arrays of sidewall ribbons 10 nm and 30 nm in width were fabricated and characterized by ARPES. The sidewall growth method, combined with the excellent depth precision of RIE, allows for the easy fabrication of ribbons that are on the edge of possibility using a strictly top-down approach to patterning a single sheet of graphene. As shown in Figure 4.8, the ribbons, grown lengthwise along the $\langle 11\bar{2}0 \rangle_{SiC}$ direction, have edges
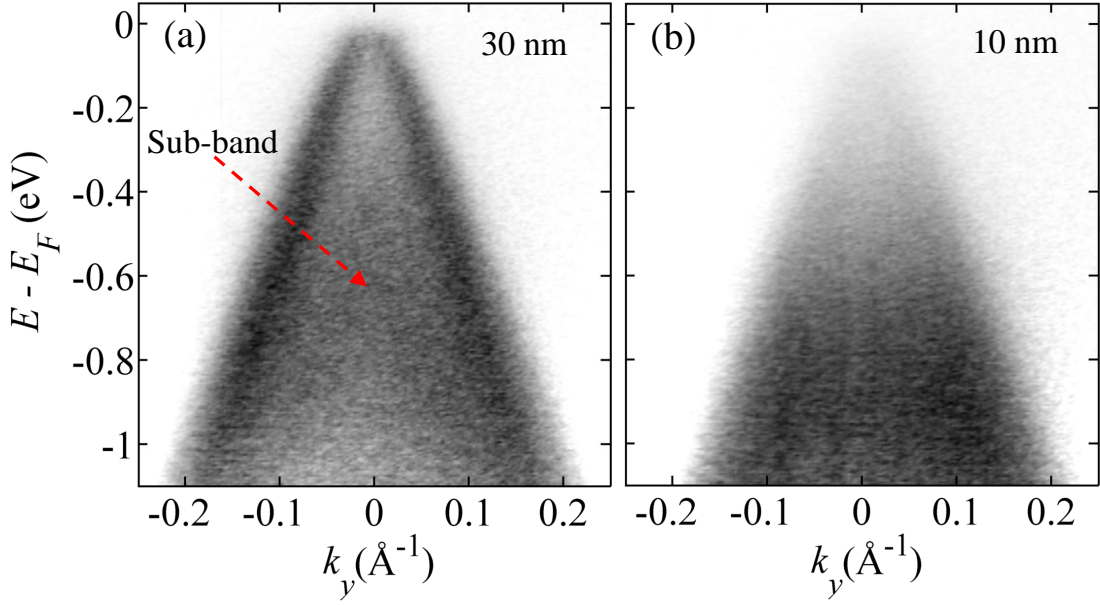
Figure 4.9: Bands as seen by ARPES near the K point of 10 and 30 nm sidewall ribbon arrays. (a) 30 nm array, depicting a Dirac cone with what appears to be a diffuse subband, reminiscent of bilayer graphene on the Si-face. (b) 10 nm array, where there are no distinct bands and the intensity fades rapidly toward the Fermi level. The data were taken at 100 K.

roughly along the so-called "armchair", or $\langle 10\bar{1} \rangle_G$ direction. This edge direction in particular has been identified as potentially possessing the largest band gap for a given ribbon width,[112, 111] and it is also known to endow carbon nanotubes extending along this direction with semiconducting properties.[113].[10]

Figure 4.9 depicts the ARPES bands from sidewall ribbon arrays composed of 10- and 30 nm-wide ribbons. Confirming the highly-ordered nature of the sidewall ribbon arrays, the 30 nm ribbons in Figure 4.9(a) feature a prominent Dirac cone. The ribbons in both arrays were found to be rotated about the $\langle 11\bar{2}0 \rangle_{SiC}$ direction by about $\theta = \pm 29°$ relative to the SiC (0001) surface, in agreement with the previous LEED data presented on a different sample. There was significant intensity corresponding to graphene on the (0001) surface, attributable to the ribbons sometimes overgrowing

---

[10]It is important to point out a difference in nomenclature between the graphene and carbon nanotube literature; in the case of the former, "zigzag"/"armchair" refers to the shape of the *edges*, while in the case of the latter, those terms refer to the direction *perpendicular* to the edges.

the sidewall facet onto that surface. Because the cones of both arrays lie firmly on $k_y \approx 0$, the graphene on the sidewall facets appears to have more in common with Si-face graphene than that of the C-face because the latter typically exhibits a distribution of cones in ARPES.[54] Furthering this point, a diffuse graphite-like sub-band around -0.6 eV is visible in Figure 4.9(a), although the fraction of graphitic stacking must be small, as the measured Fermi velocity is around the 10^6 m/s seen in single layer graphene and MEG [1] rather than the 8×10^5 m/s seen in graphite. Also of note is the fact that the cones, although presumably belonging to mostly single-layer graphene, is essentially undoped, in contrast to single layer graphene on the (0001) face.[53, 132] The reason for this lack of doping is currently unclear, but there are likely differences between the higher order sidewall facet and the (0001) face that could contribute to a differing amount of charge transfer to the graphene, including a work function difference and a possible lack of a buffer layer on the sidewall.

The linewidths of the bands in Figure 4.9(a) are significantly thicker than those in a bulk graphene ARPES image.[1] It is tempting to use this information alone as evidence that the image contains very thin nanoribbons because narrow features in real space produce broad ones in reciprocal space, and so these ribbons might therefore be thin enough that their bands are broader than the angular resolution of the ARPES detector. For a 30 nm ribbon, however, the broadening is expected to be only about $\frac{2\pi}{300\text{Å}} \approx 0.02\text{Å}^{-1}$ — much smaller than the broadening observed here. Furthermore, the k_y direction is along the length of the ribbons, and so broadening would not be expected along k_y as there is no confinement in that direction. We conclude that the bands, at least in the case of Figure 4.9(a), are instead being smeared by disorder in the orientation of the ribbons.

ARPES bands from the 10 nm ribbon arrays in Figure 4.9(b) differ greatly from those of Figure 4.9(a). Notably, the photoemission intensity drops precipitously toward E_F. Additionally, distinct bands are barely visible against what appears to be

56

an opaque triangle of intensity, although further down in energy (not shown) discrete bands were observed. This opaqueness is likely caused by both physical disorder in the ribbons and from splitting in the nanoribbon bands caused by the extremely small lateral ribbon dimensions. Still, it is impossible to tell from these data alone whether each area along the nanoribbons contains at least one metallic electron following the Dirac cone or whether some areas have Dirac electrons and others do not. However, we note that transport experiments on high-mobility sidewall ribbons [116] and unzipped nanotubes [109] have so far failed to report significant band gaps.

Finally, although we have presented data here only on sidewall graphene oriented roughly in the $\langle 10\bar{1} \rangle_G$ direction, or armchair direction, unsuccessful attempts were also made to image the bands of ribbons running along $\langle 11\bar{2} \rangle_G$, or zigzag direction. We believe the reason for this discrepancy is a lack of a single favorable SiC facet in that direction, causing intensity from the Dirac cone from graphene on these facets to be spread around in reciprocal space. The existing literature supports our claim; first, all works to date that image sidewall graphene by TEM use the SiC $(10\bar{1}n)$ facets,[115, 133] and, second, past work on SiC has shown that the orientation of 4H-SiC (0001) steps after hydrogen etching, a process quite similar to graphene growth, favor the $\langle 10\bar{1}0 \rangle_{SiC}$ direction.[120] It is imperative to understand, however, that this facet disorder does not *necessarily* translate into reduced graphene quality.

CHAPTER V

GFET FABRICATION PROCESS USING BENT GRAPHENE

Although FETs operating at over 300 GHz using graphene have now been claimed,[134, 135] these numbers come with the caveat that they represent f_T, the frequency at which the current gain h_{21} is unity. This figure of merit is not relevant for digital electronics, which require a voltage gain $h_{12} \geq 1$, because logical values are represented by voltages that must be preserved and carried forward through many computations. Unity voltage gain frequency has, until recently, remained unreported because the low output resistance of graphene essentially guarantees that this quantity is less than the unity current gain frequency.

Until now, greater than unity voltage gains in graphene FETs (GFETs) have been obtained solely by employing a very thin ($\leq$ 5 nm) gate dielectric to maximize the controlling electric field.[135, 136, 137] In this Chapter, we propose a GFET fabrication process that exploits a heretofore undiscovered curvature-induced semiconducting region of graphene draped over two adjoined SiC facets [5] to create an on/off ratio larger than that of an ideal graphene sheet in a similar device. First, details of this semiconducting region are given, followed by an overview of our proposed GFET fabrication process. Finally, we give electrical data that appear to confirm that our semiconducting junction may have superior voltage gain characteristics through higher off-state resistances and a non-linear current-voltage characteristics.
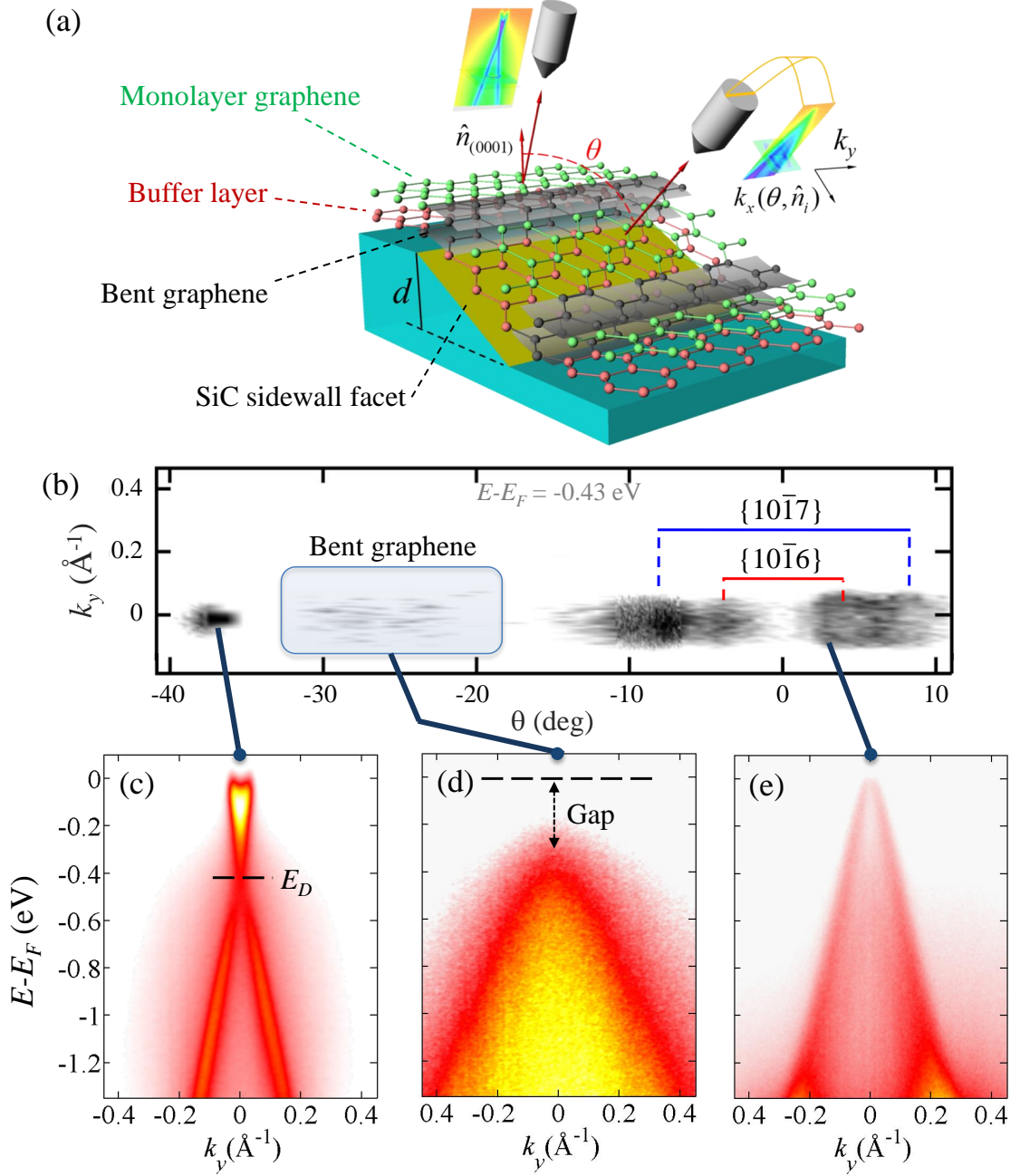
Figure 5.1: ARPES of an overgrown sidewall array with a semiconducting bent graphene region. (a) ARPES experimental setup, illustrating the effect of varying θ. (b) 2D constant energy cut at $E - E_F \approx -0.43$ eV over a variety of detector angles θ, detecting Dirac cones coming from surfaces ranging from (0001) to $\{10\bar{1}6\}$. (c-e) ARPES bands deriving from graphene on the (c) (0001) surface, (d) semiconducting transition region, and (e) $\{10\bar{1}6\}/\{10\bar{1}7\}$ facets. Adapted from Reference [5].

5.1 A semiconducting graphene region at the junction of two SiC facets

In the previous Chapter, we presented ARPES data on structured epitaxial graphene grown on higher order surfaces of SiC. Samples that were overgrown in the sense that the graphene grew over the sidewalls and onto the flat (0001) surface were also investigated. A 2D constant energy cut, as well as representative experimental bands, of a typical overgrown sidewall sample are given in Figure 5.1.

In Figure 5.1(b), which is a 2D constant energy cut at an energy corresponding to E_D for monolayer graphene on the (0001) surface, many Dirac cones are visible, corresponding to at least three different SiC facets: (0001), $\{10\bar{1}7\}$ ($\Delta\theta \approx 28.6°$), and $\{10\bar{1}6\}$ ($\Delta\theta \approx 32.2°$). Other facets, including $(10\bar{1}8)$ ($\Delta\theta \approx 25.3°$) have been reported in the literature.[115] We observed no difference in doping between graphene on the $\{10\bar{1}6\}$ and $\{10\bar{1}7\}$ surfaces. A faint region of intensity is visible in Figure 5.1(b) centered around $\theta \approx 27°$. After significant background subtraction, plotting E vs k in this region reveals a cone whose apex lies around 0.5 eV below the Fermi level, with no intensity above the apex, suggesting that a band gap exists. Because of its faint intensity as well as its orientation relative to the (0001) and $\{10\bar{1}7\}$ surfaces, we propose that this cone is derived, as shown in Figure 5.1(a), from a bent transition region between the sidewall facet and the (0001) surface.

Consistent with being derived from a very narrow bend in the graphene, our ARPES data give evidence for the quasi-one-dimensional (1D) nature of the semiconducting region, similar to the case of a carbon nanotube. First, as shown in Figure 5.2(a), the shapes of intensity profiles, called energy distribution curves (EDCs), through $k_y = 0$ at several θ are nearly indentical, indicating that the band structure of the region does not depend on θ. However, observing that the *relative* intensities of the EDCs do change with θ, as shown in Figure 5.2(b) allows us to estimate the width of the semiconducting region. We treat the photoemission intensity $I(\mathbf{k})$ originating
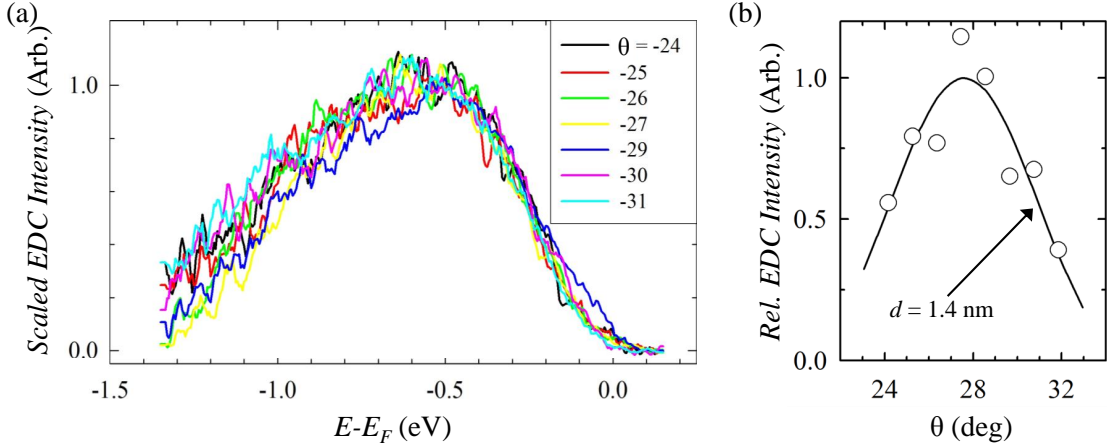
Figure 5.2: Quasi-1D nature of bent graphene on SiC. (a) Multiple scaled EDCs at various angles θ using the same dataset as Figure 5.1. (b) Relative EDC intensities of the data in (a) with a fit to $\text{sinc}^2\left(\frac{\pi d \sin\theta}{\lambda}\right)$ for $d = 1.4$ nm. Adapted from Reference [5].

from this area as being emitted from an infinitely long source of width d in $\hat{\mathbf{x}}$, which will convolve the emitted intensity pattern of an infinitely wide source $I_0(\mathbf{k})$ with the function $\text{sinc}^2\left(\frac{k_x d}{2}\right)$ to give

$$I(\mathbf{k}) = I_0(\mathbf{k}) * \text{sinc}^2\left(\frac{k_x d}{2}\right) = I_0(\mathbf{k}) * \text{sinc}^2\left(\frac{\pi d \sin\theta}{\lambda}\right) \tag{5.1}$$

where $\lambda \approx 0.22$ nm for a typical photoelectron with an energy of 30 eV. We find that the shape of the data in Figure 5.2(b) is best fit by $d = 1.4$ nm. This number is consistent with TEM studies of the radius of curvature of graphene as it runs over natural steps on SiC (0001).[133]

The final evidence for the semiconducting region deriving from bent graphene lies in its reduced Fermi velocity of only about 5×10^5 m/s. From Equation 1.2, $v_F = \frac{\sqrt{3}at}{2\hbar}$. $\hbar$ is a universal constant, and a decrease in the lattice constant a to completely account for the decrease in v_F implies physically unreal C–C bond lengths of < 1 Å.[138] The majority of the reduction, therefore, must come from the hopping energy t decreasing from ~3 eV to < 2 eV, which comes conceptually from curvature in graphene through p_z-p_z orbital interactions as well as rehybridization with sp^2

bonds.[139, 140]

The origin of the band gap in bent graphene on SiC is unclear because its geometry admits a number of explanations, including substrate bonding, strain and confinement. Currently, we have no evidence of bonding to the substrate in the bend region. Calculations of curvature-induced strain on carbon nanotubes estimate the strain-induced band gap from a curvature radius of ~1 nm to be on the order of tens of meV,[139] while similar calculations of unaxial strain on graphene also predict that enormous (~10%) strain values are required to get modest (~100 meV) gaps.[141] By contrast, from confinement alone, the expected gap would be around 1 eV-nm / 1.4 nm $\approx$ 0.7 eV.[111] Confinement, therefore, appears to give the most compelling reason for the formation of the band gap.

In retrospect, there is some evidence in the literature for our semiconducting structure forming when graphene runs over natural atomic steps on SiC (0001). Macroscale electronic transport measurements on epitaxial graphene by Yakes, et al., found that four point measurements with current injection across natural steps in SiC were a factor of 2 higher than those along the steps.[142] Mesoscale scanning tunneling potentiometry measurements near the atomic level made by Ji, et al., found large potential drops localized to SiC steps.[143] We expect that the resistance across bends in our structured graphene to be larger than that of natural SiC — a result that predicted theoretically by Tow, et al. [144] — because the radii of curvature for graphene running over higher SiC steps are smaller.

5.2   The basic GFET

The GFET, shown in Figure 5.3 is similar to the silicon FET in many ways, minus the details of how particular components, in particular the source and drain, are achieved. In silicon devices, when the gate of an FET is defined, highly-doped source and drain regions are automatically placed in proximity to it through the use of
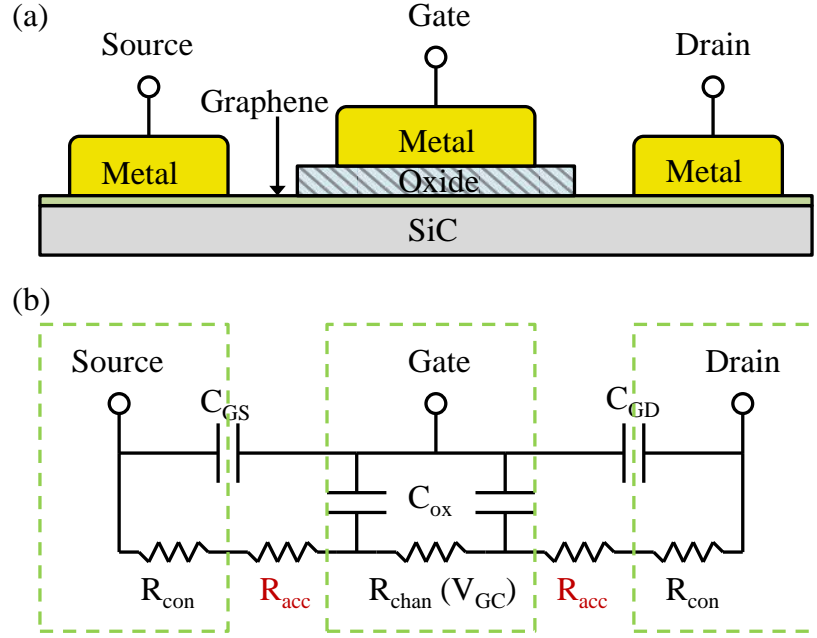
Figure 5.3: GFET schematic and equivalent resistor/capacitor model. (a) Schematic of a basic GFET. The gate oxide does not share the same dimensions as the gate because it is typically part of a separate fabrication step. (b) Equivalent resistor/capacitor model of the GFET, showing the variable channel resistance $R_{chan}(V_{GC})$ that is dependent upon the gate-to-channel voltage, electrode contact resistance R_{con}, gate capacitance C_{ox}, and gate-source/drain capacitances C_{GS} and C_{GD}. The undesirable access resistance is R_{acc}.

ion implantation and subsequent annealing to drive the dopants a little underneath the gate.[43] By contrast, the archetypal GFET currently does not use highly-doped wells because of the inability to repair the substantial lattice damage caused by ion implanation, which can reach many nm into the substrate.[43] As a result, as shown in Figure 5.3(a), the graphene between the gate and the source/drain electrodes is both ungated and potentially undoped, resulting in relatively large resistances that hinder the performance of the GFET. This parasitic resistance has been referred to in the graphene literature as the *access resistance*.[95, 32]

The GFET presented here is similar to the archetypal GFET given in Figure 5.3 save for two differences: the channel is composed of an array of overgrown and inter-connected structured graphene, and the gate oxide is formed passively at the interface of the graphene and the gate. The former difference allows us to use large gate lengths to take advantage of the ease of aligning to larger features yet maintaining a large fractional coverage of semiconducting bent graphene, while the latter allows us to eas-ily create a thin gate dielectric. These two design choices should increase the voltage gain of our proposed GFETs.

Figure 5.4 shows the basic GFET fabrication process proposed here to create a CMOS-style inverter containing two transistors — one n- and one p-type — placed so that their channels are in series with respect to the source/drain electrodes. The inverting output is an electrode attached to the common end of the two transistors. Notably, since GFETs can take on both n- and p-type characteristics, GFETs can be used as both types of transistor.[136, 137] In this sense, the designs of GFET devices are simpler than comparable CMOS ones.

Following this process, we start with bare SiC (0001) that has been planarized with a chemical-mechanical polish (CMP) by the manufacturer (Cree, Inc.) and etch trenches 20 nm deep into it. In reality, this channel contains several trenches in parallel so that extremely small gates are not required. Monolayer graphene is
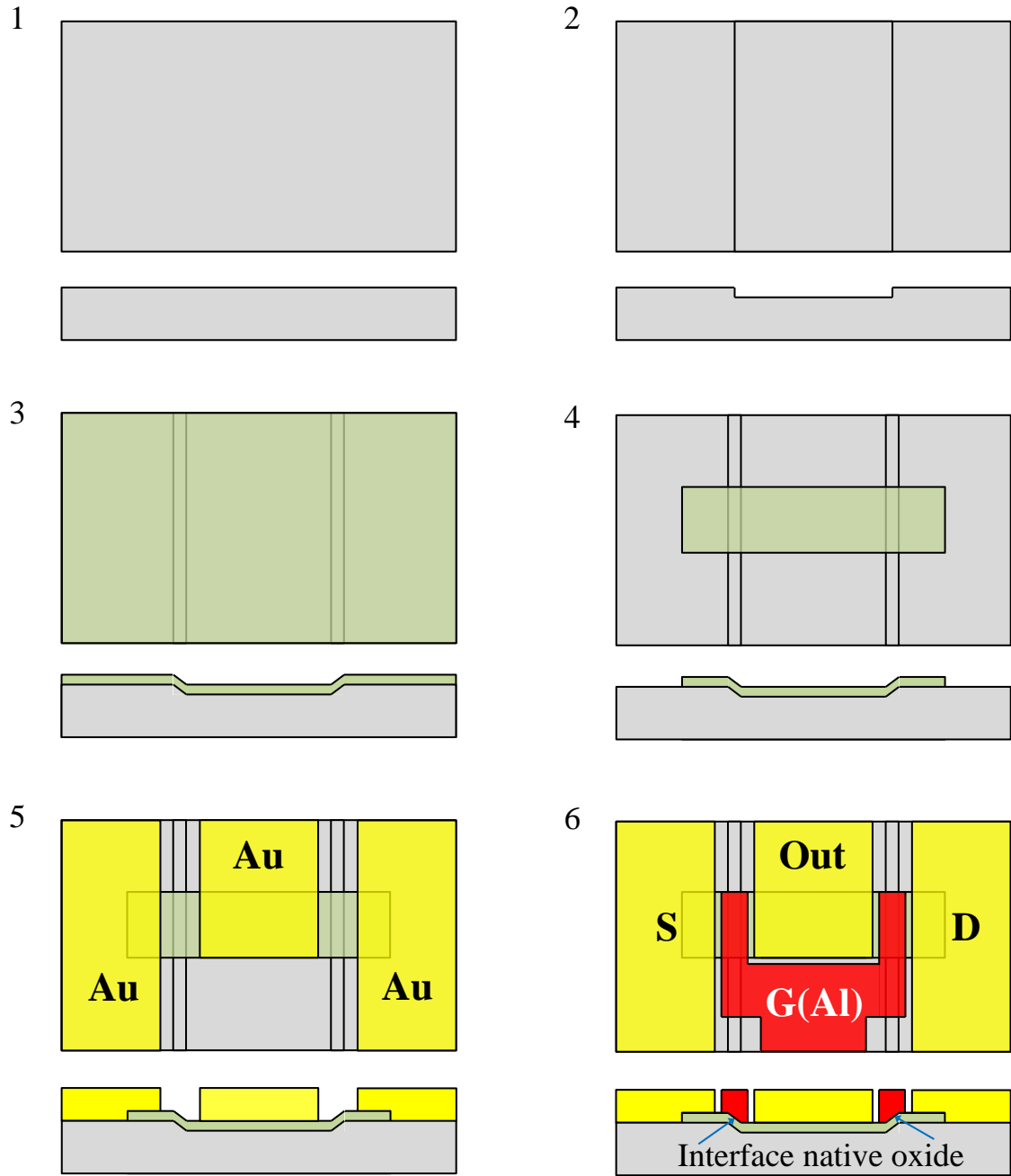
Figure 5.4: GFET inverter fabrication process.

grown over the entire sample by heating to about 1,550 °C for 15 min using the CCS process. The graphene channel ($L \approx 1.5~\mu$m, $W = 5~\mu$m) is then defined by EBL and a subsequent RIE etch.

For direct contacts to the graphene (e.g., for the source/drain electrodes) 10/50 nm layers of Cr and Au are evaporated onto the surface and defined by a liftoff process using polymethyl methacrylate (PMMA) e-beam resist. For the gate stack, 50 nm of Al is evaporated onto the surface and defined by the same liftoff process used for the source/drain. As mentioned previously, an extremely thin layer of alumina (Al_2O_3) forms in ambient conditions between the graphene and aluminum.[136, 137, 145] Low-humidity air, such as that found in a cleanroom, was found to be sufficient to form a high-quality oxide.

5.2.1 A native oxide gate dielectric

Depositing a uniform, thin gate dielectric on graphene is a difficult challenge because sputtering and atomic layer deposition (ALD), two common techniques used in industry, are not completely compatible with graphene. In the case of sputtering, the substrate is bombarded with atomic species of sufficient energy to cause surface lattice damage[1] that could severely affect the conductivity of the atomically-thin graphene.[43] For ALD, the mostly chemically-inert nature of graphene means that adhesion, and therefore uniformity, is poor without introducing special processing steps,[147] such as plasma pre-treatments to enhance the chemical reactivity of the surface,[148] or depositing special "seed" layers to provide an alternative, more reactive surface.[149, 150] These layers inevitably reduce the effectiveness of the gate by increasing the separation between it and the graphene channel. Other, more exotic approaches of creating gate dielectrics have been demonstrated, such as ion gels [151] and hexagonal boron nitride (h-BN) flakes [152], but these methods are currently

---

[1]Despite this, sputtering has been successfully used recently to deposit ~1 nm thick aluminum oxide tunnel barriers on graphene for studying spin lifetimes in the latter material.[146]

firmly rooted in the realm of research.

Although it is not clear the precise mechanism behind its formation, multiple groups have demonstrated working GFETs, including the first single [136] and multi-stage [137] logic inverters, using an oxide passively formed at the interface between evaporated Al and graphene as the gate dielectric. Malec, et al., showed that the Al leads on graphene of width 1 μm served as excellent semi-insulating tunnel junctions, while a wider one of width 5 μm was conducting, suggesting the oxide is created by lateral diffusion of oxygen along the graphene from an air-exposed region.[145] Regardless, this oxide is observed to form in this work as well, demonstrated by the Al $2p$ XPS data in Figure 5.5(a). That figure shows an XPS depth profile — data taken at regular intervals after sputtering the sample surface with an intense Ar ion beam — going all the way through a large array of Al lines several μm wide on our graphene. The topmost plot (red) shows the surface spectrum before sputtering as containing alumina (76 eV) as well as Al (73 eV), which presumably comes from several nm underneath the alumina. After the surface is sputtered away, the bulk of the Al layer is up to half oxide.[2] Finally, a layer of pure alumina is observed as the etch proceeds toward the graphene in the bottommost plot (purple).

From etch times alone, the thickness of the alumina layer at the graphene-aluminum interface is not significantly different from the thickness of the alumina layer at the aluminum-air surface. The thickness of this latter layer can be found by analyzing the relative integrated intensities of the Al $2p$ XPS peaks of the aluminum and alumina both at the surface and in the bulk. Relative to the surface, the intensity of detected photoelectrons from a depth x in a film goes as $I(x) \propto e^{-x/L\cos\theta}$, where L is the energy-dependent mean electron escape depth and θ is the angle from the surface normal at which the detected electrons were ejected. The integrated intensity

---

[2]The vacuum of the chamber ($\sim$1$\times$10^{-7} torr) permits a limited amount of surface oxidation during the analysis, and so this figure should be treated as an upper limit on the amount of oxygen in the Al.
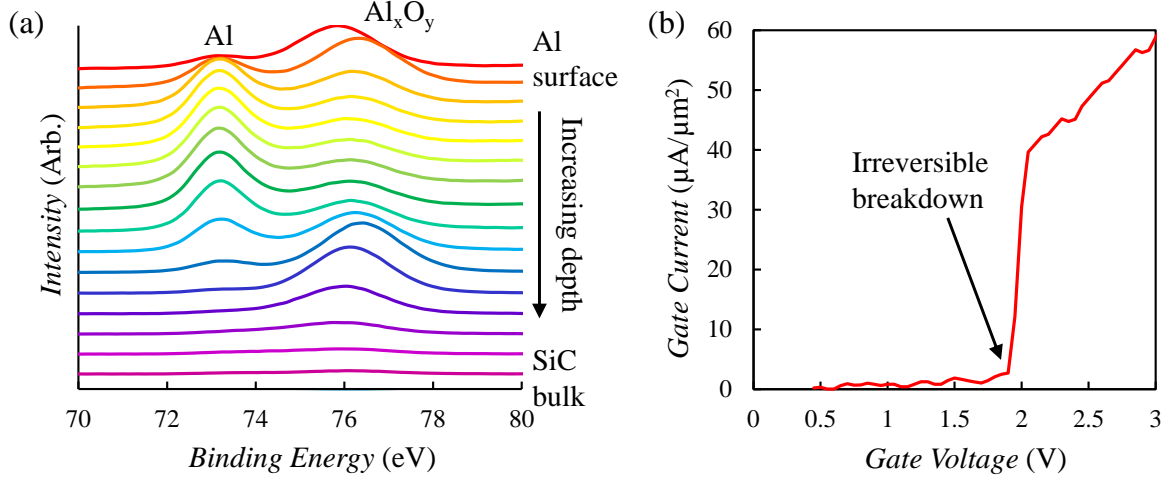
Figure 5.5: Elemental composition and breakdown I-V curve of a native oxide gate on graphene. (a) XPS Al $2p$ orbital depth profile of an array of gates several μm wide. The surface (red) shows a mix of Al and alumina, with only alumina likely being on the surface, which progresses to mostly Al in the bulk of the aluminum before turning completely to alumina again near the graphene and SiC bulk (purple). (b) Gate voltage sweep, showing a breakdown event at around 2 V (0.3-0.5 MV/cm). The biases were applied in 20 μs pulses spaced far apart to minimize heating effects that reduce the breakdown voltage.[153]

of electrons escaping from between the surface and a distance d down is therefore $\int_0^d e^{-x/L\cos\theta}\mathrm{d}x = L\cos\theta\left(1 - e^{-d/L\cos\theta}\right)$. Correcting for the atomic fraction of Al in the alumina (0.4), we can estimate the thickness using the ratios of the aluminum and alumina integrated intensities both at the surface (R_s) and in the bulk of the film (R_b) as

$$d = L\cos\theta\log\left(\frac{R_s}{R_b}\right) \tag{5.2}$$

where R_s and R_b were found to be 0.06 and 0.5, respectively, $L \approx 3$ nm for electrons with kinetic energy $1{,}486 - 75 \approx 1{,}400$ eV,[55] and $\theta = 0°$ for the XPS system used. From these parameters, the thickness of the alumina layer at the graphene is determined to be between 4 and 6 nm, depending on the true values of the mean electron escape depth and the stoichiometry of the alumina, which may deviate from the ideal Al_2O_3.

Figure 2(b) shows a typical breakdown characteristic for the native oxide gate, showing that it is, indeed, an effective gate with a high breakdown field and a low leakage current.[3] For numerous gates ranging in length from 500 nm to 5 μm, the largest tested, we find that the breakdown voltage is remarkably constant at 2 V, corresponding to a breakdown field of 0.3-0.5 MV/cm, which is comparable to previously reported values of thermally-oxidized Al_2O_3 films on silicon.[154] Although 5 μm-long gates were reported to be conducting by Malec, et al.,[145] we note that that study used exfoliated graphene, which may have a lower oxygen diffusion length owing to its low quality relative to our SiC samples. We expect that at some gate length, larger than what is considered here, that the Al would begin to form a direct contact with the graphene.

5.2.2 Structured graphene channel

Numerous two-GFET inverter structures have been fabricated with and without trenches in the channel to observe electronically a bent semiconducting graphene structure created by those trenches. One such inverter, with trenches, is shown in Figure 5.6(a). Up to 10 inverters — half with and half without trenches — were fabricated on single samples with trenches lying along each of three directions: the graphene armchair ($\langle 11\bar{2}0 \rangle_{SiC}$) and zigzag ($\langle 10\bar{1}0 \rangle_{SiC}$) directions as well as another direction halfway between. Arrays of trenches were patterned in series along each channel to amplify the potential effect of any bent graphene contained therein.

The channel resistances of 48 devices on a single sample are presented in Figure 5.6(b), demonstrating clearly that there is a large difference in resistance between channels with and without trenches. The channel resistance presented here has been compensated for contact resistance as well as the inevitable resistance anisotropy

---

[3]Although the leakage appears to be around 1 MΩ-μm^2 in Figure 5.5(b), the tool used to measure breakdown current had an internal resistance of 1 MΩ and was in parallel with the gate. The actual pre-breakdown gate resistance is on the order of 1 GΩ-μm^2.
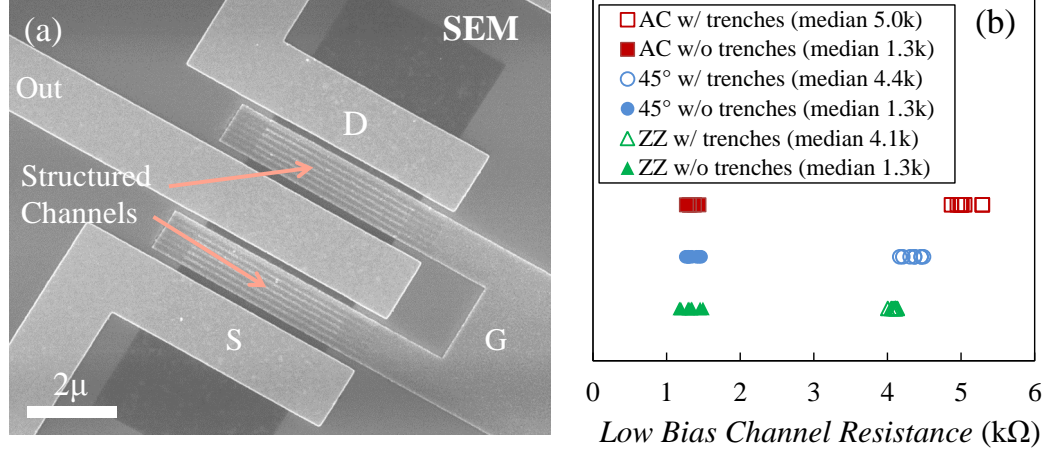
Figure 5.6: Direction dependence of structured graphene channels. (a) Scanning electron microscopy (SEM) image of a representative dual-gate GFET with a structured graphene channel, visible as lines running parallel to the longer dimension of the gate, source, and drain electrodes. (b) Channel resistance, minus contacts and natural steps,[142] of channels with structured trenches running in the graphene armchair (AC) and zigzag (ZZ) directions, as well as an intermediate direction 45° degrees from the first two.

with respect to direction as a result of natural SiC steps.[142] Contact resistances of 10^4 Ω-μm were extracted using the transmission line method (TLM), which involves fabricating a number of channels of different length and extracting the contact resistance by finding the y-intercept of a plot of resistance vs channel length.[155] Several samples, each with as many devices, have now been fabricated, and the results have been the same for each: the resistances of channels with trenches extending along the graphene armchair direction are significantly higher than those of channels with similar features fabricated along other directions. The relative increase, compared to an identical channel without trenches, is about a factor of 4 for the armchair direction, and between 2 and 3 for the zigzag direction.

These electrical data are not enough to prove that a semiconducting region exists at the bends in our structured channels; other possibilities include p-n or n-n$^+$ junctions or monolayer-bilayer transitions at the interface between the Si-face and the trench sidewalls. I-V data with temperature, as well as gate voltage sweeps, will help

distinguish between these possibilities. At the time of this writing, room temperature electrical data containing gate voltage sweeps for different trench directions has been taken, finding qualitative differences between them, but a careful analysis will follow in future publications.

CHAPTER VI

CONCLUSION AND FUTURE OUTLOOK

We have shown here that there are a number of ways that graphene on SiC can be harnessed for electronic devices. Chapter II focused heavily on graphene created from the C-face of SiC, demonstrating that even multilayer films behave as if they are weakly coupled to each other, preserving the interesting properties of an idealized, theoretical graphene sheet. This weakly-coupled nature provided us with an excellent testbed for a number of theoretical predictions about graphene, and has enabled others to produce transistors with the highest frequency power gain to date.[34] Chapter III, which further explored C-face graphene from the perspective of radiation damage, proved that electrical transport in those films are dominated by the highly-doped layers closest to the SiC. That chapter also proved that reactive oxygen species can attack graphene near room temperature, underscoring the fact that traditional photoresist cleaning methods may adversely affect graphene, despite claims to the contrary.[156]

In chapters IV and V, we presented the extension of an idea to use plasma-etched SiC structures to create so-called structured epitaxial graphene, demonstrating that feature sizes comparable to those created by advanced semiconductor processes are possible through increased SiC surface diffusion control. This understanding allowed us to collect the first ARPES band structure images of graphene lines of width < 30 nm. Chapter V presented an FET fabrication process built around a novel bent graphene nanostructure, created in overgrown structured graphene, that was suggested by ARPES to be semiconducting. Preliminary electrical measurements agreed that some special, non-ohmic behavior is induced in structured graphene, but more

study is needed to prove its semiconducting nature.

Structured graphene appears to be the future direction of graphene nanoelectronics; it solves many of the scalability issues [114] inherent to subtractively patterning features from much larger sheets. Much is unknown about the nanoscopic details of structured graphene, however, and surprises such as bent graphene will likely continue to present themselves. If bent graphene is proven electrically to behave like a semiconductor, its 1.4 nm width represents nearly the ultimate limit of scalability for semiconductor devices. The gain in off-state resistance using bent graphene is small — only a factor of 4 — but this may be all that is required to create devices with significant voltage gains, making graphene finally viable for a host of digital device applications. On the other hand, if this modest on/off ratio increase is not enough, it is well-known that bent graphene sheets are more chemically reactive than flat ones,[157] and so selective chemical functionalization to create a larger band gap is possible.

APPENDIX A

PROCESSING PARAMETERS

This Appendix contains the specific recipes for all processing steps in the thesis as well as supporting experimental data, where possible. Note that on non-standard tools, such as those used for graphene growth, the conditons can vary significantly between furnaces, and so only nominal parameters are given.

A.1 Nominal parameters for graphene growth and hydrogen etching

These parameters vary by furnace and depend still further on other factors such as aggregate silicon content in the crucible. As mentioned in Chapter IV, hydrogen etching is used to create atomically flat SiC surfaces.

Hydrogen etching

- Temperature: 1,400 °C

- Pressure: not evacuated

- Gas: 97% Ar 3% H_2 at 40 sccm

- Time: 30 min

Table A.1: Nominal graphene growth parameters

	C-face	Si-face	Sidewall
Temperature (°C)	1,475	1,550	1,550
Pressure (Torr)	1e-5	1e-5	1e-5
Time for 1 layer (min)	1	15	1

Table A.2: Plasma etching formulas

	Graphene	SiC 1	SiC 2
Tool	Plasma-Therm RIE	Plasma-Therm RIE	Plasma-Therm ICP
Pressure (mTorr)	100	80	10
RF1 (Platen; W)	100	200	250
RF2 (Coil; W)			500
Ar (sccm)		10	
CF_4 (sccm)			5
O_2 (sccm)	20	7	15
SF_6 (sccm)		13	

SiC_SF6M (SiC 1) Etch Rate

$y = 0.73x + 0.58$

Etch Depth (nm) vs *Etch Time* (s)
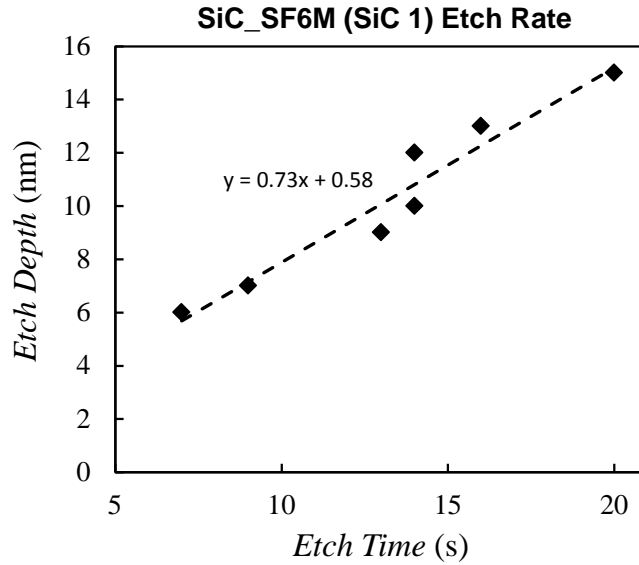
Figure A.1: Etch rate for the "SiC 1" etch.

A.2   Plasma etching formulas

Two different SiC etching formulas are used here because they serve complementary roles; noting the power difference between "SiC 1" and "SiC 2" in Table A.2, the latter etches much more quickly — but less precisely — than the former, making it appropriate when etching deep features, such as alignment marks, into the SiC.

A.3   Resist processes

ESpacer™ 300Z optional anti-charging layer:

1. Follow the procedure for spinning and baking the desired resist.

2. Spin on 200 Å ESpacer™ at 4,000 rpm with a 2,000 rpm/s ramp rate for 60 s.

3. To remove after exposure, submerge in DI water for 1 min followed by a rinse in gently-flowing DI water for 20 s.

4. Follow the procedure for developing the desired resist.

Futurrex® NR9-1500PY:

1. Spin on 1.1 μm of NR9-1500PY at 5,000 rpm with a 2,500 rpm/s ramp rate for 60 s.

2. Bake for 1 min at 150 °C.

3. Expose at 150 μC/cm^2 using 365 nm light.

4. Bake for 1 min at 100 °C.

5. Develop for 12 s in Futurrex® RD6 Developer and immediately rinse in gently-flowing DI water for 30 s followed by a gentle N_2 dry.

6. To remove, submerge for 1 minute in acetone

7. Rinse for 10 s in methanol and 10 s in isopropyl alcohol (IPA) followed by a gentle N_2 dry.

Hydrogen Silsesquioxane (HSQ):

1. Dip in and let stand in SurPass 3000 for 5 minutes.

2. Rinse in gently-flowing deionized (DI) water for 20 s and dry with an N_2 gun.

3. Spin on 100 nm 6% HSQ dissolved in methyl isobutyl ketone (MIBK) at 4,000 rpm with a 2,000 rpm/s ramp rate for 60 s. The specific type of HSQ used is marketed as Dow Corning® XR-1541.

4. Bake for 4 minutes at 80 °C.

5. A typical base dose for 100 nm features on SiC, before proximity effect correction, is about 2,000 μC/cm^2.

6. Develop for 30 s in 25% tetramethylammonium hydroxide (TMAH) and immediately rinse in gently-flowing DI water for 30 s followed by a gentle N$_2$ dry.

7. To remove, dip in Buffered Oxide Etch (BOE) 6:1 for 30 s followed by a 30 s DI water rinse and gentle N$_2$ dry.

Microposit® SC1813:

1. Spin on 1 μm of 1813 at 5,000 rpm with a 2,500 rpm/s ramp rate for 60 s.

2. Bake for 2 min at 115 °C.

3. Expose at 95 μC/cm^2 using 365 nm light.

4. Develop for 25 s in Microposit® MF 319 and immediately rinse in gently-flowing DI water for 30 s followed by a gentle N$_2$ dry.

5. To remove, submerge for 1 minute in acetone

6. Rinse for 10 s in methanol and 10 s in IPA followed by a gentle N$_2$ dry.

Polymethyl Methacrylate (PMMA):

1. Spin on 130 nm of Microchem® PMMA A4 at 4,000 rpm with a 2,000 rpm/s ramp rate for 60 s.

2. Bake for 90 s at 180 °C.

3. A typical base dose for 100 nm features on SiC, before proximity effect correction, is about 1,000 μC/cm^2.

4. Develop for 30 s in 1:2 MIBK:IPA for 3 minutes and immediately rinse in gently-flowing IPA for 20 s followed by a gentle N_2 dry.

5. To remove, submerge for 1 minute in Microposit® Remover 1165.

6. Rinse for 10 s in acetone, 10 s in methanol, and 10 s in IPA followed by a gentle N_2 dry.

ZEONREX® ZEP520a:

1. Spin on 100 nm of a pre-mixed bottle of 1:1 ZEP520a:anisole at 4,000 rpm with a 2,000 rpm/s ramp rate for 60 s.

2. Bake for 2 minutes at 180 °C.

3. A typical base dose for 100 nm features on SiC, before proximity effect correction, is about 170 $\mu C/cm^2$.

4. Develop for 2 minutes in n-Amyl acetate and immediately rinse in gently-flowing IPA for 20 s followed by a gentle N_2 dry.

5. To remove, sonicate for 15 min in 1165 if no graphene has been grown yet. Otherwise, just submerge.

6. Rinse for 10 s in acetone, 10 s in methanol, and 10 s in IPA followed by a gentle N_2 dry.

A.4   Metal liftoff processes

Negative polymer resists, e.g. Futurrex® family:

1. Submerge in acetone for 1 hour.

2. Take sample out, and while holding it over the acetone, spray a steady stream of acetone for 5 seconds, then give 5 strong but short sprays.

3. Rinse for 10 s in methanol and 10 s in IPA followed by a gentle N_2 dry.

Positive polymer resists, e.g. PMMA, ZEP:

1. Submerge in 1165 held at 70 °C for 6 hours to overnight.

2. Let cool to near room temperature, then take sample out, and while holding it over the 1165, spray a steady stream of acetone for 5 seconds, then give 10 strong but short sprays.

3. Rinse for 10 s in methanol and 10 s IPA followed by a gentle N_2 dry.

4. Inspect in microscope and repeat steps 2 and 3 until metal liftoff is satisfactory.

APPENDIX B

USEFUL CALCULATIONS

B.1   Facets of hexagonal SiC

There are multiple correct choices for the basis vectors used to index crystallographic directions in hexagonal crystals. Any two of the three vectors in Figure B.1 will specify the lattice, with the third vector being a linear combination of the other two. However, to eludicate this three-fold symmetry that exists in hexagonal lattice directions, four Miller indices — three in-plane and one out-of-plane — are used for specifying surfaces and directions in hexagonal SiC. The notation for a surface is $(hk\overline{h+k}l)$, where l is the out-of-plane index and $\overline{h+k}$ represents the redundant third in-plane index. All indices are integers.

Indexing and calculating the angles of the facets of hexagonal SiC are straightforward. Let the real space basis vectors of hexagonal SiC be given by

$$\mathbf{a_1} = a\left(\frac{\sqrt{3}}{2}, -\frac{1}{2}, 0\right) \tag{B.1a}$$

$$\mathbf{a_2} = a\left(-\frac{\sqrt{3}}{2}, -\frac{1}{2}, 0\right) \tag{B.1b}$$

$$\mathbf{a_3} = c(0, 0, 1), \tag{B.1c}$$

where a and c are the in- and out-of-plane lattice constants, respectively. In the case of 4H SiC, these are $a = 3.079$ Å and $c = 10.081$ Å, respectively.[158] A surface $(hk\overline{h+k}l)$ in Miller indices corresponds to a surface in reciprocal space with a normal $\mathbf{b} = h\mathbf{b_1} + k\mathbf{b_2} + l\mathbf{b_3}$, where $\mathbf{b_1}$, $\mathbf{b_2}$ and $\mathbf{b_3}$ are the reciprocal lattice vectors of $\mathbf{a_1}$, $\mathbf{a_2}$ and $\mathbf{a_3}$, respectively, given by
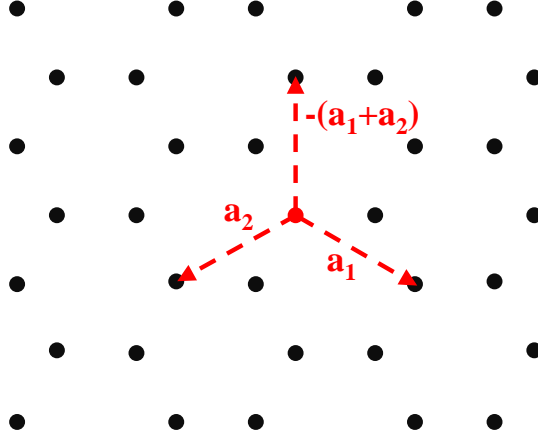
Figure B.1: Overcomplete basis vectors of a hexagonal lattice.

$$\mathbf{b_1} = \frac{4\pi}{\sqrt{3}a}\left(\frac{1}{2}, \frac{\sqrt{3}}{2}, 0\right) \tag{B.2a}$$

$$\mathbf{b_2} = \frac{4\pi}{\sqrt{3}a}\left(-\frac{1}{2}, \frac{\sqrt{3}}{2}, 0\right) \tag{B.2b}$$

$$\mathbf{b_3} = \frac{2\pi}{c}(0, 0, 1). \tag{B.2c}$$

Using these equations, we can determine that the magnitude in real space of a purely in-plane reciprocal lattice vector $\mathbf{b} = h\mathbf{b_1} + k\mathbf{b_2}$ would be $\frac{2\pi}{||h\mathbf{b_1}+k\mathbf{b_2}||} = \frac{2\pi}{\frac{4\pi}{\sqrt{3}a}\sqrt{h^2+hk+k^2}} = \frac{\sqrt{3}a}{2\sqrt{h^2+hk+k^2}}$ and, similarly, that the magnitude in real space of a purely out-of-plane reciprocal lattice vector $\mathbf{b} = l\mathbf{b_3}$ would be $\frac{2\pi}{l||\mathbf{b_3}||} = \frac{c}{l}$. These observations allow for the calculation of the real space inclination angle θ_{hkl} of a plane with Miller indices h, k, and l with respect to the $\{0001\}$ surfaces as

$$\theta_{hkl} = \arctan\left(\frac{\frac{c}{l}}{\frac{\sqrt{3}a}{2\sqrt{h^2+hk+k^2}}}\right) = \arctan\left(\frac{2c\sqrt{h^2 + hk + k^2}}{\sqrt{3}al}\right). \tag{B.3}$$

Table B.1 gives the incline angles from the $\{0001\}$ surfaces of both the $(10\bar{1}n)$ and $(11\bar{2}n)$ surfaces for 4H SiC.

Table B.1: Inclination angles with respect to the 4H SiC {0001} surfaces of both the $(10\bar{1}n)$ and $(11\bar{2}n)$ surfaces

n	$(10\bar{1}n)$	$(11\bar{2}n)$
1	75.2°	81.3°
2	62.1°	73.0°
3	51.6°	65.4°
4	43.4°	58.6°
5	37.1°	52.6°
6	32.2°	47.5°
7	28.4°	43.1°
8	25.3°	39.3°
9	22.8°	36.0°
10	20.7°	33.2°
11	19.0°	30.8°
12	17.5°	28.6°
13	16.2°	26.7°
14	15.1°	25.1°
15	14.1°	23.6°
16	13.3°	22.3°
17	12.5°	21.1°
18	11.9°	20.0°
19	11.3°	19.0°
20	10.7°	18.1°

APPENDIX C

SPECIAL ANALYTICAL METHODS

This Appendix contains the details of some special analytical methods used to study data presented in this thesis. They have been included here for easy reference because it is unlikely that these methods would be detailed in the literature.

C.1 Automated ARPES cone identification

The vast quantities of data generated by ARPES on C-face graphene over multiple runs necessitated a means to automatically plot and analyze each image. Part of this effort involved automatically identifying cones in an image so that their locations in reciprocal space as well as their slopes could efficiently extracted. Identifying these bands made possible other, more complicated, analyses, such as automatically fitting the increases in the width of the bands with higher binding energy.

The Hough transform, a well-known image analysis technique,[159] was used to indentify bands in our data. This transform involves identifying points likely to belong to a band, drawing many lines at different angles through those points, computing the angles and distances of each of those lines to some fixed origin, and keeping statistics on the occurrences of these distances/angles. If a given angle/distance combination shows up often, a line with those properties likely exists in the data. The process, which is illustrated in Figure C.1, is outlined below:

1. Start with noise-filtered ARPES data.

2. Find points in the data that correspond to local intensity maxima. The process can be refined by throwing out maxima that are too low relative to the background noise, or by keeping only the highest n points.

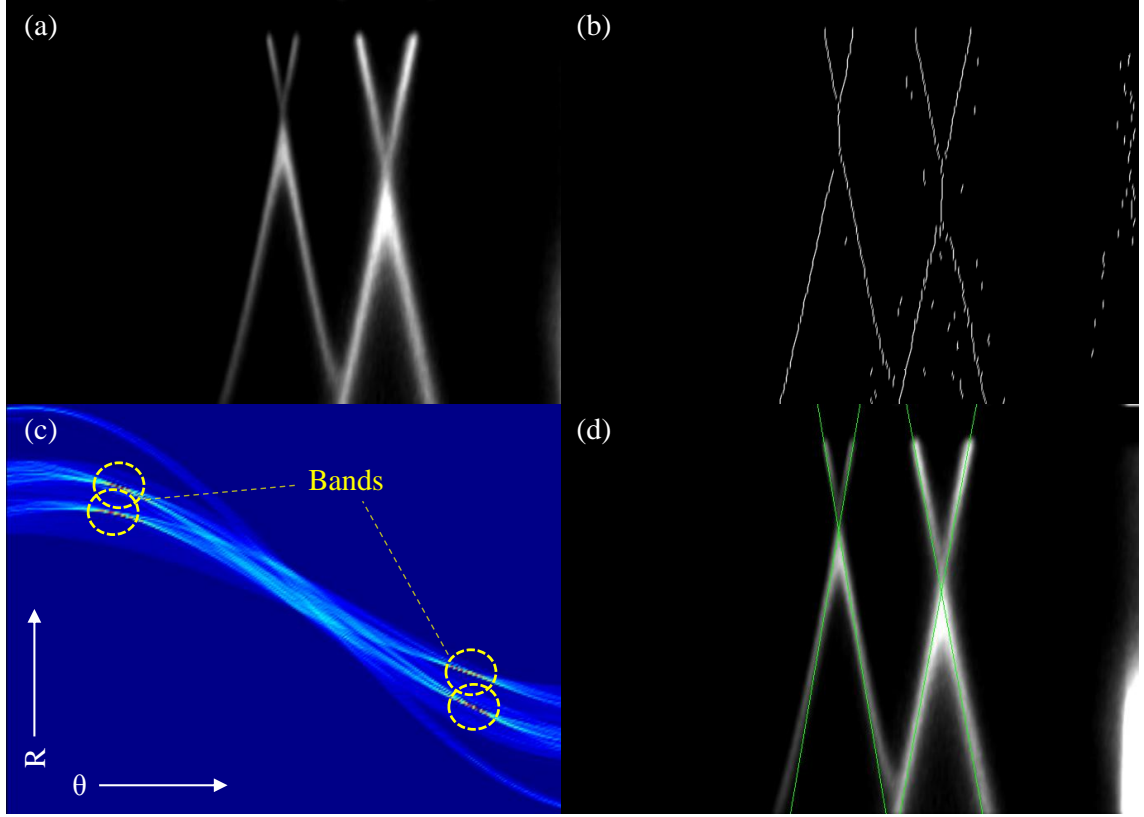**Figure C.1:** Automated band finding process. (a) Starting ARPES picture. (b) Plot of local intensity maxima found in (a). (c) Angle/distance binning plot, following the Hough transform, for the collection of points in (b), highlighting the areas where the bin count is high, indicating the existence of particular bands in (b). (d) Angles/distances from the areas identified in (c) converted back into lines and overlaid on (a).

3. Compute the distances R to the origin of lines with angle θ passing through each identified intensity peak, repeating for many θ.

4. For each θ, increment the bin corresponding to the distance computed.

5. After all the local maxima from the ARPES data are analyzed, find local maxima from the θ and R binning. In a plot of θ/R bins, these maxima are always located at the confluence of many curves. These maxima are the bands found by the algorithm.

C.2   SiC background subtraction of Raman spectra

The Raman spectrum of epitaxial graphene on SiC is a sum of contributions from both the graphene and the SiC, which overlap in some regions, necessitating the subtraction of the SiC "background" signal. This subtraction is performed, as shown in Figure C.2 by obtaining the Raman spectrum of bare SiC and subtracting its normalized spectrum from the graphene + SiC Raman spectrum. The feature of choice to normalize Raman spectra to, as shown in Figure C.2(b) is a road, flat shoulder in the SiC spectrum between 1,800 and 1,900 cm^{-1}. The complete steps are as follows:

1. Subtract the constant background from both the raw graphene + SiC spectrum as well as the reference SiC spectrum.

2. Scale the SiC spectrum to have the same intensity between 1,800 and 1,900 cm^{-1} as in the graphene + SiC spectrum.

3. Subtract the scaled SiC spectrum from the graphene + SiC spectrum.

The best reference SiC spectrum is obtained by focusing the optical lens beneath the graphene whose Raman spectrum is to be isolated.
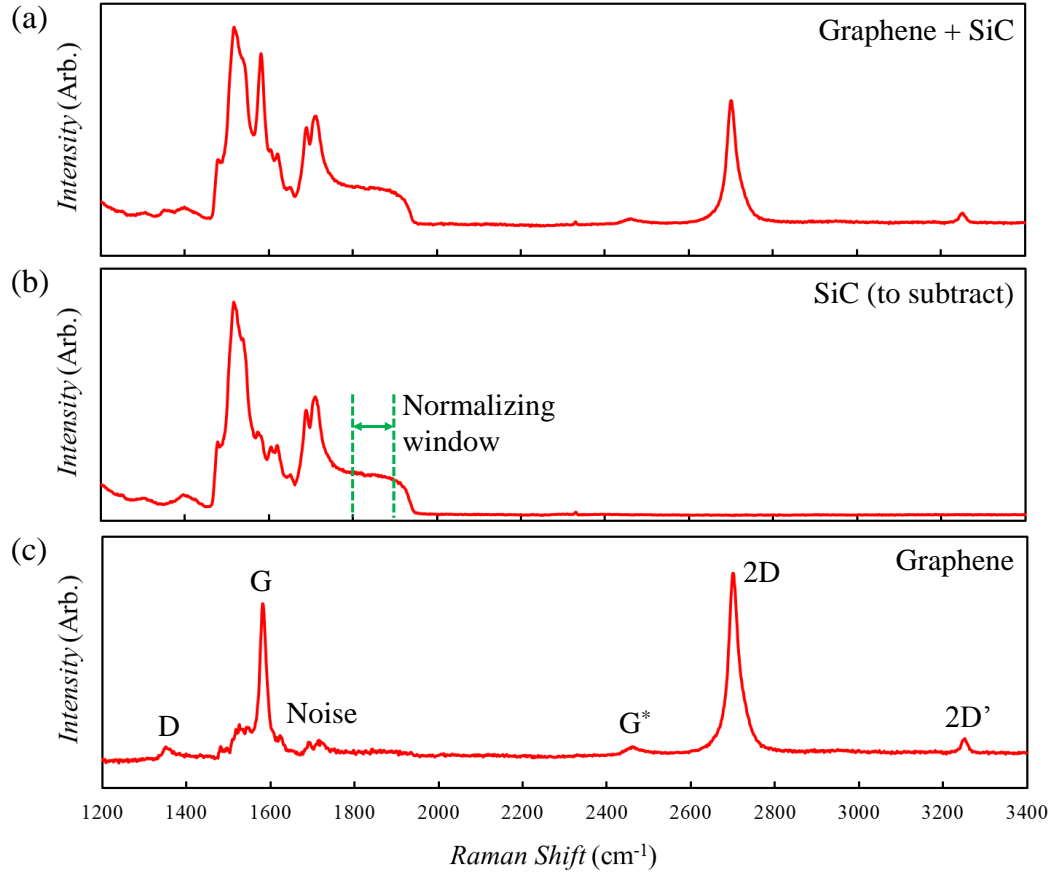
Figure C.2: SiC background subtraction from epitaxial graphene Raman spectra. (a) Raw epitaxial graphene spectrum. (b) Bare SiC spectrum, showing the intensity window used as a reference for scaling Raman spectra. (c) Spectrum of (a) after subtracting (b), with all visible graphene peaks labeled for clarity.

REFERENCES

[1] M. Sprinkle, D. Siegel, Y. Hu, J. Hicks, A. Tejeda, A. Taleb-Ibrahimi, P. Le Fèvre, F. Bertran, S. Vizzini, H. Enriquez, S. Chiang, P. Soukiassian, C. Berger, W. A. de Heer, A. Lanzara, and E. H. Conrad, "First direct observation of a nearly ideal graphene band structure," *Phys. Rev. Lett.*, vol. 103, no. 22, p. 226803, 2009.

[2] J. Hicks, M. Sprinkle, K. Shepperd, F. Wang, A. Tejeda, A. Taleb-Ibrahimi, F. Bertran, P. Le Fèvre, W. A. de Heer, C. Berger, and E. H. Conrad, "Symmetry breaking in commensurate graphene rotational stacking: Comparison of theory and experiment," *Phys. Rev. B*, vol. 83, no. 20, p. 205403, 2011.

[3] J. Hicks, R. Arora, E. Kenyon, P. S. Chakraborty, H. Tinkey, J. Hankinson, C. Berger, W. A. de Heer, E. H. Conrad, and J. D. Cressler, "X-ray radiation effects in multilayer epitaxial graphene," *Appl. Phys. Lett.*, vol. 99, no. 23, p. 232102, 2011.

[4] J. Hicks and E. H. Conrad, "Graphene investigated by synchrotron radiation," *MRS Bull.*, vol. 37, no. 12, pp. 1203–1213, 2012.

[5] J. Hicks, A. Tejeda, A. Taleb-Ibrahimi, M. S. Nevius, F. Wang, K. Shepperd, J. Palmer, F. Bertran, P. Le Fèvre, J. Kunc, W. A. de Heer, C. Berger, and E. H. Conrad, "A wide-bandgap metal-semiconductor-metal nanostructure made entirely from graphene," *Nature Phys.*, vol. 9, no. 1, pp. 49–54, 2013.

[6] I. Meric, M. Y. Han, A. F. Young, B. Ozyilmaz, and P. Kim, "Current saturation in zero-bandgap, top-gated graphene field effect transistors," *Nature Nanotech.*, vol. 3, pp. 654–659, 2008.

[7] P. R. Wallace, "Band theory of graphite," *Physical Review*, vol. 71, no. 9, pp. 622–634, 1947.

[8] S. Reich, J. Maultzsch, C. Thomsen, and P. Ordejón, "Tight-binding description of graphene," *Phys. Rev. B*, vol. 66, no. 3, p. 035412, 2002.

[9] K. S. Novoselov, A. K. Geim, S. V. Morozov, D. Jiang, Y. Zhang, S. V. Dubonos, I. V. Grigorieva, and A. A. Firsov, "Electric field effect in atomically thin carbon films," *Science*, vol. 22, no. 5696, pp. 666–669, 2004.

[10] B. Huard, N. Stander, J. A. Sulpizio, and D. Goldhaber-Gordon, "Evidence of the role of contacts on the observed electron-hole asymmetry in graphene," *Phys. Rev. B*, vol. 78, no. 12, p. 121402, 2008.

[11] J. S. Bunch, S. S. Verbridge, J. S. Alden, A. M. van der Zande, J. M. Parpia, H. G. Craighead, and P. L. McEuen, "Impermeable atomic membranes from graphene sheets," *Nano Lett.*, vol. 8, no. 8, pp. 2458–2462, 2008.

[12] S. Chen, L. Brown, M. Levendorf, W. Cai, S.-Y. Ju, J. Edgeworth, X. Li, C. W. Magnuson, A. Velamakanni, R. D. Piner, J. Kang, J. Park, and R. S. Ruoff, "Oxidation resistance of graphene-coated cu and Cu/Ni alloy," *ACS Nano*, vol. 5, no. 2, pp. 1321–1327, 2011.

[13] G. F. Schneider, S. W. Kowalczyk, V. E. Calado, G. Pandraud, H. W. Zandbergen, L. M. K. Vandersypen, and C. Dekker, "DNA translocation through graphene nanopores," *Nano Lett.*, vol. 10, no. 8, pp. 3163–3167, 2010.

[14] S. W. Johnston, V. M. Dubin, M. L. McSwiney, and P. Moon, "Forming a copper diffusion barrier," Patent US 8 227 335, July 24, 2012.

[15] R. R. Nair, P. Blake, A. N. Grigorenko, K. S. Novoselov, T. J. Booth, T. Stauber, N. M. R. Peres, and A. K. Geim, "Fine structure constant defines visual transparency of graphene," *Science*, vol. 320, no. 5881, p. 1308, 2008.

[16] S. Bae, H. Kim, Y. Lee, X. Xu, J.-S. Park, Y. Zheng, J. Balakrishnan, T. Lei, H. R. Kim, Y. I. Song, Y.-J. Kim, K. S. Kim, B. Özyilmaz, J.-H. Ahn, B. H. Hong, and S. Iijima, "Roll-to-roll production of 30-inch graphene films for transparent electrodes," *Nature Nano.*, vol. 5, pp. 574–578, 2010.

[17] X. Wang, L. Zhi, and K. Müllen, "Transparent, conductive graphene electrodes for dye-sensitized solar cells," *Nano Lett.*, vol. 8, no. 1, pp. 323–327, 2008.

[18] M. Green, *Solar Cells: Operating Principles, Technology, and System Applications*, 1st ed. Sydney: University of New South Wales, 1986.

[19] A. B. Kuzmenko, E. van Heumen, F. Carbone, and D. van der Marel, "Universal optical conductance of graphite," *Phys. Rev. Lett.*, vol. 100, no. 11, p. 117401, 2008.

[20] Z. Q. Li, E. A. Henriksen, Z. Jiang, Z. Hao, M. C. Martin, P. Kim, H. L. Stormer, and D. N. Basov, "Dirac charge dynamics in graphene by infrared spectroscopy," *Nature Phys.*, vol. 4, pp. 532–535, 2008.

[21] D. S. Ginley and C. Bright, "Transparent conducting oxides," *MRS Bull.*, vol. 25, no. 8, pp. 15–18, 2000.

[22] K. S. Novoselov, D. Jiang, F. Schedin, T. J. Booth, V. V. Khotkevich, S. V. Morozov, and A. K. Geim, "Two-dimensional atomic crystals," *Nat. Acad. Sci. Proc.*, vol. 102, no. 30, pp. 10 451–10 453, 2005.

[23] C. Berger, Z. Song, T. Li, X. Li, A. Y. Ogbazghi, R. Feng, Z. Dai, A. N. Marchenkov, E. H. Conrad, P. N. First, and W. A. de Heer, "Ultrathin epitaxial graphite: 2D electron gas properties and a route toward graphene-based nanoelectronics," *J. Phys. Chem. B*, vol. 108, no. 52, pp. 19 912–19 916, 2004.

[24] S. Stankovich, R. D. Piner, X. Chen, N. Wu, S. T. Nguyen, and R. S. Ruoff, "Stable aqueous dispersions of graphitic nanoplatelets *via* the reduction of exfoliated graphite oxide in the presence of poly(sodium 4-styrenesulfonate)," *J. Mater. Chem.*, vol. 16, pp. 155–158, 2006.

[25] W. S. Hummers and R. E. Offeman, "Preparation of graphitic oxide," *J. Am. Chem. Soc.*, vol. 80, no. 6, p. 1339, 1958.

[26] A. Reina, X. Jia, J. Ho, D. Nezich, H. Son, V. Bulovic, M. S. Dresselhaus, and J. Kong, "Large area, few-layer graphene films on arbitrary substrates by chemical vapor deposition," *Nano Lett.*, vol. 9, no. 1, pp. 30–35, 2009.

[27] X. Li, W. Cai, J. An, S. Kim, J. Nah, D. Yang, R. Piner, A. Velamankanni, I. Jung, E. Tutuc, S. K. Banerjee, L. Colombo, and R. S. Ruoff, "Large-area synthesis of high-quality and uniform graphene films on copper foils," *Science*, vol. 5, no. 5932, pp. 1312–1314, 2009.

[28] P. W. Sutter, J.-I. Flege, and E. A. Sutter, "Epitaxial graphene on ruthenium," *Nature Mater.*, vol. 7, pp. 406–411, 2008.

[29] S. Stankovich, D. A. Dikin, R. D. Piner, K. A. Kohlhaas, A. Kleinhammes, Y. Jia, Y. Wu, S. T. Nguyen, and R. S. Ruoff, "Synthesis of graphene-based nanosheets via chemical reduction of exfoliated graphite oxide," *Carbon*, vol. 45, no. 7, pp. 1558–1565, 2007.

[30] H. Wang, A. Hsu, K. K. Kim, J. Kong, and T. Palacios, "Gigahertz ambipolar frequency multiplier based on CVD graphene," *Proc. IEEE Int. El. Devices Meet.*, pp. 23.6.1–23.6.4, 2010.

[31] W. A. de Heer, C. Berger, M. Ruan, M. Sprinkle, X. Li, Y. Hu, B. Zhang, J. Hankinson, and E. H. Conrad, "Large area and structured epitaxial graphene produced by confinement controlled sublimation of silicon carbide," *Nat. Acad. Sci. Proc.*, vol. 108, no. 41, pp. 16 900–16 905, 2011.

[32] J. S. Moon, D. Curtis, M. Hu, D. Wong, C. McGuire, P. M. Campbell, G. Jernigan, J. L. Tedesco, B. VanMil, R. Myers-Ward, C. Eddy, and D. K. Gaskill, "Epitaxial-graphene RF field-effect transistors on Si-face 6H-SiC substrates," *IEEE Elec. Dev. Lett.*, vol. 30, no. 6, pp. 650–652, 2009.

[33] Y.-M. Lin, C. Dimitrakopoulos, K. A. Jenkins, D. B. Farmer, H.-Y. Chiu, A. Grill, and P. Avouris, "100-ghz transistors from wafer-scale epitaxial graphene," *Science*, vol. 327, no. 5966, p. 662, 2010.

[34] Z. Guo, R. Dong, P. S. Chakraborty, N. Lourenco, J. Palmer, Y. Hu, M. Ruan, J. Hankinson, J. Kunc, J. D. Cressler, C. Berger, and W. A. de Heer, "Record maximum oscilation frequency in c-face epitaxial graphene transistors," *Nano Lett.*, vol. 13, no. 3, pp. 942–947, 2013.

[35] Y. Zhang, Y.-W. Tan, H. L. Stormer, and P. Kim, "Experimental observation of the quantum Hall effect and Berry's phase in graphene," *Nature*, vol. 438, no. 7065, pp. 201–204, 2005.

[36] A. C. Ferrari, J. C. Meyer, V. Scardaci, C. Casiraghi, M. Lazzeri, F. Mauri, S. Piscanec, D. Jiang, K. S. Novoselov, S. Roth, and A. K. Geim, "Raman spectrum and graphene and graphene layers," *Phys. Rev. Lett.*, vol. 97, no. 18, p. 187401, 2006.

[37] S. Russo, J. B. Oostinga, D. Wehenkel, H. B. Heersch, S. S. Sobhani, L. M. K. Vandersypen, and A. F. Morpurgo, "Observation of Aharonov-Bohm conductance oscillations in a graphene ring," *Phys. Rev. B*, vol. 77, no. 8, p. 085413, 2008.

[38] S. Y. Zhou, G.-H. Gweon, J. Graf, A. V. Fedorov, C. D. Spataru, R. D. Diehl, Y. Kopelevich, D.-H. Lee, S. G. Louie, and A. Lanzara, "First direct observation of Dirac fermions in graphite," *Nature Phys.*, vol. 2, pp. 595–599, 2006.

[39] G. Eda, G. Fanchini, and M. Chhowalla, "Large-area ultrathin films of reduced graphene oxide as a transparent and flexible electronic material," *Nature Nanotech.*, vol. 3, no. 5, pp. 270–274, 2008.

[40] L. J. Cote, R. Cruz-Silva, and J. Huang, "Flash reduction and patterning of graphite oxide and its polymer composite," *J. Am. Chem. Soc.*, vol. 131, no. 31, pp. 11 027–11 032, 2009.

[41] Z. Wei, S. Kim, S.-Y. Kim, Y. Hu, M. K. Yakes, A. R. Laracuente, Z. Dai, S. R. Marder, C. Berger, W. P. King, W. A. de Heer, P. E. Sheehan, and E. Riedo, "Nanoscale tunable reduction of graphene oxide for graphene electronics," *Science*, vol. 328, no. 5984, pp. 1373–1376, 2010.

[42] D. V. Kosynkin, A. L. Higginbotham, A. Sinitskii, J. R. Lomeda, A. Dimiev, B. K. Price, and J. M. Tour, "Longitudinal unzipping of carbon nanotubes to form graphene nanoribbons," *Nature*, vol. 458, pp. 872–876, 2009.

[43] S. A. Campbell, *Fabrication Engineering at the Micro- and Nanoscale*, 3rd ed. New York: Oxford University Press, 2008.

[44] A. Reina, S. Thiele, X. Jia, S. Bhaviripudi, M. S. Dresselhaus, J. A. Schaefer, and J. Kong, "Growth of large-area single- and bi-layer graphene by controlled

carbon precipitation on polycrystalline ni surfaces," *Nano Research*, vol. 2, no. 6, pp. 509–516, 2009.

[45] X. Li, W. Cai, L. Colombo, and R. S. Ruoff, "Evolution of graphene growth on ni and cu by carbon isotope labeling," *Nano Lett.*, vol. 9, no. 12, pp. 4268–4272, 2009.

[46] M. S. Dresselhaus and G. Dresselhaus, "Intercalation compounds of graphite," *Advances in Physics*, vol. 30, no. 2, pp. 139–326, 1981.

[47] X. Li, C. W. Magnuson, A. Venugopal, R. M. Tromp, J. B. Hannon, E. M. Vogel, L. Colombo, and R. S. Ruoff, "Large-area graphene single crystals grown by low-pressure chemical vapor deposition of methane on copper," *J. Am. Chem. Soc.*, vol. 133, no. 9, pp. 2816–2819, 2011.

[48] D. V. Badami, "X-Ray studies of graphite formed by decomposing silicon carbide," *Carbon*, vol. 3, no. 1, pp. 53–57, 1965.

[49] A. J. Van Bommel, J. E. Crombeen, and A. Van Tooren, "LEED and Auger electron observations of the SiC(0001) surface," *Surface Science*, vol. 48, no. 2, pp. 463–472, 1975.

[50] M. Orlita, C. Faugeras, P. Plochocka, P. Neugebauer, G. Martinez, D. K. Maude, A.-L. Barra, M. Sprinkle, C. Berger, W. A. de Heer, and M. Potemski, "Approaching the Dirac point in high-mobility multilayer epitaxial graphene," *Phys. Rev. Lett.*, vol. 101, no. 26, p. 267601, 2008.

[51] K. V. Emtsev, A. Bostwick, K. Horn, J. Jobst, G. L. Kellogg, L. Ley, J. L. McChesney, T. Ohta, S. A. Reshanov, J. Rhrl, E. Rotenberg, A. K. Schmid, D. Waldmann, H. B. Weber, and T. Seyller, "Towards wafer-size graphene layers by atmospheric pressure graphitization of silicon carbide," *Nature Mater.*, vol. 8, pp. 203–207, 2009.

[52] R. M. Tromp and J. B. Hannon, "Thermodynamics and kinetics of graphene growth on SiC(0001)," *Phys. Rev. Lett.*, vol. 102, no. 10, p. 106104, 2009.

[53] T. Ohta, A. Bostwick, J. L. McChesney, T. Seyller, K. Horn, and E. Rotenberg, "Interlayer interaction and electronic screening in multilayer graphene investigated with Angle-Resolved Photoemission Spectroscopy," *Phys. Rev. Lett.*, vol. 98, no. 20, p. 206802, 2007.

[54] M. Sprinkle, J. Hicks, A. Tejeda, A. Taleb-Ibrahimi, P. Le Fèvre, F. Bertran, H. Tinkey, M. C. Clark, P. Soukiassian, D. Martinotti, J. Hass, W. A. de Heer, C. Berger, and E. H. Conrad, "Multilayer epitaxial graphene grown on the SiC (000$\bar{1}$) surface; structure and electronic properties," *J. Phys. D*, vol. 43, no. 37, p. 374006, 2010.

[55] M. P. Seah and W. A. Dench, "Quantitative electron spectroscopy of surfaces: A standard data base for electron inelastic mean free paths in solids," *Surface and Interface Analysis*, vol. 1, no. 1, pp. 2–11, 1979.

[56] J. Hicks, K. Shepperd, F. Wang, and E. H. Conrad, "The structure of graphene grown on the SiC (000$\bar{1}$) surface," *J. Phys. D: Appl. Phys.*, vol. 45, no. 15, p. 154002, 2012.

[57] D. Sun, Z.-K. Wu, C. Divin, X. Li, C. Berger, W. A. de Heer, P. N. First, and T. B. Norris, "Ultrafast relaxation of excited Dirac fermions in epitaxial graphene using Optical Differential Transmission Spectroscopy," *Phys. Rev. Lett.*, vol. 101, no. 15, p. 157402, 2008.

[58] D. L. Miller, K. Kubista, G. M. Rutter, M. Ruan, W. A. de Heer, P. N. First, and J. A. Stroscio, "Observing the quantization of zero mass carriers in graphene," *Science*, vol. 324, no. 5929, pp. 924–927, 2009.

[59] A. Bostwick, T. Ohta, T. Seyller, K. Horn, and E. Rotenberg, "Quasiparticle dynamics in graphene," *Nature Phys.*, vol. 3, pp. 36–40, 2007.

[60] Y.-W. Tan, Y. Zhang, K. Bolotin, Y. Zhao, E. H. Hwang, S. D. Sarma, H. L. Stormer, and P. Kim, "Measurement of scattering rate and minimum conductivity in graphene," *Phys. Rev. Lett.*, vol. 99, no. 24, p. 246803, 2007.

[61] J. Hass, F. Varchon, J. E. Millán-Otoya, M. Spinkle, N. Sharma, W. A. de Heer, C. Berger, P. N. First, L. Magaud, and E. H. Conrad, "Why multilayer graphene on SiC (000$\bar{1}$) behaves like a single sheet of graphene," *Phys. Rev. Lett.*, vol. 100, no. 12, p. 125504, 2008.

[62] J. M. B. Lopes dos Santos, N. M. R. Peres, and A. H. Castro Neto, "Graphene bilayer with a twist: Electronic structure," *Phys. Rev. Lett.*, vol. 99, no. 25, p. 256802, 2007.

[63] G. Trambly de Laissardière, D. Mayou, and L. Magaud, "Localization of Dirac electrons in rotated graphene bilayers," *Nano Lett.*, vol. 10, pp. 804–808, 2010.

[64] E. J. Mele, "Commensuration and interlayer coherence in twisted bilayer graphene," *Phys. Rev. B*, vol. 81, no. 16, p. 161405, 2010.

[65] S. Latil, V. Meunier, and L. Henrard, "Massless fermions in multilayer graphitic systems with misoriented layers: *Ab initio* calculations and experimental fingerprints," *Phys. Rev. B*, vol. 76, no. 20, p. 201402, 2007.

[66] G. Li, A. Luican, J. M. B. Lopes dos Santos, A. H. Castro Neto, A. Reina, J. Kong, and E. Y. Andrei, "Observation of Van Hove singularities in twisted bilayer graphene," *Nature Phys.*, vol. 6, pp. 109–113, 2009.

[67] A. Luican, G. Li, A. Reina, J. Kong, R. R. Nair, K. S. Novoselov, A. K. Geim, and E. Y. Andrei, "Single-layer behavior and its breakdown in twisted graphene layers," *Phys. Rev. Lett.*, vol. 106, no. 12, p. 126802, 2011.

[68] R. W. Havener, H. Zhuang, L. Brown, R. G. Hennig, and J. Park, "Angle-resolved Raman imaging of interlayer rotations and interactions in twisted bilayer graphene," *Nano Lett.*, vol. 12, no. 6, pp. 3162–3167, 2012.

[69] K. Kim, S. Coh, L. Z. Tan, W. Regen, J. M. Yuk, E. Chatterjee, M. F. Crommie, M. L. Cohen, S. G. Louie, and A. Zettl, "Raman spectroscopy study of rotated double-layer graphene: Misorientation-angle dependence of electronic structure," *Phys. Rev. Lett.*, vol. 108, no. 24, p. 246103, 2012.

[70] T. Ohta, J. T. Robinson, P. J. Feibelman, A. Bostwick, E. Rotenberg, and T. E. Beechem, "Evidence for interlayer coupling and Moiré periodic potentials in twisted bilayer graphene," *Phys. Rev. Lett.*, vol. 109, no. 18, p. 186807, 2012.

[71] I. Brihuega, P. Mallet, H. González-Herrero, G. Trambly de Lassardière, M. M. Ugeda, L. Magaud, J. M. Gómez-Rodríguez, F. Ynduráin, and J.-Y. Veuillen, "Unraveling the intrinsic and robust nature of van Hove singularities in twisted bilayer graphene by scanning tunneling microscopy and theoretical analysis," *Phys. Rev. Lett.*, vol. 109, no. 19, p. 196802, 2012.

[72] W.-T. Pong and C. Durkan, "A review and outlook for an anomaly of Scanning Tunelling Microscopy (STM): superlattices on graphite," *J. Phys. D*, vol. 38, no. 21, pp. R329–R355, 2005.

[73] J. Hass, R. Feng, J. E. Millán-Otoya, X. Li, P. N. First, W. A. de Heer, and E. H. Conrad, "Structural properties of multilayer graphene/ 4H-SiC (000$\bar{1}$) system as determined by Surface X-Ray Diffraction," *Phys. Rev. B*, vol. 75, no. 21, p. 214109, 2007.

[74] C. Mathieu, N. Barrett, J. Rault, Y. Y. Mi, B. Zhang, W. A. de Heer, C. Berger, E. H. Conrad, and O. Renault, "Microscopic correlation between chemical and electronic states in epitaxial graphene on SiC (000$\bar{1}$)," *Phys. Rev. B*, vol. 83, no. 23, p. 235436, 2011.

[75] I. Gierz, J. Henk, H. Höchst, C. R. Ast, and K. Kern, "Illuminating the dark corridor in graphene: Polarization dependence of Angle-Resolved Photoemission Spectroscopy on graphene," *Phys. Rev. B*, vol. 83, no. 12, p. 121408, 2011.

[76] T. K. Gaisser, *Cosmic Rays and Particle Physics*, 1st ed. Cambridge: Cambridge University Press, 1991.

[77] S. P. Swordy, "The energy spectra and anisotropies of cosmic rays," *Space Sci. Rev.*, vol. 99, no. 1–4, pp. 85–94, 2001.

[78] G. A. Bazilevskaya, I. G. Usoskin, E. O. Flückiger, R. G. Harrison, L. Desorgher, R. Bütikofer, M. B. Krainev, V. S. Makhmutov, Y. I. Stozhkov, A. K. Svirzhevskaya, and *et al.*, "Cosmic ray induced ion production in the atmosphere," *Space Sci. Rev.*, vol. 137, no. 1–4, pp. 149–173, 2008.

[79] J. R. Srour and J. M. McGarrity, "Radiation effects on microelectronics in space," *Proc. IEEE*, vol. 76, no. 11, pp. 1443–1469, 1988.

[80] E. G. Stassinopoulos and J. P. Raymond, "The space radiation environment for electronics," *Proc. IEEE*, vol. 76, no. 11, pp. 1423–1442, 1988.

[81] K. F. Galloway and R. D. Schrimpf, "MOS device degradation due to total ionizing radiation in the natural space environment: A review," *Microelectr J.*, vol. 21, no. 2, pp. 67–81, 1990.

[82] J. H. W. Simmons, *Radiation damage in graphite*, ser. International series of monographs in nuclear energy. Oxford: Pergamon Press, 1965.

[83] E. Fermi and L. Szillard, "Neutronic reactor," Patent US 2 708 656, May 17, 1955.

[84] W.-K. Hong, C. Lee, D. Nepal, K. E. Geckeler, K. Shin, and T. Lee, "Radiation hardness of the electrical properties of carbon nanotube field effect transistors under high-energy proton irradiation," *Nanotechnol.*, vol. 17, no. 22, pp. 5675–5680, 2006.

[85] V. Skákalová, A. B. Kaiser, U. Dettlaff, K. Arstila, A. V. Krasheninnikov, J. Keinonen, and S. Roth, "Electrical properties of C^{4+} irradiated single-walled carbon nanotube paper," *Phys. Status Solidi B*, vol. 245, no. 10, pp. 2280–2283, 2008.

[86] X.-W. Tang, Y. Yang, W. Kim, Q. Wang, P. Qi, H. Dai, and L. Xing, "Measurement of ionizing radiation using carbon nanotube field effect transistor," *Phys. Med. Biol.*, vol. 50, no. 3, pp. N23–N31, 2005.

[87] C. D. Cress, C. M. Schauerman, B. J. Landi, S. R. Messenger, R. P. Raffaelle, and R. J. Walters, "Radiation effects in single-walled carbon nanotube papers," *J. Appl. Phys.*, vol. 107, no. 1, p. 014316, 2010.

[88] C. D. Cress, J. J. McMorrow, J. T. Robinson, A. L. Friedman, and B. J. Landi, "Radiation effects in single-walled carbon nanotube thin-film-transistors," *IEEE Trans. Nucl. Sci.*, vol. 57, no. 6, pp. 3040–3045, 2010.

[89] J. Guo, Y. Li, S. Wu, and W. Li, "The effects of γ-irradiation dose on chemical modification of multi-walled carbon nanotubes," *Nanotechnology*, vol. 16, no. 10, pp. 2385–2388, 2005.

[90] P. Esquinazi, D. Spemann, R. Höhne, A. Setzer, K.-H. Han, and T. Butz, "Induced magnetic ordering by proton irradiation in graphite," *Phys. Rev. Lett.*, vol. 91, no. 22, p. 227201, 2003.

[91] C. D. Cress, J. J. McMorrow, J. T. Robinson, B. J. Landi, S. M. Hubbard, and S. R. Messenger, "Radiation effects in carbon nanoelectronics," *Electronics*, vol. 1, no. 1, pp. 23–31, 2012.

[92] E. X. Zhang, A. K. M. Newaz, B. Wang, S. Bhandaru, C. X. Zhang, D. M. Fleetwood, K. I. Bolotin, S. T. Pantelides, M. L. Alles, R. D. Schrimpf, S. M. Weiss, R. A. Reed, and R. A. Weller, "Low-energy x-ray and ozone-exposure induced defect formation in graphene materials and devices," *IEEE Trans. Nuc. Sci*, vol. 58, no. 6, pp. 2961–2967, 2011.

[93] S. Y. Zhou, Ç. Ö. Girit, A. Scholl, C. J. Jozwiak, D. A. Siegel, P. Yu, J. T. Robinson, F. Wang, A. Zettl, and A. Lanzara, "Instability of two-dimensional graphene: Breaking sp^2 bonds with soft x rays," *Phys. Rev. B*, vol. 80, no. 12, p. 121409, 2009.

[94] M. Sprinkle, "Epitaxial graphene on silicon carbide: Low-vacuum growth, characterization, and device fabrication," Ph.D. dissertation, Georgia Institute of Technology, 2010.

[95] D. B. Farmer, Y.-M. Lin, and P. Avouris, "Graphene field-effect transistors with self-aligned gates," *Appl. Phys. Lett.*, vol. 97, no. 1, p. 013103, 2010.

[96] M. Guggisberg, M. Bammerlin, C. Loppacher, O. Pfeiffer, A. Abdurixit, V. Barwich, R. Bennewitz, A. Baratoff, E. Meyer, and H.-J. Güntherodt, "Separation of interactions by noncontact force microscopy," *Phys. Rev. B*, vol. 61, no. 16, pp. 11 151–11 155, 2000.

[97] C. Berger, Z. Song, X. Li, x. Wu, N. Brown, C. Naud, D. Mayou, T. Li, J. Hass, A. N. Marchenkov, E. H. Conrad, P. N. First, and W. A. de Heer, "Electronic confinement and coherence in patterned epitaxial graphene," *Science*, vol. 312, no. 5777, pp. 1191–1196, 2006.

[98] F. Tuinstra and J. L. Koenig, "Raman spectrum of graphite," *J. Chem. Phys.*, vol. 53, no. 3, pp. 1126–1130, 1970.

[99] R. J. Nemanich and S. A. Solin, "First- and second-order Raman scattering from finite-size crystals of graphite," *Phys. Rev. B*, vol. 20, no. 2, pp. 392–401, 1979.

[100] D.-Q. Yang and E. Sacher, "Carbon $1s$ x-ray photoemission line shape analysis of highly oriented pyrolytic graphite: The influence of structural damage on peak asymmetry," *Langmuir*, vol. 22, no. 3, pp. 860–862, 2005.

[101] S. Kundu, Y. Wang, W. Xia, and M. Muhler, "Thermal stability and reducibility of oxygen-containing functional groups on multiwalled carbon nanotube surfaces: A quantitative high-resolution XPS and TPD/TPR study," *J. Phys. Chem. C*, vol. 112, no. 43, pp. 16 869–16 878, 2008.

[102] T. Okpalugo, P. Papakonstantinou, H. Murphy, J. McLaughlin, and N. Brown, "High resolution XPS characterization of chemical functionalised MWCNTs and SWCNTs," *Carbon*, vol. 43, no. 1, pp. 153–161, 2005.

[103] T. Ramanathan, F. T. Fisher, R. S. Ruoff, and L. C. Brinson, "Amino-functionalized carbon nanotubes for binding to polymers and biological systems," *Chem. Mater.*, vol. 17, no. 6, pp. 1290–1295, 2005.

[104] M. Gryziński, "Classical theory of atomic collisions. I. Theory of inelastic collisions," *Physical Review*, vol. 138, no. 2A, pp. A336–A358, 1965.

[105] D. C. Elias, R. R. Nair, R. M. G. Mohuiddin, S. V. Morozov, P. Blake, M. P. Halsall, A. C. Ferrari, D. W. Boukhvalov, M. I. Katsnelson, A. K. Geim, and K. S. Novoselov, "Control of graphene's properties by reversible hydrogenation: Evidence for graphane," *Science*, vol. 323, no. 5914, pp. 610–613, 2009.

[106] J. T. Robinson, J. S. Burgess, C. E. Junkermeier, S. C. Badescu, T. L. Reinecke, F. K. Perkins, M. K. Zalalutdniov, J. W. Baldwin, J. C. Culbertson, P. E. Sheehan, and E. S. Snow, "Properties of fluorinated graphene films," *Nano Lett.*, vol. 10, no. 8, pp. 3001—3005, 2010.

[107] M. Y. Han, B. Özyilmaz, Y. Zhang, and P. Kim, "Energy band-gap engineering of graphene nanoribbons," *Phys. Rev. Lett.*, vol. 98, no. 20, p. 206805, 2007.

[108] M. C. Lemme, D. C. Bell, J. R. Williams, L. A. Stern, B. W. H. Baugher, P. Jarillo-Herero, and C. M. Marcus, "Etching of graphene devices with a helium ion beam," *ACS Nano*, vol. 3, no. 9, pp. 2674–2676, 2009.

[109] L. Jiao, X. Wang, G. Diankov, H. Wang, and H. Dai, "Facile synthesis of high-quality graphene nanoribbons," *Nature Nanotech.*, vol. 5, pp. 321–325, 2010.

[110] M. Y. Han, J. C. Brant, and P. Kim, "Electron transport in disordered graphene nanoribbons," *Phys. Rev. Lett.*, vol. 104, no. 5, p. 056801, 2010.

[111] Y.-W. Son, M. L. Cohen, and S. G. Louie, "Energy gaps in graphene nanoribbons," *Phys. Rev. Lett.*, vol. 97, no. 21, p. 216803, 2006.

[112] L. Brey and H. A. Fertig, "Electronic states of graphene nanoribbons studied with the Dirac equation," *Phys. Rev. B*, vol. 73, no. 23, p. 235411, 2006.

[113] R. Saito, M. S. Dresselhaus, and G. Dresselhaus, *Physical Properties of Carbon Nanotubes.* London: Imperial College Press, 1998.

[114] Y. Yang and R. Murali, "Impact of size effect on graphene nanoribbon transport," *IEEE Electron Dev. Lett.*, vol. 31, no. 3, pp. 237–239, 2010.

[115] M. Sprinkle, M. Ruan, Y. Hu, J. Hankinson, M. Rubio-Roy, B. Zhang, X. Wu, C. Berger, and W. A. de Heer, "Scalable templated growth of graphene nanoribbons on SiC," *Nature Nanotech.*, vol. 5, pp. 727–731, 2010.

[116] M. Ruan, Y. Hu, Z. Guo, R. Dong, J. Palmer, J. Hankinson, C. Berger, and W. A. de Heer, "Epitaxial graphene on silicon carbide: Introduction to structured graphene," *MRS Bull.*, vol. 37, no. 12, pp. 1138–1147, 2012.

[117] H. Matsunami and T. Kimoto, "Step-controlled epitaxial growth of SiC: High quality homoepitaxy," *Mat. Sci. and Eng.*, vol. 20, no. 3, pp. 125–166, 1997.

[118] V. Borovikov and A. Zangwill, "Step bunching of vicinal 6H-SiC{0001} surfaces," *Phys. Rev. B*, vol. 79, no. 24, p. 245413, 2009.

[119] S. Nakamura, T. Kimoto, H. Matsunami, S. Tanaka, N. Teraguchi, and A. Suziki, "Formation of periodic steps with a unit-cell height on 6H-SiC (0001) surface by HCl etching," *Appl. Phys. Lett.*, vol. 76, no. 23, pp. 3412–3414, 2000.

[120] V. Ramachandran, M. F. Brady, A. R. Smith, R. M. Feenstra, and D. W. Greve, "Preparation of atomically flat surfaces on silicon carbide using hydrogen etching," *J. Electron. Mat.*, vol. 27, no. 4, pp. 308–312, 1998.

[121] H. S. Kong, J. T. Glass, and R. F. Davis, "Chemical vapor deposition and characterization of 6H-SiC thin films on off-axis 6H-SiC substrates," *J. Appl. Phys.*, vol. 64, no. 5, pp. 2672–2679, 1988.

[122] T. Kimoto, A. Itoh, and H. H. Matsunami, "Step bunching in chemical vapor deposition of 6H- and 4H-SiC and vicinal SiC (0001) faces," *Appl. Phys. Lett.*, vol. 66, no. 26, pp. 3645–3647, 1995.

[123] M. Syväjärvi, R. Yakimova, E., and Janzén, "Step-bunching in SiC epitaxy: anisotropy and influence of growth temperature," *J. of Cryst. Growth*, vol. 236, no. 1–3, pp. 297–304, 2002.

[124] S. Ryu, M. Y. Han, J. Maultzsch, T. F. Heinz, P. Kim, M. L. Steigerwald, and L. E. Brus, "Reversible basal plane hydrogenation of graphene," *Nano Lett.*, vol. 8, no. 12, pp. 4597–4602, 2008.

[125] T. Burnett, R. Yakimova, and O. Kazakova, "Mapping of local electrical properties in epitaxial graphene using electrostatic force microscopy," *Nano Lett.*, vol. 11, no. 6, pp. 2324–2328, 2011.

[126] A. Das, S. Pisana, B. Chakraborty, S. Piscanec, S. K. Saha, U. V. Waghmare, K. S. Novoselov, H. R. Krishnamurthy, A. K. Geim, A. C. Ferrari, and A. K. Sood, "Montoring dopants by Raman scattering in an electrochemically top-gated graphene transistor," *Nature Nanotech.*, vol. 3, pp. 210–215, 2008.

[127] D. S. Lee, C. Riedl, B. Krauss, K. von Klitzing, U. Starke, and J. H. Smet, "Raman spectra of epitaxial graphene on SiC and of epitaxial graphene transferred to SiO$_2$," *Nano Lett.*, vol. 8, no. !2, pp. 4320–4325, 2008.

[128] A. G. Souza Filho, A. Jorio, G. G. Samsonidze, G. Dresselhaus, M. A. Pimenta, M. S. Dresselhaus, A. K. Swan, M. S. Ünlü, B. B. Goldberg, and R. Saito, "Competing spring constant versus double resonance effects on the properties of dispersive modes in isolated single-wall carbon nanotubes," *Phys. Rev. B*, vol. 67, no. 3, p. 035427, 2003.

[129] Z. H. Ni, H. M. Wang, Y. Ma, J. Kasim, Y. H. Wu, and Z. X. Shen, "Tunable stress and controlled thickness modification in graphene by annealing," *ACS Nano*, vol. 2, no. 5, pp. 1033–1039, 2008.

[130] J. Röhrl, M. Hundhausen, K. V. Emtsev, Th. Seyller, R. Graupner, and L. Ley, "Raman spectra of epitaxial graphene on SiC(0001)," *Appl. Phys. Lett.*, vol. 92, no. 20, p. 201918, 2008.

[131] F. Amy, P. Soukiassian, Y. K. Hwu, and C. Brylinski, "Si-rich 6H- and 4H-SiC (0001) 3×3 surface oxidation and initial SiO_2/SiC interface formation from 25 to 650 °C," *Phys. Rev. B*, vol. 65, no. 16, p. 165323, 2002.

[132] S. Y. Zhou, G.-H. Gweon, A. V. Fedorov, P. N. First, W. A. de Heer, L. F. Guinea, A. H. Castro Neto, and A. Lanzara, "Substrate-induced bandgap opening in epitaxial graphene," *Nature Mater.*, vol. 6, pp. 770–775, 2007.

[133] W. Norimatsu and M. Kusunoki, "Formation process of graphene on SiC (0001)," *Physica E*, vol. 42, no. 4, pp. 691–694, 2010.

[134] L. Liao, Y. Lin, M. Bao, R. Cheng, J. Bai, Y. Liu, Y. Qu, K. L. Wang, Y. Huang, and X. Duan, "High-speed graphene transistors with a self-aligned nanowire gate," *Nature*, vol. 467, pp. 305–308, 2010.

[135] Y. Wu, K. A. Jenkins, A. Valdes-Garcia, D. B. Farmer, Y. Zhu, A. A. Bol, C. Dimitrakopoulos, W. Zhu, F. Xia, P. Avouris, and Y.-M. Lin, "State-of-the-art graphene high-frequency electronics," *Nano Lett.*, vol. 12, no. 6, pp. 3062–3067, 2012.

[136] S.-L. Li, H. Miyazaki, A. Kumatani, A. Kanda, and K. Tsukagoshi, "Low operating bias and matched input-output characteristics in graphene logic inverters," *Nano Lett.*, vol. 10, no. 7, pp. 2357–2362, 2010.

[137] L. G. Rizzi, M. Bianchi, A. Behnam, E. Carrion, E. Guerriero, L. Polloni, E. Pop, and R. Sordan, "Cascading wafer-scale integrated graphene complementary inverters under ambient conditions," *Nano Lett.*, vol. 12, no. 8, pp. 3948–3953, 2012.

[138] D. W. Brenner, O. A. Shenderova, J. A. Harrison, S. J. Stuart, B. Ni, and S. B. Sinnott, "A second-generation reactive empirical bond order (REBO) potential

energy expression for hydrocarbons," *J. Phys.: Condens. Matter*, vol. 14, no. 4, pp. 783–802, 2002.

[139] C. L. Kane and E. J. Mele, "Size, shape, and low energy electronic structure of carbon nanotubes," *Phys. Rev. Lett.*, vol. 78, no. 10, pp. 1932–1935, 1997.

[140] E.-A. Kim and A. H. Castro Neto, "Graphene as an electronic membrane," *Europhys. Lett.*, vol. 84, no. 5, p. 57007, 2008.

[141] V. M. Pereira and A. H. Castro Neto, "Tight-binding approach to uniaxial strain in graphene," *Phys. Rev. B*, vol. 80, no. 4, p. 045401, 2009.

[142] M. K. Yakes, D. Dunlycke, J. L. Tedesco, P. M. Campbell, R. L. Myers-Ward, C. R. Eddy, D. K. Gaskill, P. E. Sheehan, and A. R. Laracuente, "Conductance anisotropy in epitaxial graphene sheets generated by substrate interactions," *Nano Lett.*, vol. 10, no. 5, pp. 1559–1562, 2010.

[143] S.-H. Ji, J. B. Hannon, R. M. Tromp, V. Perebeinos, J. Tersoff, and F. M. Ross, "Atomic-scale transport in epitaxial graphene," *Nature Mater.*, vol. 11, pp. 114–119, 2012.

[144] T. Low, V. Perebeinos, J. Tersoff, and P. Avouris, "Deformation and scattering in graphene over substrate steps," *Phys. Rev. Lett.*, vol. 108, no. 9, p. 096601, 2012.

[145] C. E. Malec and D. Davidović, "Transport in graphene tunnel junctions," *J. Appl. Phys.*, vol. 109, no. 6, p. 064507, 2011.

[146] B. Dlubak, M.-B. Martin, C. Deranlot, B. Servet, S. Xavier, R. Mattana, M. Sprinkle, C. Berger, W. A. de Heer, F. Petroff, A. Anane, P. Seneor, and A. Fert, "Highly efficient spin transport in epitaxial graphene on SiC," *Nature Phys.*, vol. 8, pp. 557–561, 2012.

[147] X. Wang, S. M. Tabakman, and H. Dai, "Atomic layer deposition of metal oxides on pristine and functionalized graphene," *J. Am. Chem. Soc.*, vol. 130, no. 26, pp. 8152–8153, 2008.

[148] B. Lee, S.-Y. Park, H.-C. Kim, K.-J. Cho, E. M. Vogel, M. J. Kim, R. M. Wallace, and J. Kim, "Conformal Al_2O_3 dielectric layer deposited by atomic layer deposition for graphene-based nanoelectronics," *Appl. Phys. Lett.*, vol. 92, no. 20, p. 203102, 2008.

[149] D. B. Farmer, H.-Y. Chiu, Y.-M. Lin, K. A. Jenkins, F. Xia, and P. Avouris, "Utilization of a buffered dielectric to achieve high field-effect carrier mobility in graphene transistors," *Nano Lett.*, vol. 9, no. 12, pp. 4474–4478, 2009.

[150] F. Xia, V. Perebeinos, Y.-M. Lin, Y. Wu, and P. Avouris, "The origins and limits of metal-graphene junction resistance," *Nature Nanotech.*, vol. 6, pp. 179–184, 2011.

[151] B. J. Kim, H. Jang, S.-K. Lee, B. H. Hong, J.-H. Ahn, and J. H. Cho, "High-performance flexible graphene field effect transistors with ion gel gate dielectrics," *Nano Lett.*, vol. 10, no. 9, pp. 3464–3466, 2010.

[152] I. Meric, C. Dean, A. Young, J. Hone, P. Kim, and K. L. Shepard, "Graphene field-effect transistors based on boron nitride gate dielectrics," *Proc. IEEE Int. El. Devices Meet.*, pp. 23.2.1–23.2.4, 2010.

[153] N. Klein and E. Burstein, "Electrical pulse breakdown of silicon oxide films," *J. Appl. Phys.*, vol. 40, no. 7, pp. 2728–2740, 1969.

[154] J. Kolodzey, E. A. Chowdhury, T. N. Adam, G. Qui, I. Rau, J. O. Olowolafe, J. S. Suehle, and Y. Chen, "Electrical conduction and dielectric breakdown in aluminum oxide insulators on silicon," *IEEE Trans. Electron Dev.*, vol. 47, no. 1, pp. 121–128, 2000.

[155] H. H. Berger, "Models for contacts to planar devices," *Solid-State Electron.*, vol. 15, no. 2, pp. 145–158, 1972.

[156] W. Li, Y. Liang, D. Yu, L. Peng, K. P. Pernstich, T. Shen, A. R. Hight Walker, G. Cheng, C. A. Hacker, C. A. Richter, Q. Li, D. J. Gundlach, and X. Liang, "Ultraviolet/ozone treatment to reduce metal-graphene contact resistance," *Appl. Phys. Lett.*, vol. 102, no. 18, p. 183110, 2013.

[157] S. Ciraci, S. Dag, T. Yildirim, O. Gülseren, and R. T. Senger, "Functionalized carbon nanotubes and device applications," *J. Phys.: Condens. Matter*, vol. 16, no. 29, pp. R901–R960, 2004.

[158] M. Stockmeier, R. Müller, S. A. Sakwe, P. J. Wellmann, and A. Magerl, "On the lattice parameters of silicon carbide," *Appl. Phys. Lett.*, vol. 105, no. 3, p. 033511, 2009.

[159] R. O. Duda and P. E. Hart, "Use of the Hough transformation to detect lines and curves in pictures," *Commun. ACM*, vol. 15, no. 1, pp. 11–15, 1972.